

# Radiation tolerant CMOS photodetectors for low total ionizing dose applications

---

Šegmanović, Filip

Doctoral thesis / Disertacija

2024

*Degree Grantor / Ustanova koja je dodijelila akademski / stručni stupanj:* **University of Zagreb, Faculty of Electrical Engineering and Computing / Sveučilište u Zagrebu, Fakultet elektrotehnike i računarstva**

*Permanent link / Trajna poveznica:* <https://urn.nsk.hr/urn:nbn:hr:168:342443>

*Rights / Prava:* [In copyright](#)/[Zaštićeno autorskim pravom.](#)

*Download date / Datum preuzimanja:* **2025-03-14**



*Repository / Repozitorij:*

[FER Repository - University of Zagreb Faculty of Electrical Engineering and Computing repozitory](#)





University of Zagreb  
FACULTY OF ELECTRICAL ENGINEERING AND COMPUTING

Filip Šegmanović

**RADIATION TOLERANT CMOS  
PHOTODETECTORS FOR LOW TOTAL IONIZING  
DOSE APPLICATIONS**

DOCTORAL THESIS

Zagreb, 2024.



University of Zagreb  
FACULTY OF ELECTRICAL ENGINEERING AND COMPUTING

Filip Šegmanović

**RADIATION TOLERANT CMOS  
PHOTODETECTORS FOR LOW TOTAL IONIZING  
DOSE APPLICATIONS**

DOCTORAL THESIS

Supervisor: Professor Tomislav Suligoj, PhD

Zagreb, 2024.



Sveučilište u Zagrebu  
FAKULTET ELEKTROTEHNIKE I RAČUNARSTVA

Filip Šegmanović

**CMOS FOTODETEKTORI OTPORNI NA  
ZRAČENJE ZA PRIMJENU U OKOLINI NISKE  
TOTALNE IONIZACIJSKE DOZE**

DOKTORSKI RAD

Mentor: Prof. dr. sc. Tomislav Suligoj

Zagreb, 2024.





The doctoral thesis was done at the University of Zagreb, Faculty of Electrical Engineering and Computing, at the Department of electronics, microelectronics, computer and intelligent systems.

Supervisor: Professor Tomislav Suligoj, PhD

The doctoral thesis contains: 120 pages

Doctoral thesis no.: \_\_\_\_\_

## About the Supervisor

Tomislav Suligoj received Diploma engineer, M.Sc. and Ph.D. degrees in electrical engineering from the University of Zagreb, Faculty of Electrical Engineering and Computing (FER), Croatia, in 1995, 1998 and 2001, respectively. Currently, he is a full professor at FER, Department of Electronics, Microelectronics, Computing and Intelligent Systems, teaching the courses in the area of electronics and microelectronics. He was a visiting researcher at the University of California, Los Angeles (1999-2001) and a postdoctoral researcher at the Hong Kong University of Science and Technology (2001-2002). He has been a Principal Investigator of more than 30 projects so far supported by the government agencies, international companies and universities. He published more than 20 patents and 200 papers in journals and conference proceedings in the area of design, measurements and modelling of electron devices, micro and nano electronics, semiconductor technology and integrated circuit design. He is a head of Micro and nano Electronics laboratory (MiNEL) at FER, where numerous novel and record-breaking electron devices and integrated circuits have been invented and demonstrated. Prof. Suligoj received 15 scientific awards including National Science Award; Golden plaque at innovation exhibition ARCA; Best paper awards at MIPRO MEET conference, Faculty medals “Josip Lončar” for outstanding Doctoral Dissertation, and Fulbright scholarship. He was a Symposium Chair, Technical Program Chair and a Chairman of Device Physics Subcommittee at IEEE BiCMOS and Compound Semiconductor Integrated Circuits and Technology Symposium (BCICTS). He is a Steering Committee member of MIPRO MEET conference, Technical Program Committee member of European Solid-State Electronics Research Conference (ESSERC) and MIEL. He was a President of Electron Devices / Solid-State Circuits Joint Chapter, IEEE Croatia Section. He gave numerous invited talks at the conferences, universities, institutions and companies.

## O mentoru

Tomislav Suligoj je diplomirao, magistrirao i doktorirao u polju elektrotehnike na Sveučilištu u Zagrebu, Fakultetu elektrotehnike i računarstva (FER), 1995., 1998. odnosno 2001. godine. Trenutno je redoviti profesor na Zavodu za elektroniku, mikroelektroniku, računalne i inteligentne sustave FER-a gdje predaje kolegije u području elektronike i mikroelektronike. Bio je gostujući istraživač na University of California, Los Angeles od 1999. do 2001. godine te na poslijedoktorskom usavršavanju na Hong Kong University of Science and Technology od 2001. do 2002. Dosada je vodio više od 30 projekata financiranih državnih institucija, međunarodnih kompanija i sveučilišta. Objavio je više od 20 patenata i 200 radova u časopisima i zbornicima konferencija u području projektiranja, mjerenja i modeliranja elektroničkih elemenata, mikro i nano elektronike, poluvodičke tehnologije i projektiranja integriranih sklopova. Voditelj je Laboratorija za mikro i nano elektroniku (MiNEL) FER-a u okviru kojeg je izumljen i demonstriran velik broj novih elektroničkih elemenata i integriranih sklopova od kojih mnogi imaju rekordne karakteristike. Prof. Suligoj je dobitnik 15 nagrada uključujući Državnu nagradu za znanost, Zlatnu plaketu na izložbi inovacija ARCA, Best paper awards na MIPRO MEET konferenciji, srebrnu plaketu "Josip Lončar" za posebno istaknutu doktorsku disertaciju te Fulbright-ovu stipendije. Bio je Symposium Chair, Technical Program Chair and a Chairman of Device Physics Subcommittee konferencije IEEE BiCMOS and Compound Semiconductor Integrated Circuits and Technology Symposium (BCICTS). Član je Steering Committee konferencije MIPRO MEET, tehničkog odbora konferencija European Solid-State Electronics Research Conference (ESSERC) i MIEL. Bio je predsjednik Odjela za elektroničke elemente i poluvodičke integrirane sklopove Hrvatske sekcije IEEE. Održao je velik broj pozvanih predavanja na međunarodnim konferencijama, sveučilištima, institutima i kompanijama.

## **Acknowledgment**

I would like to thank my supervisors at ams OSRAM, Ingrid Jonak-Auer and Frederic Roger, for their help and guidance during my PhD studies. The technical experience and insights within the CMOS industry you provided is something I will never forget. I would like to thank my supervisor at the University of Zagreb, Prof. Tomislav Suligoj, for his commitment and patience during the PhD and for supporting me in pursuing the ideas and topics I was interested in. Special thanks to Peter Leinfellner, Karl Rohrer and other colleagues from ams OSRAM for their support in various engineering topics. Finally, thanks to my family, who were always there for me and who supported me in every step I took. Last but not least, huge thanks to my girlfriend, Ivana, who plays a key role in everything I do and whose cooking skills were a critical asset in enduring the PhD.

This research project has been supported by a Marie Skłodowska-Curie Innovative Training Network Fellowship of the European Commission's Horizon 2020 Programme under contract number 675587 STREAM.

## Abstract

This work will present design and optimization of radiation-hard optical sensors, for medical applications, specifically CT scanner. Sensor structures are processed in a standard *ams OSRAM* 180 nm high-voltage CMOS technology. Main characteristics of these structures is the special epitaxial layer, which has a feature of high-lifetime of minority carriers, thus enabling efficient charge collection by diffusion mechanism. This also removes the need of a fully depleted epitaxial layer. The structure consists of multiple collection electrodes, which additionally lowers the dark current and the capacitance. The designed test-chip consists of different photodiode structures with process and layout variations. The electrical and optical performance of the test-chip will be tested under ionizing radiation, with the main goal of improving radiation-hardness. Four test-structures, comparable in size and layout with the prototype structure in 350 nm process node, are analyzed in more detail and a comparison with the 350 nm process node is given. Finally, TCAD simulations are carried out, which model the dark current and spectral responsivity degradation due to ionizing radiation induced defects.

**Keywords:** Ionizing radiation, Dark current, Medical applications, Semiconductor detectors, Radiation hardness (electronics), TCAD simulations, Total ionizing dose

## **CMOS fotodetektor otporni na zračenje za primjenu u okolini niske totalne ionizacijske doze**

Poluvodički optički senzori se primjenjuju u mnogim aplikacijama, poput sigurnosnih i automobilskih, pa sve do medicinskih, znanstvenih i svemirskih aplikacija gdje se zahtjeva visoka otpornost detektora na zračenje. Konkretno, u medicinskim aplikacijama poput CT skenera, za dobivanje slike se koriste X-zrake, koje za razliku od vidljive svjetlosti, generiraju parove elektron-šupljina po cijeloj putanji čestice. U većini slučajeva je senzor izveden kao zaporno-polarizirani p-n spoj sa ciljem da je osiromašeno područje čim veće, jer se time naboj brzo i efikasno skuplja putem električnog polja, odnosno mehanizmom drifta. Također postoje i izvedbe senzora koje ne koriste potpuno osiromašenje, te se u tom slučaju sakupljanje naboja obavlja putem difuzije. U tom je slučaju potrebno koristiti posebni materijal podloge sa svojstvom velikog vremena života manjskih nosilaca, čime se osigurava dovoljno dugačka difuzijska duljina kako bi se naboj efikasno skupio. Sakupljeni naboj se dalje obrađuje korištenjem analognih sklopova, te se u zadnjem koraku obavlja analogno-digitalna konverzija nakon čega se dobiva konačna slika. U CT-skeneru postoje dva principa konverzije X-zraka u električni signal: direktna i indirektna konverzija. Kod direktne konverzije, X-zrake direktno upadaju na detektor, te se generirani naboj unutar strukture skuplja putem sakupljačke elektrode i onda se dovodi na daljnju obradu signala. S druge strane, kod indirektna konverzije se koristi scintilator, koji služi kao membrana kojom se visoko-energetski fotoni X-zraka pretvaraju u nisko-energetske fotone vidljive svjetlosti, te se oni dalje detektiraju na fotodiodi i sakupljaju te šalju na daljnju obradu signala. Što je veća efikasnost pretvorbe X-zraka u vidljivu svjetlost, time je i sama efikasnost detektora veća, a ujedno je potrebna i manja doza zračenja kako bi se postigla jednaka kvaliteta slike.

Zračenjem uzrokovana oštećenja na sensorima degradiraju performanse te limitiraju stabilnost i pouzdanost senzora. Električka i optička svojstva senzora degradiraju tim oštećenjima, te se to vidi pri porastu tamne struje i smanjenju spektralnog odziva nakon ozračivanja. Efekti zračenja se dijele na kumulativne i pojedinačne tranzijentne efekte. Kumulativni efekti su gradijentni efekti, koji su prisutni tokom cijelog radnog vijeka senzora i dijele se na ionizacijske i neionizacijske efekte. Na primjer, senzor osjetljiv na totalnu-ionizacijsku dozu (TID) će pokazati degradaciju nakon što se premaši limit akumulirane TID-e. S druge strane, pojedinačni efekti nastaju zbog prijenosa energije pojedinačne čestice na osjetljive elektroničke sklopove. U slučaju CT-skenera i detektora X-zraka, samo se kumulativni efekti promatraju, specifično ionizacijski efekti.

Ionizacijsko zračenje je posljedica interakcije nabijenih čestica i visoko-energetskih fotona sa senzorskom strukturom, uslijed čega dolazi do generacije naboja u silicijskoj strukturi, ali i u izolacijskim slojevima. Na primjer, u silicijevom dioksidu, dolazi do akumulacije naboja, te uslijed toga i do stvaranja nezasićenih kovalentnih veza na granici između dielektrika i silicija. Kada ionizacijska čestica generira naboj u oksidu, dio elektrona i šupljina se odmah rekombinira. Preostali dio naboja se razdvoji uslijed ugrađenog električnog polja, i elektroni krenu prema upravljačkoj elektrodi (unutar nekoliko pikosekundi), dok se šupljine kreću prema granici silicija i oksida. Udio nerekombiniranog naboja ovisi prije svega o veličini čestice, odnosno gustoći generiranog naboja. Veće čestice, poput protona, će generirati veće skupine manje razmaknutih naboja, a time je vjerojatnost rekombinacije veća te će manje naboja izbjeći početnu rekombinaciju. S druge strane, manje čestice poput elektrona i fotona će generirati naboje u većim razmacima, i time će više naboja izbjeći inicijalnu rekombinaciju te će se više naboja akumulirati na granici između silicija i oksida. Šupljine se unutar oksida kreću preko lokaliziranih stanja, te s obzirom da je pokretljivost šupljina u oksidu puno manja ( $10^5$  puta manja) nego pokretljivost elektrona, proces akumulacije šupljina može biti dugotrajan ( $\sim 1000$  s). Nakon što se šupljine akumuliraju na granici između silicija i oksida, može doći do interakcije između šupljina i pasiviziranih vodikovih atoma. Interakcijom nastaju protoni, koji se onda kreću duž međupovršine te reagiraju s drugim protonima, čime se stvaraju površinska stanja. Ti defekti degradiraju performanse senzora, prije svega električne i optičke parametre poput povećanja struje curenja i smanjenja spektralnog odziva. Glavni parametri akumuliranog pozitivnog naboja u oksidu, te zamki u siliciju su gustoća akumuliranog naboja, gustoća zamki, udarni presjek za elektrone i šupljine, te energetski nivo u zabranjenom pojasu i vrsta zamke (akceptorska ili donorska zamka).

Postoji više metoda kako se senzor može učiniti otpornim na zračenje. Temperaturnim procesima između  $125\text{ }^{\circ}\text{C}$  i  $170\text{ }^{\circ}\text{C}$  je moguće dobrim dijelom popraviti oštećenja u oksidu, dok se samo 30 % nezasićenih veza popravi. Češće se koriste procesne metode, poput visokodopiranih plitkih slojeva koji služe kao energetska barijera za sprječavanje akumulacije manjinskih nosilaca na strani silicija. Također se često koristi potpuno osiromašeni epitaksijalni sloj, čime se efikasnost skupljanja naboja poboljšava, jer se smanjuje vjerojatnost zarobljavanja naboja. U slučaju projektiranih struktura u ovom radu, koristi se poseban epitaksijalni materijal sa svojstvom velikog vremena života manjinskih nosilaca, čime se omogućava sakupljanje naboja i putem difuzije. Uz to, osiromašeno područje je vrlo maleno, čime se također smanjuje i tamna struja, a zbog manje površine p-n spoja kapacitet se također smanjio, dok je spektralni odziv ostao isti.



U ovoj disertaciji se analizira otpornost na zračenje dizajniranih fotodetektora u *ams OSRAM* 180 nm CMOS tehnologiji. Referentne strukture su procesirane u 350 nm *ams OSRAM* tehnologiji. Četiri strukture su dizajnirane, te se one razlikuju u zastupljenosti plitkog izolacijskog sloja oksida (engl. shallow trench isolation, STI) po fotoaktivnoj površini. STI linije su implemetirane kako bi se omogućilo pravilno procesiranje time što se velika fotoaktivna površina segmentirala na manje dijelove. Fotoaktivno područje je podijeljeno na 242 otoka n-tipa te je površina između otoka pasivizirana visoko-dopirajućim plitkim slojem p-tipa. Na rubu fotoaktivnog područja se nalazi zaštitni prsten kako bi se smanjilo preslušavanje između susjednih pixela.

Silicijski wafer se podijelio na četiri kvadranta, te je na svakom kvadrantu definiran referentni čip ovisno o tome kojom je ionizacijskom dozom ozračen. Gornji desni kvadrant je referentni kvadrant jer taj kvadrant nije ozračen i on služi za normalizaciju optičkih mjerenja. U tri od četiri kvadranta (svi osim donjeg desnog kvadranta) je implementiran plitki p-tip sloj (engl. shallow p-type implant, SPI) ispod STI, kako bi se i ta površina djelomično pasivizirala.

Ozračivanje se provodi na razini wafera, odnosno svaki od tri referentna čipova na waferu (gornji lijevi te donji lijevi i donji desni kvadranti) su ozračeni redom sa TID = 100 Gy(Si), 200 Gy(Si) i 400 Gy(Si), konstantnom stopom od 100 Gy/h. Prije ozračivanja, laserom se uskladila zraka ozračivanja sa referentnim čipovima na waferu. Nakon ozračivanja, wafer je pospremljen u kutiju za skladištenje wafera te je ona stavljena u vakumiranu izolacijsku vreću, koja je stavljena u hladnjak kako bi se spriječilo napuštanje generiranih defekata uslijed ionizacijskog zračenja.

Nakon ozračivanja, wafer je pažljivo transportiran do optičkog laboratorija gdje se provode optička i električka mjerenja, poput strujno-naponske i kapacitivno-naponske karakteristike, te spektralnog odziva. Mjerenja su izvršena prije i poslije ozračivanja, s ciljem usporedbe prethodno navedenih karakteristika, te definiranja otpornosti na zračenje promatranih fotodioda. Zaključeno je da na životnoj dozi CT skenera, TID = 200 Gy(Si), nije došlo do degradacije promatranih karakteristika, te su fotodiode potpuno otporne na ionizacijsko zračenje do TID = 200 Gy(Si). Nakon TID = 400 Gy(Si), tamna struja je degradirala 15 %, spektralni odziv 2.3 %, dok se kapacitet nije promijenio.

Uz analizu mjerenja je provedena i usporedba između sličnih fotodioda procesiranih u 180 nm i 350 nm *ams OSRAM* CMOS tehnologijama. Usporedbom karakteristika prije ozračivanja, zaključeno je da fotodiode procesirane u 350 nm tehnologiji imaju nižu tamnu struju i kapacitet, zbog razlika u procesnim parametrima poput energije implantacije, termalnog budžeta i strmine profila primjesa, te STI linija koje su implementirane u 180 nm

tehnologiji. Fotodetektor procesirani u 180 nm tehnologiji imaju veći spektralni odziv, po promatralnom spektru valne duljine (400 nm – 900 nm), u odnosu na fotodiode u 350 nm tehnologiji. Uz razlike u procesnim parametrima, u 180 nm tehnologiji je dodatno korišten tanki sloj silicijeva nitrida, koji služi kao antirefletkivni sloj, čime se poboljšava spektralni odziv.

Nakon ozračivanja, tamna struja fotodioda u 350 nm tehnologiji je degradirala 89 % nakon  $TID = 200 \text{ Gy(Si)}$ , dok u slučaju fotodioda u 180 nm tehnologiji nije bilo degradacije. Nadalje, nakon  $TID = 400 \text{ Gy(Si)}$ , degradacija tamne struje fotodioda u 180 nm tehnologiji je bila manja, nego degradacija fotodioda u 350 nm tehnologiji nakon  $TID = 200 \text{ Gy(Si)}$ . Kapacitet fotodioda u 350 nm tehnologiji je i poslije ozračivanja niži u odnosu na fotodiode u 180 nm tehnologiji, no također je kapacitet degradirao 3-4 %, dok kapacitet fotodioda u 180 nm tehnologiji nije uopće degradirao nakon ozračivanja. U slučaju spektralnog odziva, obje tehnologije su otporne na ionizacijsko zračenje do  $TID = 200 \text{ Gy(Si)}$ , jer je degradacija spektralnog odziva manja od 1 %. Uspoređujući omjer normalizirane fotostruje sa tamnom strujom, može se zaključiti da su fotodiode u 180 nm tehnologiji degradirale 15 %, dok su slične strukture u 350 nm tehnologiji degradirale 50 %. Uzevši u obzir cijelu usporedbu, može se zaključiti da su fotodiode procesirane u 180 nm tehnologiji otporne na zračenje do  $TID = 200 \text{ Gy(Si)}$ , dok na istoj  $TID$  fotodiode u 350 nm tehnologiji vide veliki porast tamne struje i malu degradaciju kapaciteta.

Uz pomoć TCAD software-a su izvršene električke i optičke simulacije fotodioda u 180 nm i 350 nm tehnologijama. U slučaju zaporno-polarizirane strujno-naponske karakteristike, kapacitivno-naponske karakteristike i spektralnog odziva, jedno-otočni poprečni presjek je simuliran. Implementiran je statistički dizajn eksperimenta (DoE) koji je obuhvatio razne fizikalne parametre, poput zabranjenog pojasa, pokretljivost manjniskih nosioca, Shockley-Read-Hall rekombinacije te Auger rekombinacije, kako bi se provela kalibracija simulacija s mjerenjima. Metodologija DoE je uzela u obzir varijaciju ulaznih parametara unutar fizikalnih granica te su se promatrane karakteristike, poput tamne struje i spektralnog odziva, modelirale kao kvadratna jednažba ulaznih parametara. Konačna normalizacija je provedena tako što se simulirana karakteristika skalirala na 242 otoka, što je ukupni broj otoka u procesiranim strukturama. S druge strane, propusno-polarizirana strujno-naponska karakteristika je simulirana tako što se uzeo u obzir i periferni dio strukture, odnosno područje između otoka. Zbog toga je prilagođen poprečni presjek strukture, te se on sastojao od više susjednih otoka, koji su okruženi zaštitnim prstenom.

Sličnim statističkim dizajnom su modelirane strujno-naponske karakteristike fotodioda u 180 nm tehnologiji, nakon ozračivanja. U tom slučaju su ulazni parametri bili parametri zračenjem generiranih defekata, poput gustoće nezasićenih silicijskih veza (zamki) na granici

sa oksidom, energetski nivoi akceptorskih i donorskih zamki, udarni presjeci elektrona i šupljina, te gustoće fiksnog naboja u oksidu i nitridu. Model je objašnjen na primjeru zabranjenog pojasa u području fotodiode gdje osiromašeno područje dolazi do granice između silicija i oksida. Zaključeno je da je došlo do proširenja osiromašenog područja uz površinu, jer je u n-otoku dio akceptorskih zamki ispod kvazi-Fermijevog nivoa. Te zamke manje sudjeluju u generacijsko-rekombinacijskim procesima, a više djeluju kao dodatan fiksni naboj, što rezultira proširenjem osiromašenog područja. Usporedbom kalibriranih simulacija i mjerenja nakon ozračivanja, može se zaključiti da je u slučaju tamne struje kalibracija bila uspješna u širem naponskom rasponu, od 0.75 V do 1.75 V, te je obuhvatilo naponsku radnu točku koja je određena izlaznim pojačalima i iznosi 1.25 V. U slučaju kapaciteta, razlika između simulacija i mjerenja je vidljiva zbog toga što u simulacijama nisu obuhvaćene parazitne komponente kapaciteta, koje dolaze od metalizacijskih slojeva i izolacijskih oksida. S druge strane, simulacije također nisu pokazale porast kapaciteta nakon ozračivanja, te je time potvrđena otpornost na zračenje fotodiode u 180 nm tehnologiji. Zbog kompleksne strukture fotodiode u 180 nm tehnologiji, optičke simulacije nisu provedene, ali je prikazana usporedba poprečnog presjeka sa i bez SPI na granici između STI i silicija. Zaključeno je da SPI pomaže u poboljšanju otpornosti na zračenje, no s obzirom da je doza zračenja bila niska, njegov utjecaj nije bio značajan.

**Ključne riječi:** Ionizacijsko zračenje, Tamna struja, Medicinske aplikacije, Poluvodički detektori, Otpornost na zračenje (elektroničko), TCAD simulacije, Totalna ionizacijska doza

# Contents

1. Introduction .....	1
1.1. CT scanner detectors .....	5
1.2. Radiation-hard photodiode concepts .....	8
2. Radiation damage in silicon structures .....	13
2.1. Total ionizing dose induced defects .....	13
2.1.1. Hole charge yield .....	15
2.1.2. Fixed charges in the insulating layers .....	17
2.1.3. Interface traps at the silicon/insulator interface .....	18
2.2. Summary .....	19
3. Design of radiation-hard photodiodes in <i>ams OSRAM</i> 180nm CMOS technology .....	20
3.1. Starting material .....	20
3.2. Photodiode test-chip .....	21
3.3. Summary .....	25
4. X-ray experiments .....	27
4.1. Wafer-level X-ray irradiation .....	27
4.2. Wafer packaging .....	33
4.3. Summary .....	35
5. Wafer-level measurements .....	36
5.1. Pre-irradiation characterization .....	36
5.1.1. Current-voltage characteristics .....	36
5.1.2. Capacitance-voltage characteristics .....	38
5.1.3. Spectral responsivity characteristics .....	39
5.2. Post-irradiation characterization .....	42
5.2.1. Current-voltage characteristics .....	43
5.2.2. Capacitance-voltage characteristics .....	45
5.2.3. Spectral responsivity characteristics .....	46
5.3. Summary .....	55
6. Technology comparison (180 nm vs 350 nm) .....	57
6.1. Current-voltage characteristics comparison .....	57
6.2. Capacitance-voltage characteristics comparison .....	58
6.3. Spectral responsivity characteristics comparison .....	59
6.4. Summary .....	64
7. Electrical and optical characteristics analysis and simulations .....	66

7.1. Simulated photodiode structure in <i>ams OSRAM</i> 350 nm CMOS technology.....	67
7.2. TCAD parameter variability for calibration of pre-irradiation simulations .....	70
7.3. Statistical design of experiment .....	73
7.4. Photodiode structure simulation in <i>ams OSRAM</i> 180 nm CMOS technology and pre-irradiation electrical characteristics measurement fitting.....	80
7.5. Implementation of TID induced defects in TCAD environment .....	83
7.6. Impact of the SPI on the STI/Si interface .....	86
7.7. Modeling and calibration of trap parameters in TCAD simulations.....	91
7.8. TID model in 180 nm technology .....	93
7.8.1. Dark current comparison between the TCAD simulations and the measurements	97
7.8.2. Capacitance comparison between the TCAD simulations and the measurements.	99
7.9. Summary .....	100
8. Conclusion.....	102
9. Bibliography.....	107
Biography .....	118
Životopis.....	119
List of publications.....	119

# 1. Introduction

Imaging applications find their usage in many different applications, ranging from automotive and security applications to applications that operate in radiation environment like medical and space applications. For example, medical instruments like Computed Tomography (CT) scanners use X-rays in order to create images, thus the detectors have to be radiation-hard against ionizing radiation. An image sensor consists of a sensing device (a photodiode), which detects incoming light and converts the signal, via the readout circuit, into an electrical signal for further processing. Early solid-state image sensors were bipolar and MOS photodiode arrays developed in the late 1960s [1]. Charge-coupled devices (CCD) were invented in 1969 and became the dominant digital imaging technology in 1980s and 1990s [2]. CCD sensors are silicon-based integrated circuits that operate by converting light energy, in the form of photons, into electric charges. When a photon of specific wavelength strikes a silicon crystal lattice (Si) in or near a CCD photo-site, it creates a free electron and a hole via the photoelectric effect. The primary function of CCD is to collect the photo-generated electrons in its pixels (potential wells) during the CCD's exposure to radiation. The higher the intensity of light that is incident on a particular pixel, the higher the number of electrons that accumulate on that pixel. By varying the CCD gate voltages, the depth of the potential wells can be modified. In this way, electrons are transferred across the registers to the read-out circuit and the output signal is then transferred to further processing [3].

The CMOS image sensors (CIS) started to attract attention around mid-1980s and until early 1990s, the passive pixel sensor (PPS) was the dominant CIS technology [4]. The PPS had much lower performance than the CCDs and were replaced by the modern CMOS active pixel sensor (APS) [5, 6]. The addition of an amplifier in each pixel significantly increases the sensor speed and improves signal-to-noise ratio (SNR). Still, the early APS were too large for commercial viability, due to the larger technology nodes. As the technology continued to down-scale, it enabled integration of an analog-to-digital converter (ADC) at each pixel, providing fast readout and enabling new imaging applications that required wider dynamic range [7]. CIS convert optical signal into digital signal, which can be further processed into an image. CIS designs usually include four-transistor (4T) pixel, where the sensing device is a pinned photodiode. Main parameters of a CIS are quantum efficiency (QE), linearity, SNR, dark current and capacitance. The quantum efficiency defines the conversion between the incoming photons and the generated minority electrons, in the form of collection efficiency of the photodiode. Spectral responsivity gives a ratio of output photocurrent versus the input optical

power. Noise is an important photodiode parameter, as it defines the optical and thermal noise components, therefore determining the dynamic range of a detector. In radiation environment, dark current is an important parameter, as it increases after irradiation exposure, resulting in degraded CIS performance. [8]. Photodiode capacitance mainly affects the transient response of the photodiode and is defined by the p-n junction width.

Major issues that CCD have over CIS are radiation softness, difficulty to achieve large array sizes, incompatibility of CCD with the requirements for instrument miniaturization, difficulty in increasing the spectral responsivity range of CCD, and difficulty in increasing the readout rate of CCD. The complexity of charge transfer in the CCD device, as compared to the CIS can be seen in Figure 1.1. [9]. The main difference in charge transfer comes from the fact that in CIS, charge to voltage conversion occurs within each individual pixel, whereas in the CCD, the charge from all pixels is collected in series and then converted into the voltage signal, resulting in a much slower response [9].

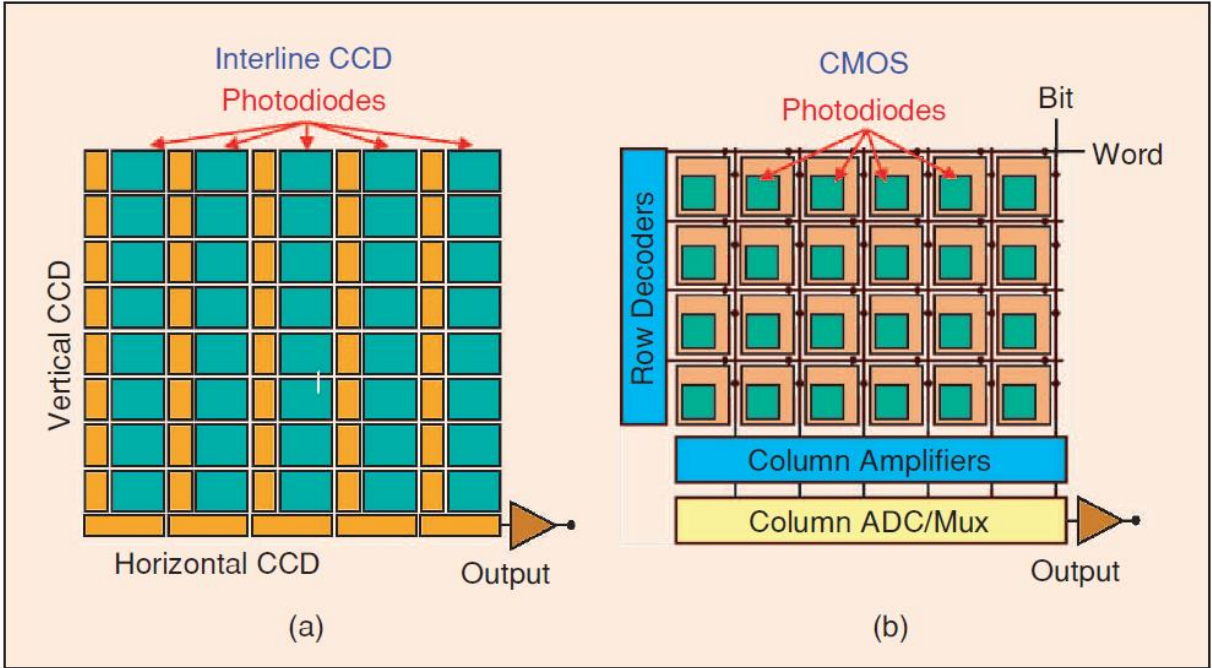


**Figure 1.1.** Comparison between the readout architectures of a) interline transfer CCD and b) CIS [9]. The main difference in charge transfer comes from the fact that in CIS, charge to voltage conversion occurs within each individual pixel, whereas in the CCD, the charge from all pixels is collected in series and then converted into the voltage signal, resulting in a much slower response.

On the other hand, active pixel sensor (APS) technology is more radiation hard, because of the intra-pixel charge transfer. They operate at lower temperatures and voltages, resulting in lower power consumption [10]. Additionally, compared to the CCD, the technology is more cost

efficient and offers on-chip functionality and compatibility with standard CMOS technologies, allowing monolithic integration of readout and signal processing electronics [11]. Furthermore, technology scaling allows CIS to easily be transferred to smaller technology nodes. As mentioned before, selective and high-speed readout offers flexibility and fast image acquisition [12-14]. The main drawback of CIS is the pixel fill factor and QE. Fill factor determines the effective photoactive area, which is reduced compared to the CCD due to having the readout inside the pixel. Moreover, the added noise from the readout and other noise sources reduces the dynamic range and limits the overall performance of the APS [15].

CIS are commonly implemented in medical, space and high energy physics applications like CT scanner, Large Hadron Collider (LHC) at CERN, etc. The main requirement for such sensors is radiation hardness against ionizing and non-ionizing radiation. For example, in the LHC, hybrid pixel detectors are implemented in the innermost layers for particle tracking. Hybrid detectors mean that the CMOS readout and the sensor come from different chips and are attached by using pitch bump-bonding. This allows for separate optimization of both components. In addition, full depletion of the sensing layer can be achieved by applying large bias voltages, leading to an efficient and fast charge collection, thus improving the radiation tolerance. Main disadvantages of the hybrid pixels are the complexity of the bump-bonding technology and the high cost of the material. On the other hand, monolithic active pixel sensors (MAPS) allow for very thin detectors as the sensor and the readout electronics are integrated inside the same silicon die, thus avoiding the bump-bonding design. Additionally, standard CMOS processes can be used, making the MAPS technology very cost effective. Their main disadvantage is lower radiation hardness and smaller charge collection time [16]. A cross-section of a MAPS detector is shown in Figure 1.2, where the CMOS readout is integrated with the collection electrode [17]. Cross-section of a depleted MAPS (DMAPS) structure with silicon-on-insulator (SOI) technology is depicted in Figure 1.3. In such a structure, additional isolation is needed to shield the CMOS circuitry from the extended depletion region [18]. MAPS are usually based on epitaxial layers with standard resistivities. On the other hand, the DMAPS use a high-resistive substrate, which enables full depletion of the substrate. Fully depleted substrate improves charge collection, as it is dominated by drift mechanisms, resulting in a larger signal and higher radiation hardness than in MAPS. In order to shield the CMOS readout from the sensing layer, additional deep n-/p-well layers are needed. In the SOI technology, a buried oxide layer (BOX) separates the CMOS layer from the high-resistivity bulk. The downside of this technology is the radiation intolerance for harsher radiation environments, such as the high-luminosity-LHC (HL-LHC) at CERN [19].



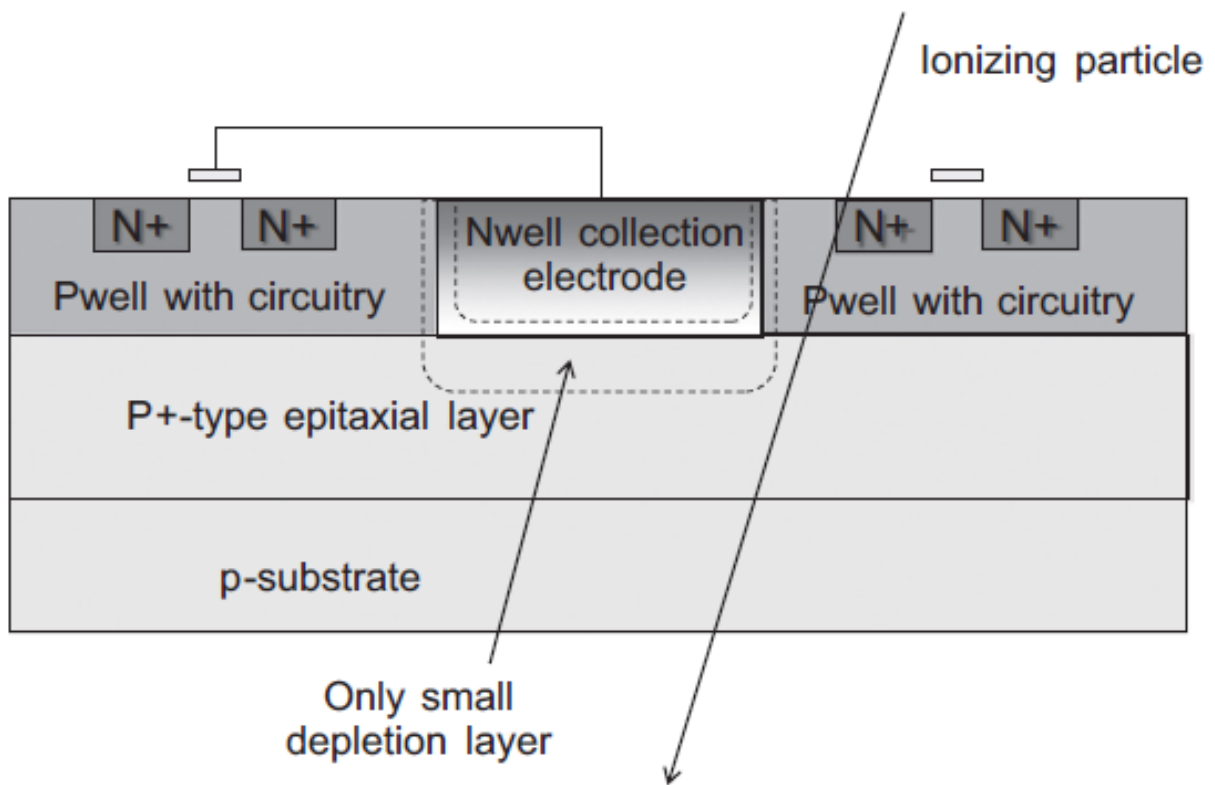


**Figure 1.2.** Cross-section of a monolithic active pixel sensors (MAPS) detector [17]. It consists of an N-Well (NW) collection electrode which is integrated with the read-out circuitry. The main disadvantage of a MAPS detector is the slow collection rate of the optically generated charge, as the expanding space charge region (SCR) from the p-n junction is not large enough to efficiently collect minority carriers.

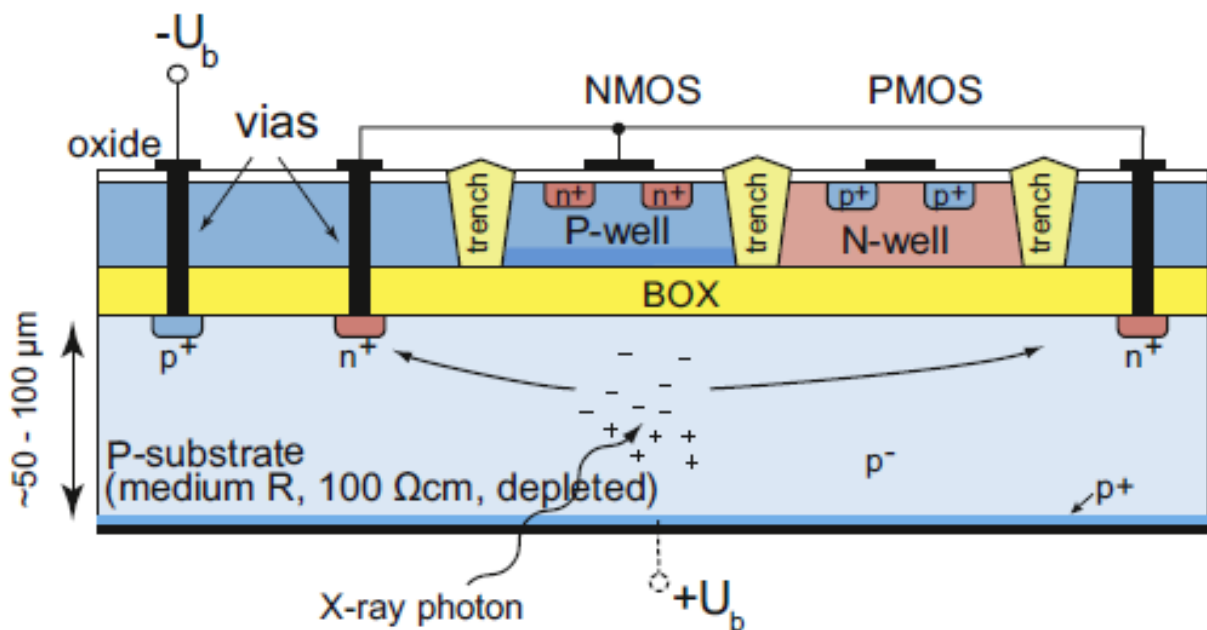


**Figure 1.3.** Cross-section of a depleted monolithic active pixel sensors (DMAPS) structure with silicon on insulator (SOI) technology [18]. The depleted charge collection volume is separated from the read-out circuitry by the buried oxide (BOX). The transistors of the read-out circuit are laterally isolated by trenches. Additionally, at the top surface of the BOX, in the P-Well (PW) region, a doped layer is

processed to further passivate the silicon/box interface. Depleted substrate enables fast and efficient charge collection, resulting in higher radiation hardness, compared to the standard MAPS structure.

## **1.1. CT scanner detectors**

CT scanners are medical apertures, in which a rotating X-ray tube is placed opposite of the detector array, which is used to create images of different tissues inside a human body. A Philips 8-cm measurement system composed of multiple modules of detector arrays is shown in Figure 1.4. [20]. Each module consists of multiple photodiodes, placed in an array to maximize the efficiency of the scanned element. Main characteristics of such photodiodes are high quantum efficiency, low crosstalk, high dynamic range good accuracy, stability and uniformity as well as the transient response and the geometric resolution, which is dominated by the photodiode size. Dynamic range is important as the signal in the photodiodes can vary over multiple orders of magnitude. Good accuracy is needed to measure small differences in tissue density, for example in brain imaging. Stability parameter implies that sensors have to produce the same signal for the same irradiation conditions between the scan and the system calibration. Photodiode uniformity over the pixel array means that all photodiodes in an array yield the same electrical signal after irradiation exposure. Furthermore, the transient response of the photodiode must be within the frame acquisition period, which is in the order of tens of microseconds. Finally, the photodiodes have to be radiation-hard against ionizing radiation [20]. An example of a detector module is depicted in Figure 1.5. [20].



**Figure 1.4.** Philips 8-cm data measurement system, composed of multiple detector array modules [20].

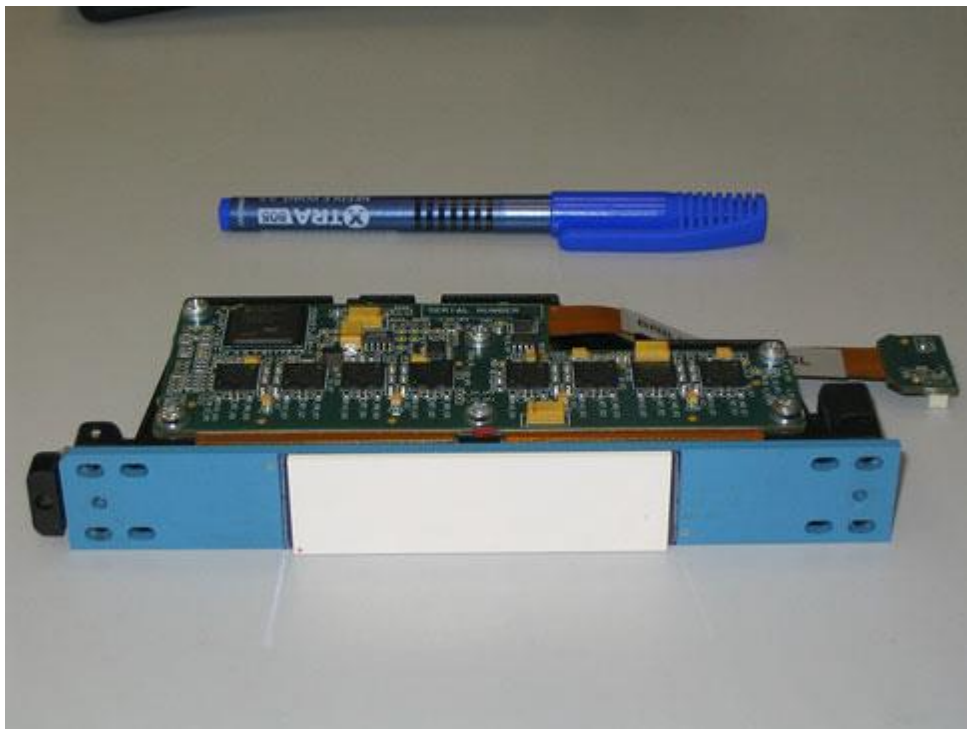


**Figure 1.5.** A detector module implemented in a CT scanner [20].

There are two principles of X-ray conversion to the electrical signal in semiconductor detectors: direct and indirect conversion, as depicted in Figure 1.6. [21]. In the direct conversion, X-rays directly reach the detector surface, creating charges as they propagate through the detector structure. Unfortunately, X-rays also create defects in the insulating layers and at the interfaces, i.e. at the silicon oxide/silicon interface in the case of silicon detectors.

On the other hand, indirect conversion includes an additional scintillator layer, placed above the detector that converts the high-energy X-ray photons to the low-energy visible light photons. There are many different scintillators, i.e. inorganic and ceramic scintillators, that find their usage relative to the environment they are used in. For example, in a CT scanner, ceramic scintillators made of gadolinium oxysulfide powder phosphors ( $Gd_2O_2S$ ) are used. The main requirements of such scintillators are high linear output, low afterglow, low radiation damage, high uniformity and chemical stability. Improving the light output of the scintillators would reduce X-ray exposure, thus the radiation damage [22, 23]. The photodiodes used in such detectors must be optimized for the visible light and near-infrared (NIR) spectrum (between 400 nm and 900 nm). The scintillator is not 100% efficient in converting the X-ray photons to higher wavelength photons, meaning that some of the X-rays reach the photodiode surface. They generate irradiation-induced defects that increase the surface recombination velocity, resulting in degradation of electrical and optical performances of the photodiodes [24-28].

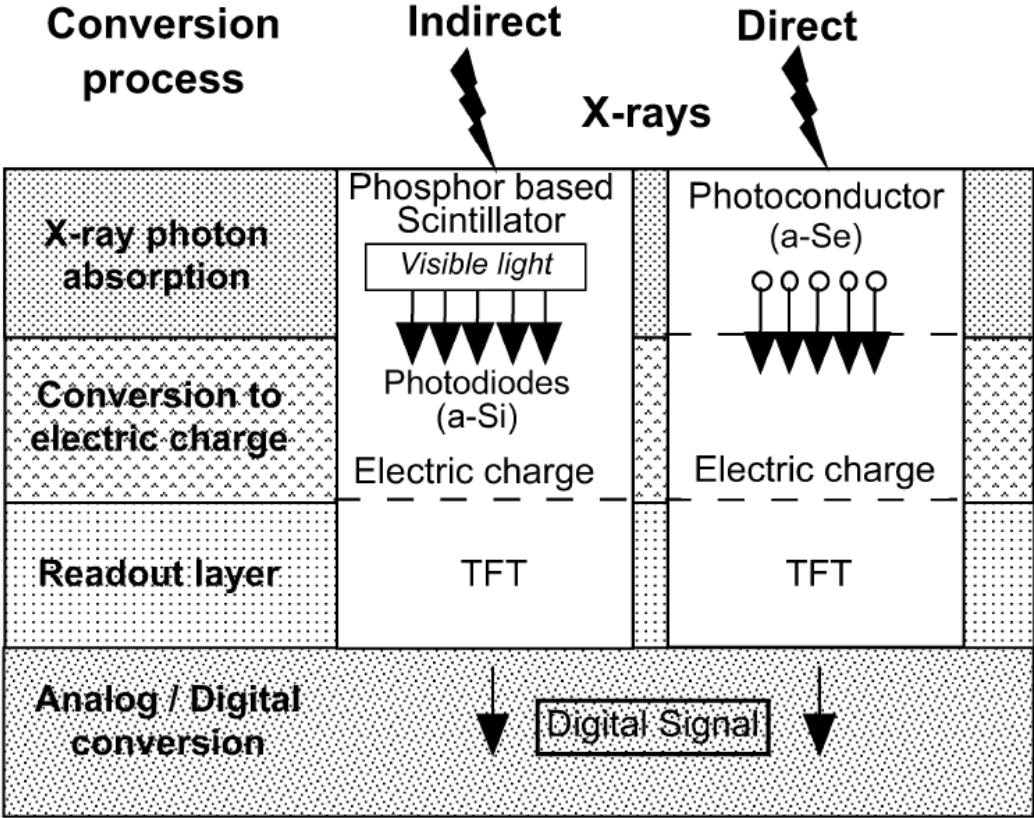


**Figure 1.6.** Comparison between indirect and direct X-ray conversion [21]. In direct conversion, X-rays directly reach the detector surface, creating charges as they propagate through the detector structure. Additionally, X-rays also create total ionizing dose (TID) induced defects in the insulating layers and at the interfaces, i.e. at the silicon oxide/silicon interface in the case of silicon detectors. On the other hand, indirect conversion includes an additional scintillator layer, placed above the detector that converts the high-energy X-ray photons to the low-energy visible light photons. Since the scintillator is not 100 % efficient in converting X-rays into visible light photons, a small fraction of X-rays will directly hit the photodiode surface, resulting in partial sensor degradation.

## 1.2. Radiation-hard photodiode concepts

There are multiple different variants of radiation-hard photodiode designs. For example, by changing from a larger to a smaller technology node, shallow-trench-isolation (STI) was used instead of a thermally grown local field oxide (LOCOS). Gated photodiodes were implemented to reduce the dark current after ionizing radiation exposure. Another solution is to integrate the pinned photodiode as it significantly reduces the dark current increase after the irradiation, if the distance between the STI and the junction is well selected [29, 30]. Additionally, highly-doped shallow p-type implant can be used to passivate the silicon-silicon oxide interface [31]. It was shown that due to total ionizing dose (TID) induced defects, the area below the insulating oxides becomes depleted, which leads to increased dark current. The best performance in terms of dark current after ionizing radiation was achieved for the highly-doped p-type layer surrounding the N-Well photodiode, as it prevents the space charge region (SCR) from reaching the insulating oxides [32].

In most cases, the sensor is implemented as a reverse biased p-n junction with the goal of increasing the SCR to efficiently collect optically generated carriers by drift mechanism [33, 34]. A common method of increasing the SCR is the full depletion of the low-doped epitaxial layer, which has benefit of fast and efficient charge collection, but simultaneously the dark current increases due to the Shockley-Read-Hall generation current, as it increases with increasing width of the SCR. On the other hand, high collection efficiency can be achieved without fully depleting the epitaxial layer by growing the epitaxial layers with high lifetime of minority carriers. This enables the carriers to be efficiently collected by diffusion mechanism, removing the need to fully deplete the epitaxial layer. Although, the diffusion is slower than drift, a partial depletion of epitaxial layer results in reduced dark current, while still maintaining satisfactory spectral responsivity and temporal resolution of such photodiodes [17].

Furthermore, thickness of the epitaxial layer heavily affects the optical performance of the photodiodes, and a photodiode cross-section, showing three collection electrodes, an epitaxial layer, and the substrate, is illustrated in Figure 1.7. The light-blue region between the substrate and the epitaxial layer is the out-diffusion region, present due to the gradient in doping profile at that junction. The SCR is present around the collection electrodes. In this example, the epitaxial thickness is varied between 14  $\mu\text{m}$  – 30  $\mu\text{m}$ . The penetration depth of the light into silicon substrate versus wavelength is shown in Figure 1.8.

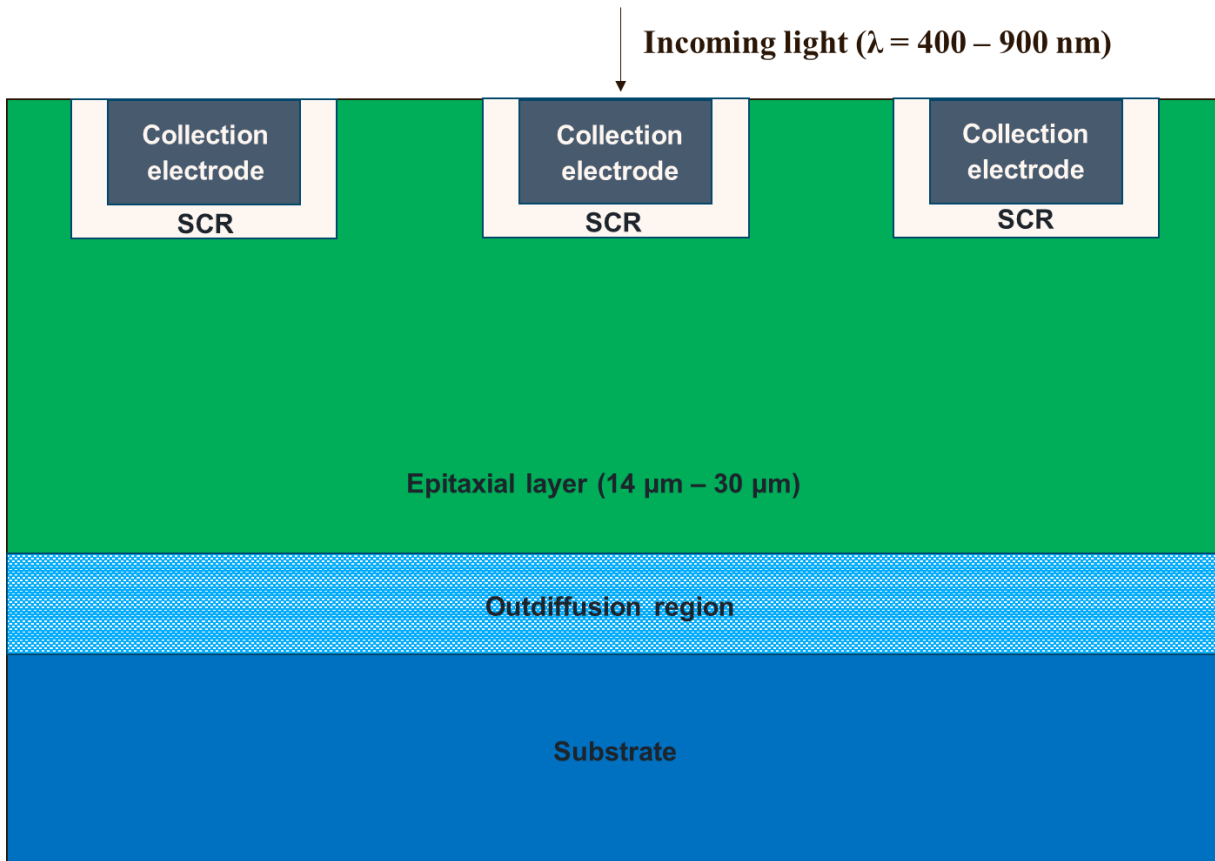


**Figure 1.7.** Illustration of a photodiode cross-section consisting of three collection electrodes, epitaxial layer, and the substrate. The epitaxial layer thickness is ranging from 14  $\mu\text{m}$  – 30  $\mu\text{m}$  and between the substrate and the epitaxial layer is the out-diffusion region, due to the gradient in doping profile between the substrate and the epitaxial layer.

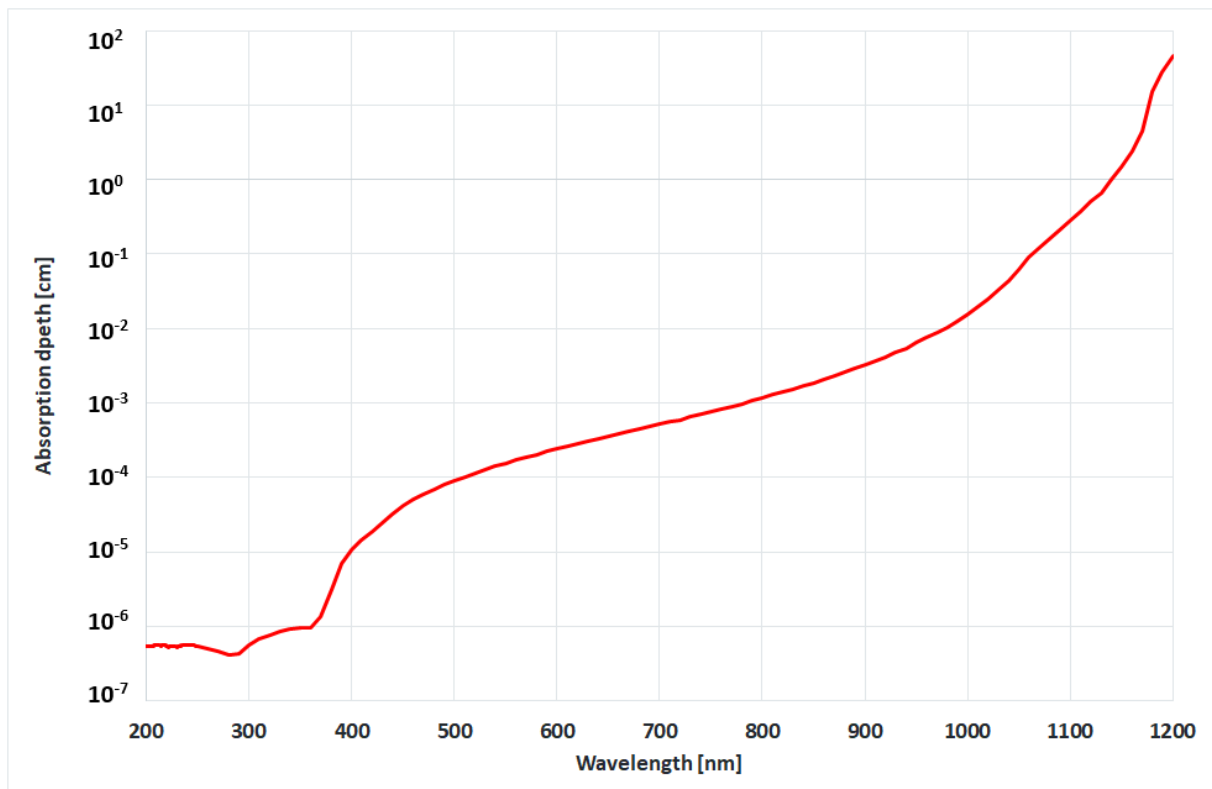


**Figure 1.8.** The penetration depth of light in silicon versus wavelength.

Spectral responsivity curves, in the spectrum range between 200 nm and 1200 nm, for different epitaxial thicknesses, are demonstrated in Figure 1.9. [35]. At lower wavelengths, up to 500 nm wavelength, the variability of the spectral responsivity is roughly 10% and is less affected by epitaxial thickness variability. This is because the absorption depth of the lower wavelength light is shallower, and the generated carriers are closer to the depletion region of the collection electrodes and are therefore affected more by the drift collection mechanism. On the other hand, for higher wavelengths, above 900 nm, the spectral responsivity alters up to 12-13% because of the deeper light absorption. In that situation, the majority of optically generated carriers end up in the substrate region, where the doping concentration is much higher, increasing the recombination rate of the minority carriers, thus decreasing spectral responsivity. In addition to that, due to the gradient in the doping profile and the resulting electric field in the out-diffusion region, the optically generated minority carriers are pushed away from the substrate and towards the collection electrode. For thinner epitaxial layers, the effective quasi-neutral region is smaller, and since the out-diffusion region is repelling the minority carriers towards the collection electrodes, there is a higher chance for them to be collected by the collection electrodes, resulting in higher responsivity in the spectrum range between 500 nm and 900 nm, compared to thicker epitaxial layers. In order to have a higher spectral responsivity for near-infrared (NIR) spectral range, a thicker epitaxial layer is needed [35]. On the other hand, the diffusion current component of the dark current increases if the epitaxial thickness increases, resulting in a higher total dark current. Furthermore, diffusion current is dominantly affected by the temperature conditions of the application, hence the increase of the dark current can be limited if the operated temperature decreases.

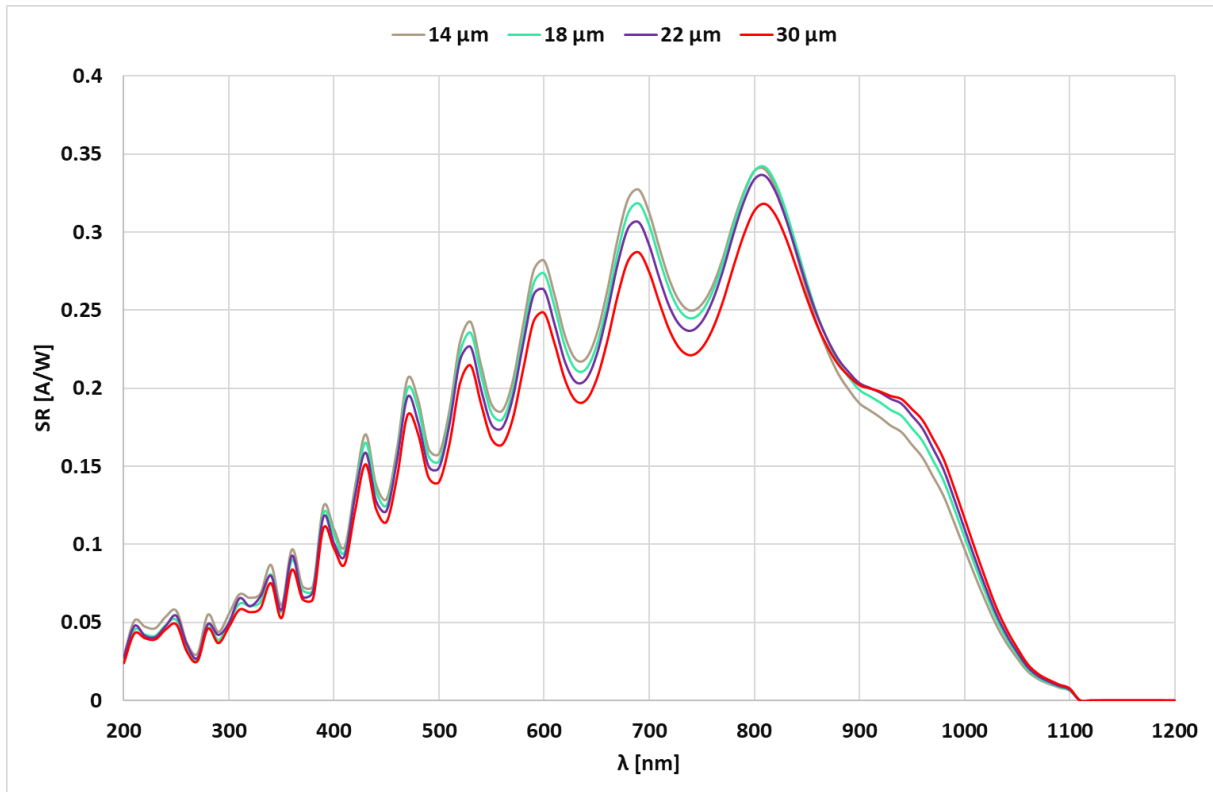


**Figure 1.9.** Spectral responsivity curves, for wavelength spectrum between 200 nm and 1200 nm, for different epitaxial thicknesses (14  $\mu\text{m}$  – 30  $\mu\text{m}$ ) [35]. At lower wavelengths, up to 500 nm wavelength, the variability of the spectral responsivity is roughly 10%, whereas above 900 nm, the spectral responsivity alters up to 12-13%.

In this dissertation, the effects of the ionizing radiation, caused by X-ray irradiation, on silicon photodiodes are defined and analyzed. A photodiode test-chip is designed and fabricated in *ams OSRAM* 180 nm CMOS technology. The limited active-area size in 180 nm technology required the photoactive region to be segmented into smaller areas. The division of the photoactive area was achieved by implementing thin STI cut-lines. In three photodiode structures, the optimization of the active area was done by equidistantly placing the STI lines between the two neighbouring islands. In the case of the fourth photodiode structure, the STI area was minimized, but the spacing between the STI and the nearest island was not constant. Furthermore, a shallow p-type implant was introduced with the goal of passivating the STI/silicon interface and improving the radiation hardness of the photodiodes.

The measurement characterization shown that the proposed detectors are radiation-hard up to TID = 200 Gy(Si), whereas after TID = 400 Gy(Si), the dark current degraded between 10 – 16 %, the spectral responsivity decreased by  $\sim$  2%, while the photodiode capacitance remained intact. A comparison between two similar photodiodes fabricated in 180 nm and 350 nm *ams OSRAM* CMOS technologies is presented as well. The analysis showed that the devices fabricated in the smaller technology node are more radiation-hard, even after twice as



high TID, compared to the detectors fabricated in 350 nm technology node. The drawback of the STI lines was a slight increase of the dark current before irradiation, resulting in a higher dark current, compared to the devices fabricated in 350 nm technology. Furthermore, in 180 nm technology, a thin nitride layer is processed that acted as an anti-reflective coating (ARC) layer, enhancing the optical performance of the analyzed photodiodes.

Additionally, the sources of electrical and optical characteristics degradation by X-ray irradiation are identified and their effect is modeled and analyzed by TCAD simulations.

A possible explanation for higher radiation hardness in 180 nm technology could be the additional trapping of positive charges in the nitride layer, that compensates the effect of the interface traps. Additionally, small differences in other parameters, such as differences in thermal budget and in the doping profiles further contribute to the radiation hardness of the photodiodes processed in 180 nm technology.

## 2. Radiation damage in silicon structures

Radiation damage in semiconductor sensors alters the response and degrades the performance of many devices ultimately limiting their stability and lifetime. Moreover the damage can significantly increase the detector noise and degrade other electrical properties such as dark current [27]. Radiation effects are grouped in cumulative and single event effects (SEE). Cumulative effects are gradual effects taking place during the whole lifetime of the electronics exposed in a radiation environment. A device sensitive to TID or displacement damage will exhibit failure in a radiation environment when the accumulated TID (or particle fluence) has reached its tolerance limit. On the other hand, single event effects are due to the energy deposited by one single particle in the electronic device. They can happen in any moment, and their probability is expressed in terms of cross-section [36]. In the following chapters, a short introduction to ionizing irradiation is given. It covers the interaction of ionizing irradiation particles with the semiconductor structures processed in *ams OSRAM* 180 nm CMOS technology. Furthermore, radiation-induced defects like fixed charges in the insulating layers, as well as the interface traps at the silicon oxide/silicon interface are closely examined. Finally, the theory and the models presented in this chapter will be used in modeling of the TID-induced defects in chapter 7, where TCAD software is used to calibrate different electrical and optical simulations with the wafer-level measurements.

### 2.1. Total ionizing dose induced defects

Ionizing radiation is caused by charged particles and photons with high energy. Apart from creating electron-hole pairs in the silicon structure, ionizing radiation also forms charge carriers in insulating layers (e.g. SiO<sub>2</sub>) where some of them are trapped, leading to charge buildup [37]. The holes in the oxide have a very low mobility and can get trapped near the Si-SiO<sub>2</sub> interface. This causes the electrons to accumulate near the interface, potentially depleting the photodiode surface, thus increasing the photodiode dark current. In chapter 7.8, it is shown that the radiation induced trapped positive charges in the insulating layers extend the space charge region (SCR) at the oxide interface, leading to an enhancement of interface state Shockley-Read-Hall (SRH) generation current.

Both interface traps and trapped positive charges play an important role in the photodiode performance degradation. Figure 2.1. shows a band diagram of a Metal-Oxide-Semiconductor (MOS) structure with highlighted TID induced defects [38]. When a high-energy particle, in this case an X-ray photon, interacts with a MOS structure, electron-hole pairs are created through its trajectory. The generated carriers can generate additional charge pairs if their energy

is higher than the minimum required energy for charge-pair generation. In the silicon oxide, as soon as the charges are generated, some of the electrons and holes will recombine. For a positive bias applied at the gate, the remaining electrons will quickly drift towards the gate, in picosecond time frame. On the other hand, the remaining holes, which is called the hole yield, will slowly start to drift towards the interface with the silicon. The hole transport is highly dispersive in nature and heavily depends on the temperature conditions. At room temperature, the transport takes place over multiple decades in time, ranging from hundreds of nanoseconds to seconds, and much slower at lower temperatures [39-41]. At the SiO<sub>2</sub>/Si interface, on the oxide side, the accumulated holes act as an added density of fixed positive charges. Furthermore, some of the accumulated positive charges can react at the interface, resulting in generation of the interface traps along the interface on the silicon side.

The TID induced defects increase the surface recombination rate, widen the SCR and can trap optically generated minority carriers, resulting in degradation of electrical and optical performances of the photodiode. The following three sections will describe in more details the mechanisms behind the transport of holes in the oxide and the accumulation of oxide charges and the creation of interface traps.

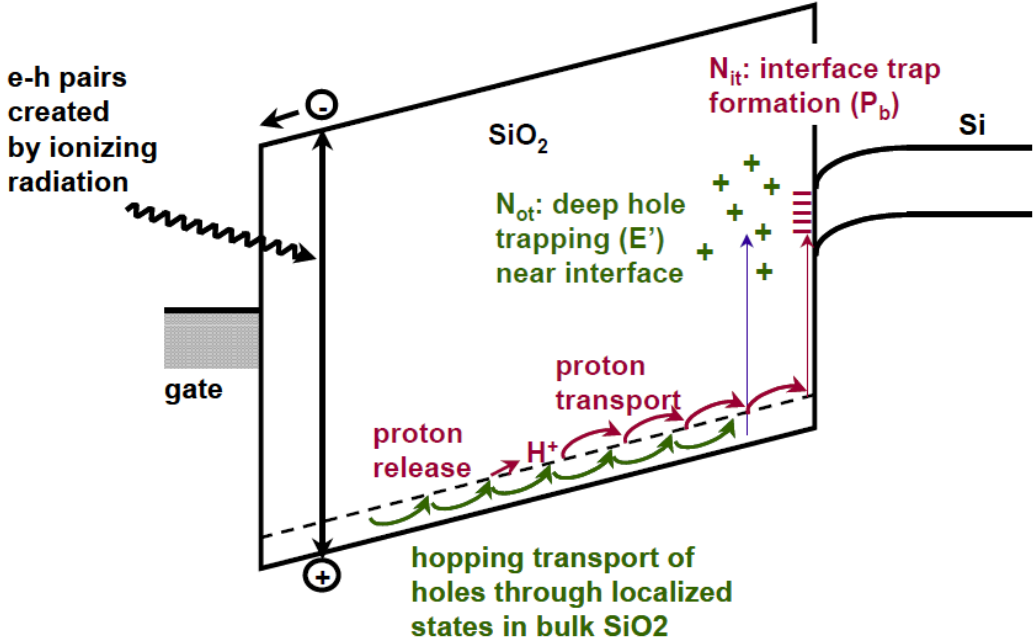


**Figure 2.1.** Band diagram of a MOS structure with a positive bias applied to the gate, illustrating the generation of TID-induced defects [38]. After the charge-pair generation, remaining unrecombined holes are traveling towards the SiO<sub>2</sub>/Si interface, where they accumulate and help creating interface traps on the silicon side of the interface.

### 2.1.1. Hole charge yield

The fraction of holes that escape the initial recombination is called the hole charge yield. The hole yield depends on the electric field in the oxide as well as on the irradiation particle. The electric field is separating the generated electron-holes pairs, whereas the irradiation particle defines the charge-pair line density. The line density of the generated charge pairs describes how dense the electron-hole pairs are generated over the trajectory of the incoming irradiation particle. It is determined by the linear energy transfer (LET), which is a measure of energy loss of a particle per unit length of the particle trajectory. The LET is in fact the stopping power of the incoming ionizing irradiation particles. The irradiation particles are divided into low-LET and high-LET particles. The low-LET particles include X-rays, gamma rays, and high-energy electrons. On the other hand, protons, alpha particles and other heavier ions are the high-LET particles. For particles that generate dense clusters of charge pairs, like the high-LET particles, the separation distance is in the range of 0.3 nm for 1 MeV protons, thus the initial recombination is relatively high. On the other hand, the low-LET particles generate a lighter amount of charge carriers, with the average separating distance in the range of 50 nm for 1 MeV electrons, resulting in a lower initial recombination rate [42, 43].

There are two models that describe the initial recombination of the generated charges in the oxide: the geminate and the columnar model, as shown in Figures 2.2. a) and b) respectively [42]. The thermalization distance, highlighted as the radius,  $r_1$ , defines the average separation distance between the generated electron and the generated hole of the same pair, after they have dissipated their excess kinetic energy and reached thermal equilibrium energies. The average thermalization distance is  $\sim 5$  nm for silicon oxide [44, 45]. The geminate model describes the recombination model for low-LET particles, as the separation distance is much greater than the thermalization distance. In this case, the recombination can be considered between separate electron-hole pairs. On the other hand, in the columnar model, the opposite is the case, as for the high-LET particles the separation distance is much smaller than the thermalization distance. In such a situation, the recombination between many overlapping electron-hole pairs is considered, and the hole yield is much smaller than in the geminate model [45].

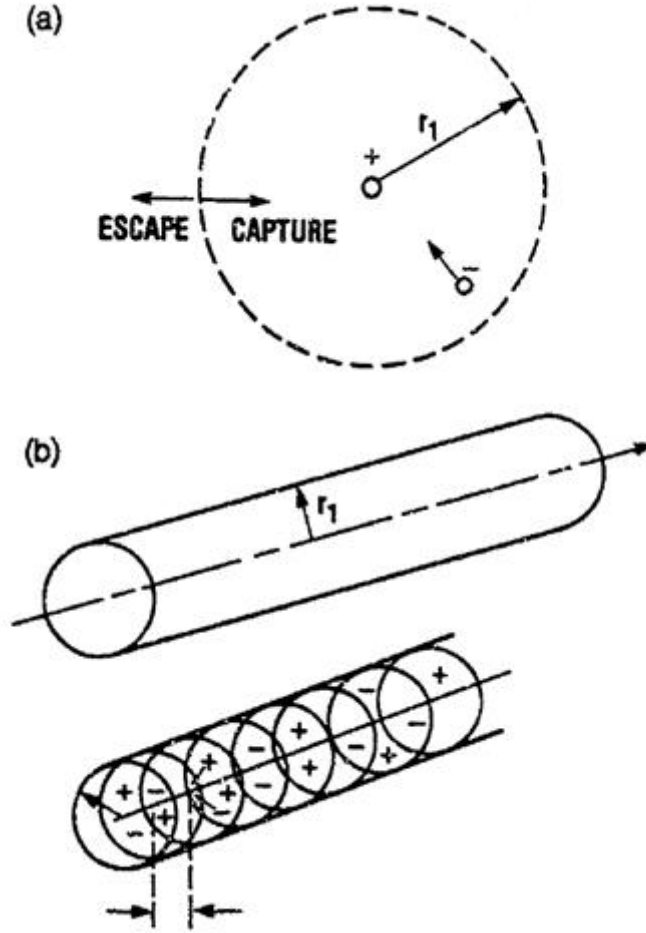


**Figure. 2.2.** Initial recombination models: a) geminate and b) columnar [42]. The geminate model is used to describe low-LET particles, such as X-rays, gamma rays and high energy electrons. The columnar model describes interactions of high-LET particles, such as protons, alpha particles and other heavy ions, with the silicon oxide.

A comparison of charge yield between different irradiation particles (Co-60 gamma rays, 10 keV X-rays, low-energy protons and alpha particles) is shown in Figure 2.3. [38]. The function of unrecombined holes is used to calculate the total number of accumulated fixed positive charges in the oxide:

$$N_{holes} = f(E_{oxide}) \cdot g_0 \cdot D \cdot t_{oxide}, \quad (2.1)$$

where  $f(E_{oxide})$  is the field-dependent hole charge yield in absolute values,  $g_0$  [*charge pairs* ·  $rad^{-1} \cdot cm^{-3}$ ] is a material-specific parameter describing the initially generated charge-pair density per rad of dose,  $D$  [ $rad$ ] is the dose and  $t_{oxide}$  [ $cm$ ] is the thickness of the silicon oxide [46]. The  $g_0$  is dependent on the electron-hole pair creation energy, which is in the range of  $17 \text{ eV} \pm 1 \text{ eV}$  for  $SiO_2$  [47]. This equation will be used later, in chapter 7.5, in the modeling of TID defects in the TCAD environment.

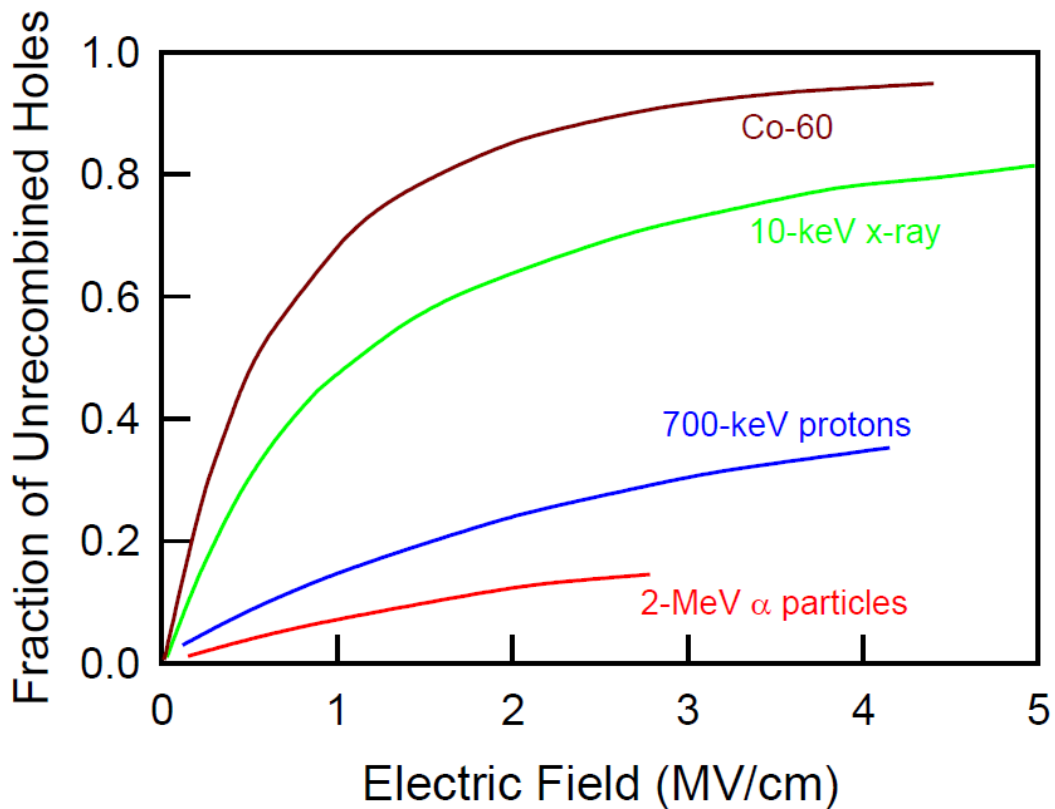


**Figure 2.3.** Fraction of unrecombined holes (yield charge) versus electric field in the oxide, with respect to different irradiation particles: gamma rays, X-rays, low-energy protons and alpha particles [38].

### 2.1.2. Fixed charges in the insulating layers

As mentioned before, for a positive bias, the fraction of generated holes, which escape initial recombination, start to move towards the silicon-oxide/silicon interface. As depicted in Figure 2.1., the hole transport is achieved by moving through localized states, via „polaron hopping“ phenomena [25]. The process is highly dispersive, occurring over many decades in time after the irradiation, affected by the changes in the electric field, temperature and the oxide thickness. Polarons describe interaction between charge carriers and their distorted potential field, where the effective mass of charge carriers, in this case holes, increases and their mobility decreases [48]. By causing distortions in the local potential field of the oxide lattice, the depth of local traps increases, resulting in trapped holes in the localized states. Due to that, the hole transport is quite slow and can last over multiple decades in time after irradiation. Additionally, polaron hopping is dependent on the temperature and oxide thickness [49, 50]. Once the holes are close to the silicon/silicon oxide interface, a fraction of holes can get trapped in the oxide vacancies [51], which act as trapping centers. Trapping of holes depends mainly on the capture

cross-section at the interface. The capture cross-section is strongly dependent on the electric field present in the oxide and the quality of the processed oxide [52-58].

Even though the fixed charges in the oxide are relatively stable, they are constantly annealing, and at room temperature it can take up to years until all the charges are annealed. In general, annealing is dependent on time, temperature and applied electric field in the oxide. At room temperature, tunneling of electrons from the silicon is the dominant mechanism for annealing the fixed charges in the oxide [59-68]. At higher temperatures, above 100°C, thermal emission of electrons from the oxide valence band into the traps will become the dominant effect [69-80]. Additionally, by applying a positive bias during annealing, the process can be further enhanced. On the other hand, applying a negative bias afterwards can lead to partial restoration of the fixed charges in the oxide. The passivating electrons can tunnel back into the silicon substrate, thus recovering some of the fixed charges in the oxide. [81].

### **2.1.3. Interface traps at the silicon/insulator interface**

Once the holes reach the interface with the silicon, some of them may react with the passivating hydrogen atoms, thus creating the interface traps on the silicon side of the interface. These defects are localized deep-level traps in the silicon bandgap and their occupancy is determined by the Fermi level, as shown in Figure 2.1. These traps can be positive, negative or neutral, depending on their energy level, relative to the Fermi level energy. If the trap energy is above the Fermi level, the traps would act as donors, and such would be positively charged. In the opposite situation, where the Fermi level is above the trap energy, they would act as acceptors, hence being negatively charged. Around the midgap, the traps are neutral [82-85].

Two temperature-dependent mechanisms play a role in generation of interface traps: diffusion of neutral hydrogen and proton transport. It was shown that at lower temperatures, between 120 K and 150 K, the generation of interface traps is mainly affected by neutral hydrogen diffusion, whereas at temperatures above 200K, proton transport is the main mechanism for interface trap buildup, the latter being the overall dominant process [86, 87].

Compared to the accumulation of fixed charges in the oxide, buildup of interface traps is a much slower process. Saturation of interface traps can last longer than thousands of seconds after TID exposure [88, 89]. The determining factor in the interface trap buildup is the transport time frame of the protons along the interface. The average hopping distance for protons is reported to be 0.26 nm, corresponding to the average distance between the oxygen atoms. Furthermore, the activation energy needed for interface trap creation is reported to be 0.82 eV [90-92]. Both the fixed charges in the oxide and the interface traps share similar dependence to

the electric field, implying that they are both linked to the hole trapping at the SiO<sub>2</sub>/Si interface [93].

Interface traps require much higher temperatures for annealing, usually above 150 °C, than the fixed charges in the oxide. The annealing of traps heavily depends on the interface quality, and in some cases the annealing temperature can go up to 300 °C. In addition to the thermal annealing, other radiation hardening techniques include surface passivation by shallow highly-doped implants and other process and layout optimizations [24, 27, 30, 94-101].

## **2.2. Summary**

After the X-ray exposure, TID induced defects are generated in the insulating layers and at the insulator/silicon interface in the silicon photodiode structures. There are two types of defects that degrade the performance of the optical sensors: the fixed positive charges in the insulating layers and the interface traps at the insulator/silicon interface. The fixed positive charges are accumulated holes in the insulating layers, close to the interface with silicon. These fixed charges contribute to the generation of interface traps, which are deep-level defects present on the silicon side at the insulator/silicon interface. Due to these defects, the surface recombination rate is increased, resulting in an increased dark current after X-ray exposure. Additionally, in the un-passivated silicon surfaces, optically generated minority electrons can get trapped which results in reduction of optical performance of the silicon photodiodes. Radiation hardening techniques include thermal annealing at high temperatures, surface passivation by shallow highly-doped implants and other process and layout optimizations.



### 3. Design of radiation-hard photodiodes in *ams OSRAM* 180 nm CMOS technology

In the following chapter, a photodiode concept, fabricated in *ams OSRAM* 180nm CMOS technology, is presented. First, a short introduction about the starting material is given, where the wafer map is shown, indicating four quadrants on the wafer. Afterwards, the photodiode test-chip is shown, where the *ams OSRAM* 180 nm CMOS technology is introduced. Furthermore, a cross-section of the proposed photodiode structure is given with highlighted photodiode regions. Finally, layouts of four similar photodiode structures are shown, each with different STI over photoactive (PA) region ratio.

#### 3.1. Starting material

Wafers used in the test-chip fabrication consist of a low-doped, p-type epitaxial layer ( $\rho_{\text{epi}} \approx 19 \text{ } \Omega\text{cm}$ ,  $t_{\text{epi}} = 18 \text{ } \mu\text{m}$ ), which is thermally grown on top of the p-type substrate ( $\rho_{\text{sub}} \approx 0.03 \text{ } \Omega\text{cm}$ ). Furthermore, the epitaxial layer has a special high-lifetime of minority electrons feature,  $\tau = 1 \text{ ms}$ , which is used in order to provide sufficiently long diffusion length for the optically generated carriers. Long diffusion length enables the optically generated carriers to be efficiently collected by diffusion mechanism.

Wafer map, with highlighted quadrants, as well as the central die and the central vertical and horizontal dies is shown in Figure 3.1. Each wafer quadrant is specific in regard to the TID it received during X-ray exposure, further discussed in chapter 4. Wafer notch is also visible, which defines the wafer orientation and helps with specifying the correct dies for the X-ray irradiation experiment. Furthermore, on the bottom right quadrant, the shallow p-type implant (SPI), was omitted due to non-standard processing. The impact of omitting the SPI on the post-irradiation spectral responsivity characteristics will be discussed in chapters 5.2.3. and 7.6., where the post-irradiation optical wafer-level measurements are discussed and a TCAD simulation comparison between the SPI and non-SPI surface passivation is given.

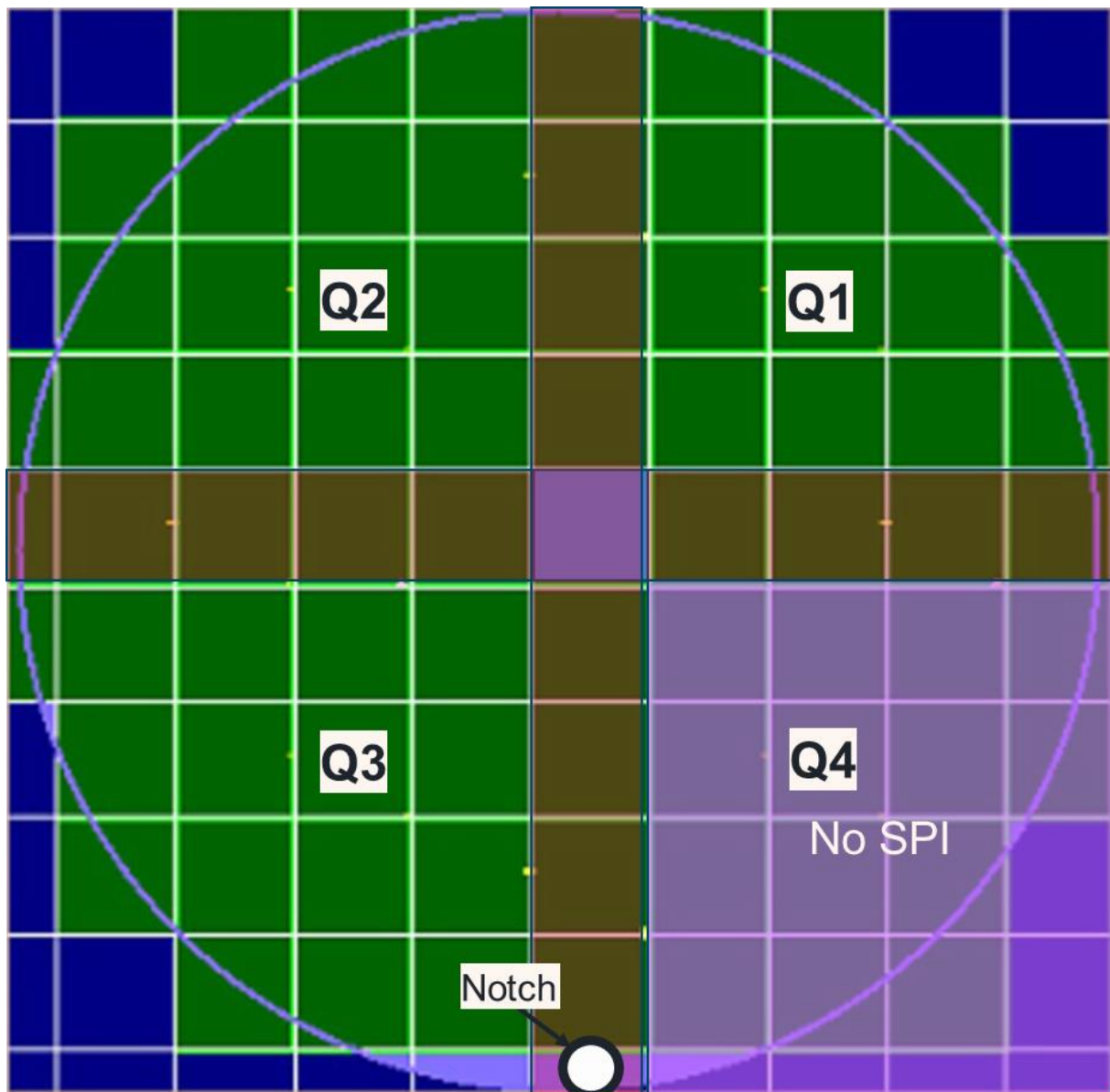


**Figure 3.1.** Wafer map indicating the four quadrants. Each quadrant is specific in regard to the Total Ionizing Dose (TID) it received during X-ray exposure. Wafer notch is visible on the bottom side, indicating the wafer orientation. Bottom right quadrant did not receive the shallow p-type (SPI) due to non-standard processing.

### 3.2. Photodiode test-chip

The prototype photodiode structure, processed in 350 nm CMOS technology, is used as a reference structure with the goal to down-scale it to 180 nm technology. The 350 nm *ams OSRAM* process node is a 3.3V/5V, 2-poly and 4-metal layer mixed signal technology. The 180 nm *ams OSRAM* process node is a 1.8V/5V, 1-poly and 6-metal layer mixed signal technology. For the purpose of optimization, multiple photodiode variants were designed and tested. The size of the structures in both technologies is  $600\ \mu\text{m} \times 800\ \mu\text{m}$ . The layout of the photodiode processed in 180 nm technology is shown in Figure 3.2, and consists of 242 n-well

(NW) islands, surrounded by the p/n/p-type guard-ring [102]. NW islands act as collection electrodes for the photo-generated carriers. Additionally, STI cut-lines were implemented in order to divide the fabricated active area into smaller segments, thus avoiding misprocessing due to active area size restrictions in 180 nm technology. Horizontal, vertical and diagonal spacings between the islands are kept constant, as well as the spacing between the STI and the nearest NW islands.

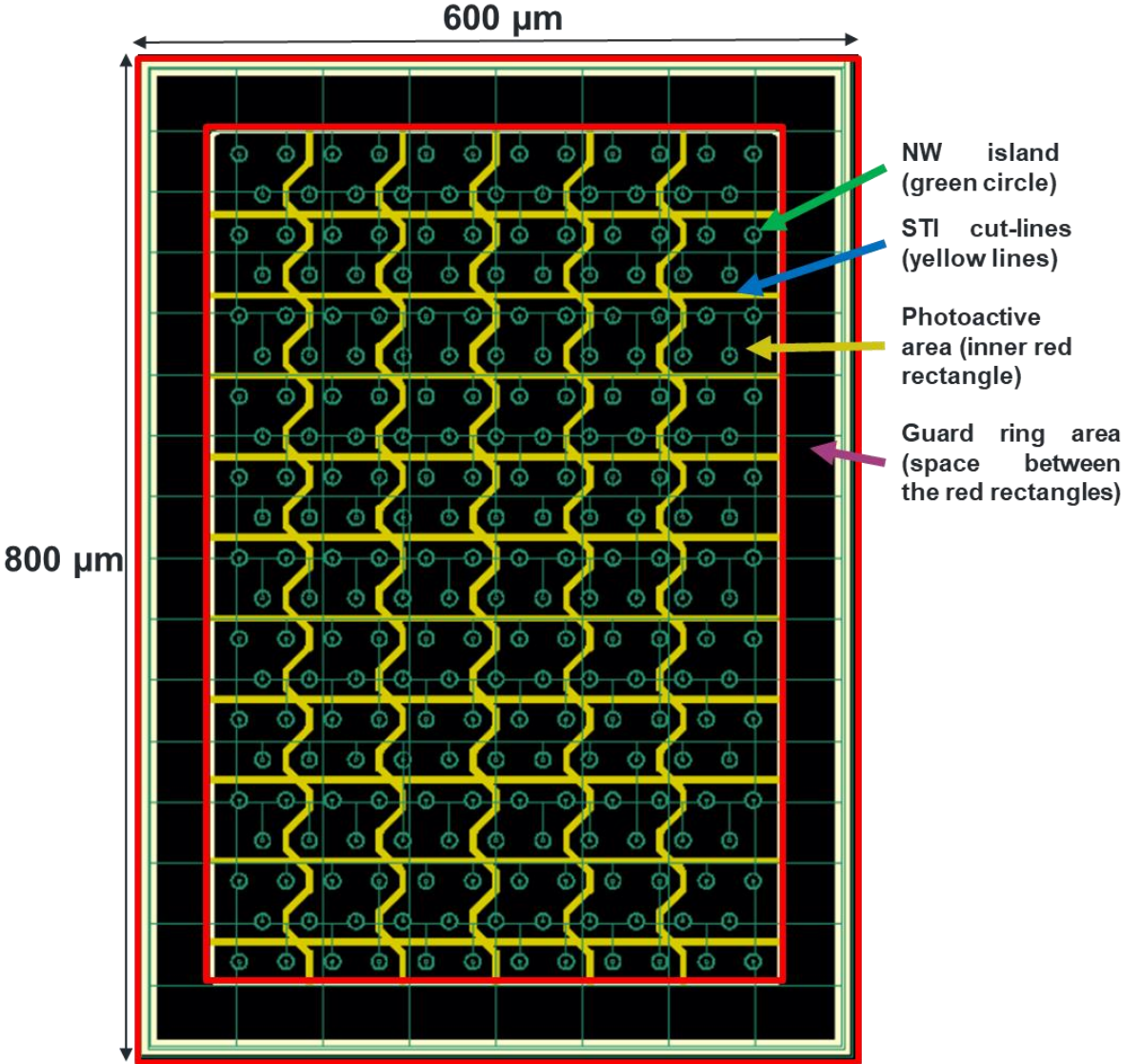


**Figure 3.2.** Layout of the photodiode structure designed and processed in *ams OSRAM* 180 nm CMOS technology. The photodiode consists of 242 N-Well (NW) islands and it is surrounded by the p/n/p-type guard-ring. Yellow lines are the shallow trench isolation (STI) cut-lines, used to divide the active-area into smaller segments to allow correct processing. Horizontal, vertical and diagonal spacings between the islands are kept constant, as well as the spacing between the STI and the nearest NW islands [102].

The cross-section of one island, its periphery and the guard-ring is shown in Figure 3.3. [102]. The NW island is surrounded by a highly-doped p-type layer ( $N_A > 10^{20} \text{ cm}^{-3}$ ), which

acts as a passivation layer such that the electrons do not accumulate at the SiO<sub>2</sub>/Si interface. In order to harden the region below the STI, another SPI with an acceptor doping of  $N_A > 10^{17} \text{ cm}^{-3}$ , two orders of magnitude higher than the epitaxial layer doping, was used to prevent the depletion under STI. The SPI processing step is taken from 350 nm technology and was adjusted for fabrication in 180 nm CMOS technology [102]. Since the SPI is not a standard-process option, one quadrant of the wafer was not processed with it. The p/n/p-type guard-ring surrounds the photoactive area and is partially covered by the metal lines. The positive operating voltage of 1.25 V, determined by the readout amplifier, is applied to the cathode contact, whereas the anode and the guard-ring contacts are grounded.

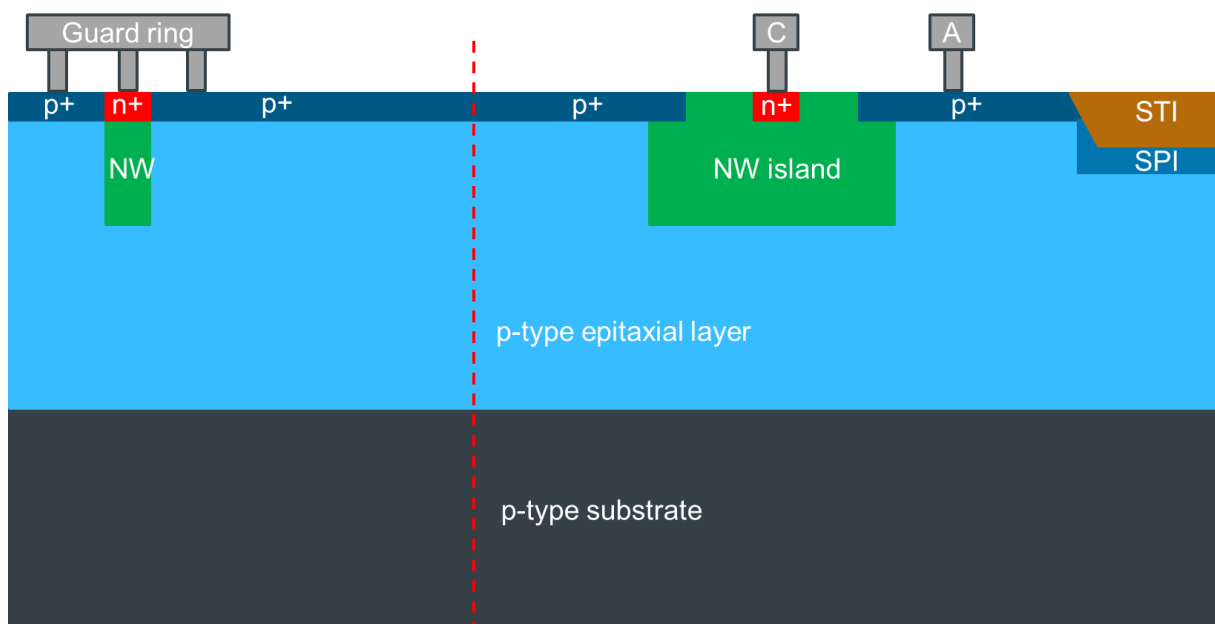


**Figure 3.3.** Cross-section of the photodiode structure with the layout shown in Figure 3.2, depicting one N-Well (NW) island, its periphery and the guard-ring area. Dashed red line separates the photoactive area (where the NW islands are placed) and the guard-ring area. The shallow trench isolation (STI) represents half of the yellow line from Figure 3.2, and the SPI represents the shallow p-type implant below the STI. Anode and cathode contacts are highlighted by „A“ and „C“ respectively. Photodiode operating voltage is 1.25V in reverse bias, with the anode and guard-ring contacts grounded [102].

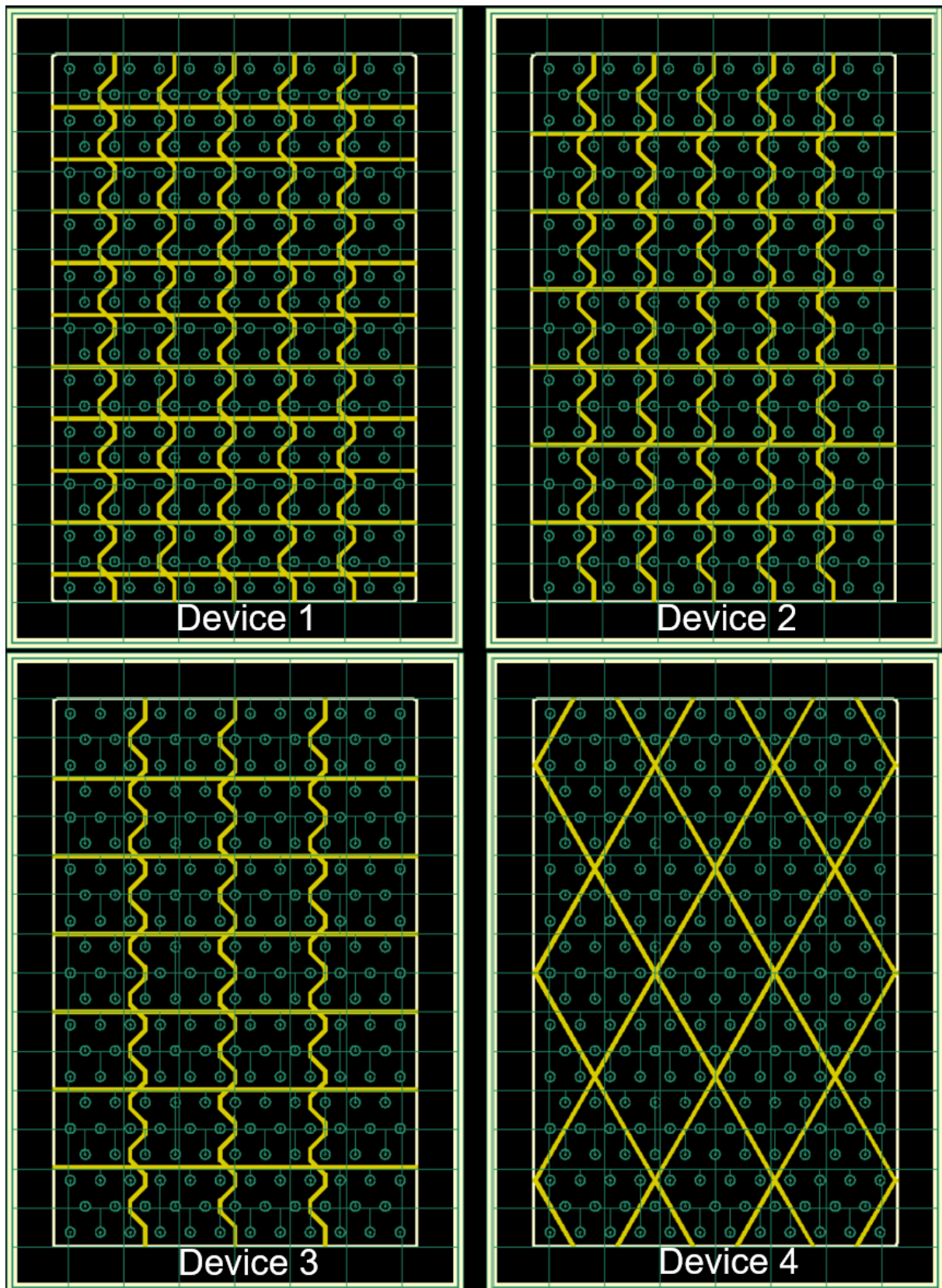


**Figure 3.4.** The layouts of four photodiode design versions. The difference between the structures is in shallow trench isolation (STI) distribution over the photoactive area (PA). Devices 1-3 have constant spacing between the STI and the nearest islands, whereas the fourth device has diagonally placed STI lines which resulted in the smallest STI coverage of the photoactive area and inconsistent spacing between STI and N-Well (NW) islands [102].

Four versions of photodiodes are designed, and their layouts are shown in Figure 3.4. [102]. The STI to photoactive area ratios for the four photodiodes are summarized in Table 3.1 [102]. The difference between all structures is in the density and position of the STI regions. Additionally, devices 1-3 have constant spacing between the STI and the nearest islands, whereas the fourth device has diagonally placed STI lines which resulted in the smallest STI coverage of the photoactive area, but inconsistent spacing between STI and NW islands [102]. The performance of each photodiode structure, in regard to the dark current, capacitance and spectral responsivity characteristics will be analyzed and discussed in the next few chapters, where the wafer-level measurements, before and after X-ray irradiation, are analyzed in more detail.

**Table 3.1:** Shallow trench isolation (STI) to photoactive area (PA) ratio for the four photodiode versions. Devices 1-3 have constant spacing between the closest island and the STI cut-lines, whereas device 4 has diagonally placed STI cut-lines to minimize the STI to photoactive area ratio [102].

Device #	STI/PA ratio [%]
Device 1	5.79
Device 2	4.61
Device 3	3.50
Device 4	3.18

### 3.3. Summary

In the design of a radiation-hard photodiode test-chip, a special starting material was used that consisted of an 18  $\mu\text{m}$  low doped p-type epitaxial layer which was grown on top of the low resistive p-type substrate. Additionally, the epitaxial layer has a high-lifetime minority carrier property, which enabled long diffusion lengths in order to efficiently collect optically generated carriers via diffusion mechanisms. The wafer is divided in four quadrants, each represented by a reference die that received a different TID. The top right die is a reference die that received no X-ray irradiation. A photodiode test-chip is shown and it consists of four different photodiode structures, processed and fabricated in *ams OSRAM* mixed signal 180 nm technology. In the photodiode design, STI cut-lines are used in order to allow for correct processing due to active-area size restrictions in 180 nm technology. Furthermore, the layout consists of 242 NW islands that are surrounded by the highly-doped p-type surface implant, which was used for surface passivation. At the edge of the photodiode, a p/n/p-type guard-ring is implemented. Finally, below the STI, another SPI is introduced to partially passivate

STI/silicon interface. The bottom right quadrant did not have the SPI processed below the STI, due to non-standard processing.



## 4. X-ray experiments

The following chapter describes wafer-level X-ray irradiation procedure at Seibersdorf Laboratories. The wafer, on which the previously mentioned photodiode structures are fabricated, was securely prepared and transported to the irradiation facility where it was carefully aligned, irradiated and then stored in the cooling system to prevent defect annealing. Finally, the wafer was securely packaged and transported back to the optical laboratory at *ams OSRAM*, where electrical and optical measurements were performed.

### 4.1. Wafer-level X-ray irradiation

Wafer-level X-ray irradiation was performed at Seibersdorf Laboratories (Seibersdorf Labor GmbH), in Austria. The effective lifetime dose of a photodiode implemented in a CT scanner is specified to be 200 Gy(Si). The specification is related to a customer product and may be different for other CT scanner providers. Irradiation system used to irradiate the wafer is the X-ray equipment GE/Seifert ISOVOLT3003. It consists of the Machlett OEG-60 tube, 45° tungsten anode, 1.5 mm Beryllium permanent filtration and has an optical focus of 6 mm x 6 mm. The X-ray therapy quality, TW30 (BEV series CCEMRI 1972), of the previously mentioned X-ray system was chosen. The selected X-ray therapy quality corresponds to the following parameters: 30 kV tube voltage, average photon energy of 17 keV and first half-value thickness of 0.17 mm Aluminum. The irradiation energy of 17 keV was selected in order to have the maximum absorption of X-ray photons at the silicon oxide/silicon interface [103-105]. The irradiation measuring quantity was defined as kinetic energy released per unit mass (air KERMA), in Gy, in air without DUT. With assumed secondary electron equilibrium and negligible bremsstrahlung loss, justified up to the maximum photon energy of 150 keV, the air kerma can be equated with the absorbed dose in air. The surface of the wafer consists of a few  $\mu\text{m}$  thick inter-level dielectric (ILD) oxide, after which a thin silicon nitride layer is present. Between the nitride and the silicon, a very thin, up to 2 nm thick, native silicon oxide layer is located. Considering the thickness of the insulating layers and the energy of the incoming X-ray photons, the loss of the TID due to X-ray photons passing through different insulating layers is negligible and the TID can be considered as Gy in silicon [103, 104].

In such an irradiation setup, the photodiode electrodes were left floating during irradiation. Due to the spatial distribution of the X-ray beam, surrounding dies were also partially irradiated. Figure 4.1. shows the wafer map with highlighted three symmetrical irradiated dies, A1, A2 and A3, that were chosen for the X-ray irradiation experiment. The figure was based on [102], with added die names and the non-SPI quadrant for additional clarity. The notch is also visible



on the bottom part of the wafer, which indicates its orientation and helps with selecting the target dies for correct X-ray beam focusing. Dies A1, A2 and A3 were irradiated with TID of 100 Gy(Si), 200 Gy(Si) and 400 Gy(Si) respectively. Furthermore, the spread of the X-ray beam is indicated by the red-dashed circle. In addition to that, the non-irradiated reference die is highlighted by a red cross. The reference die is used in systematic error calculations in order to minimize the impact of external factors, such as the wafer misalignment and the manual position of the optical fiber on the measured characteristics. The systematic error calculation and its correction will be discussed in the chapter 5.2.3, where the measurement analysis of spectral responsivity after X-ray irradiation is explained in more details. For reference purposes, the wafer quadrant where the SPI was omitted is also highlighted in a transparent purple square. Irradiation dose rate was 100 Gy/h and the ambient temperature was  $T_{Xray} = 21$  °C. Each reference point was irradiated for a corresponding time to reach the desired TIDs. That is 1 hour for reference point A1 for a TID of 100 Gy(Si), 2 hours for reference point A2 for a TID of 200 Gy(Si) and 4 hours for reference point A3 for a TID of 400 Gy(Si).

Referent non-irradiated site for reference measurements

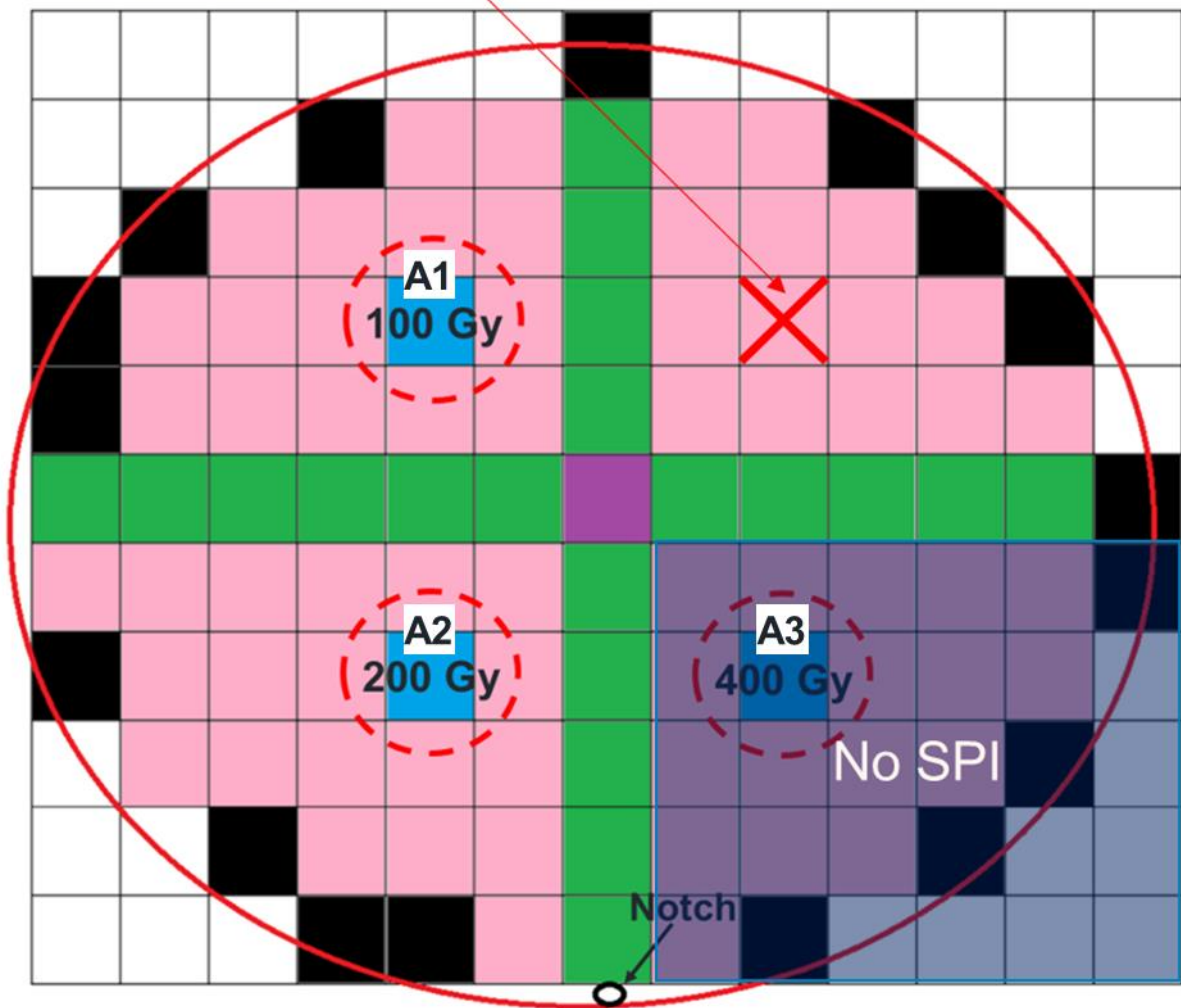


**Figure 4.1.** Irradiation wafer map. Blue-colored dies, the reference points (A1, A2 and A3) for irradiations, were irradiated with 100 Gy(Si), 200 Gy(Si) and 400 Gy(Si) respectively, with the dose rate of 100 Gy(Si)/h. Red-dashed circles approximate the X-ray beam distribution. Circle at the bottom of the wafer map represents the wafer notch, determining its orientation and helping with selecting the target reference dies for X-ray beam focusing. Purple-colored die is the middle die and the green-colored dies divide the wafer into 4 quadrants. Furthermore, pink-colored dies are additional dies, which have not received any X-ray irradiation, whereas the black-colored dies are not fully processed dies. The wafer quadrant where the SPI was omitted is highlighted in a transparent purple square. The figure was based on [102], with added reference die names and the non-SPI quadrant for additional clarity.

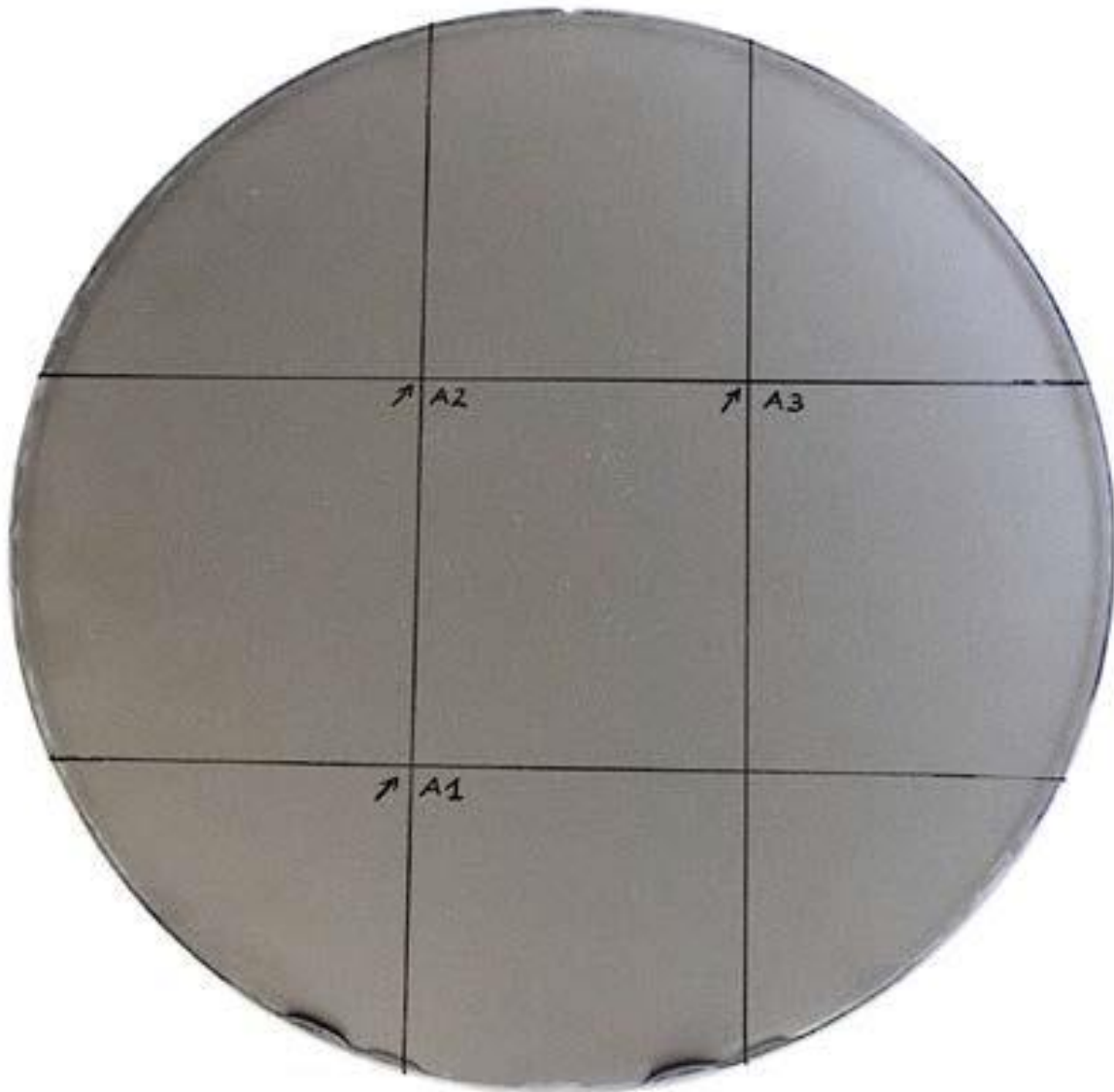


**Figure 4.2.** Marking of the reference points on the back-side of the wafer. Protective foil was attached on the backside of the wafer so that the reference marks can be gently added. Wafer notch is visible on the upper part of the wafer, indicating correct reference marking locations.

Before irradiation, the reference points were gently marked on the protective foil, which was placed on the backside of the wafer, as seen in Figure 4.2. Additionally, wafer notch is visible on the upper part of the wafer, indicating its orientation so that the reference markings can be correctly aligned. Afterwards, the wafer was fixed to a 2 mm polymethyl methacrylate (acrylic glass, plexiglass – PMMA) plate using adhesive tape, which can be observed in Figure 4.3.

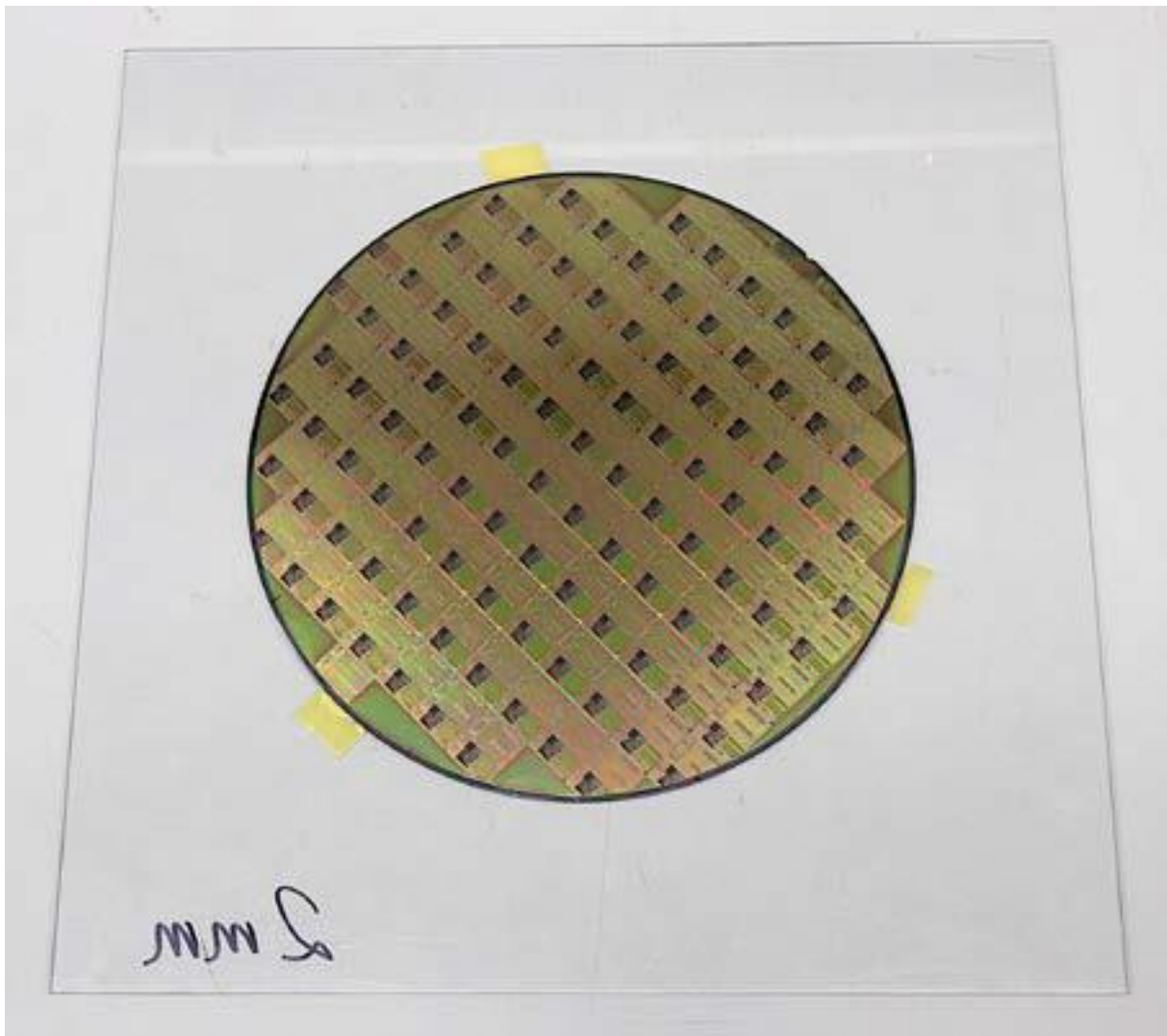


**Figure 4.3.** Fixed wafer to a 2 mm plexiglass plate with adhesive tape.

After the wafer was fixed to the PMMA plate, it was positioned in front of the collimator, the monitor chamber and the filter wheel of the X-ray system. The whole aperture can be observed in Figure 4.4. Furthermore, each reference point was positioned at a reference distance of 40 cm to the X-ray tube. An example of aligning the X-ray beam to backside of the A1 die is depicted in Figure 4.5. The wafer was then turned around so that the X-ray beam directly hits the front-side of the wafer.

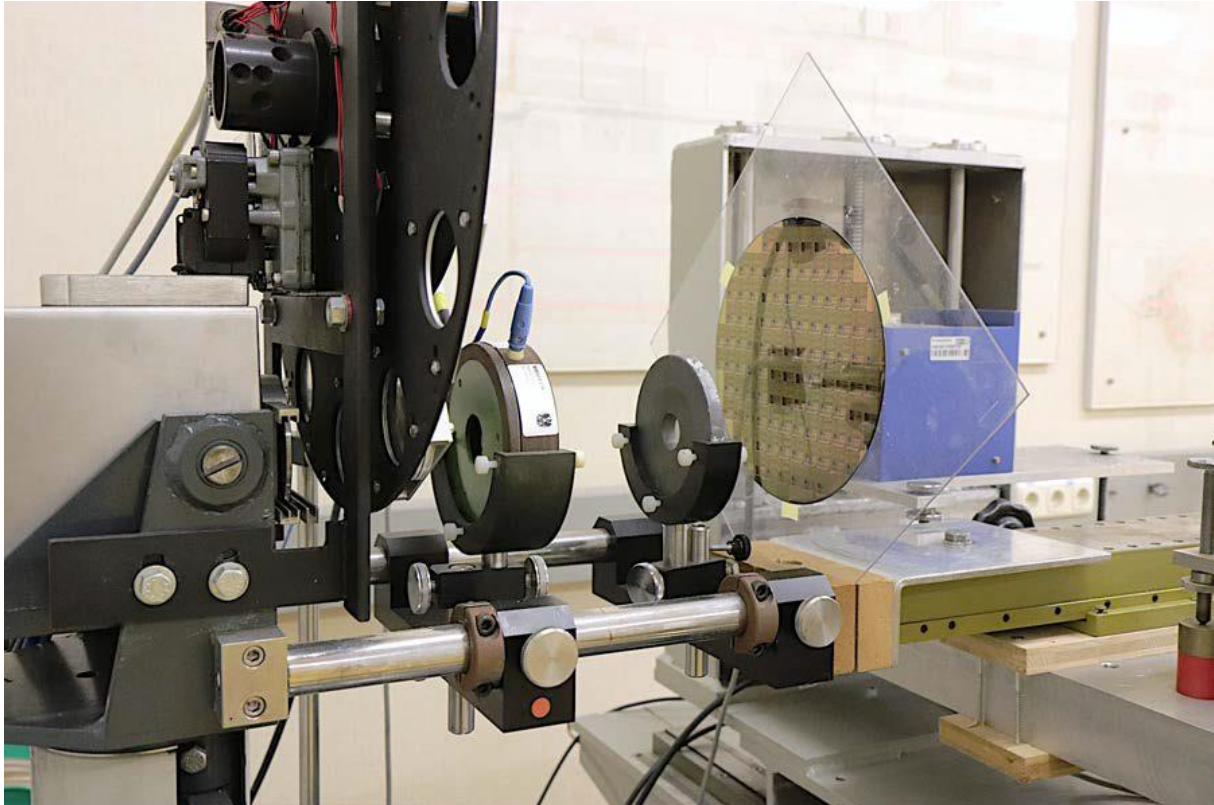


**Figure 4.4.** Positioning of the wafer in front of the collimator, the monitor chamber and the filter wheel of the X-ray system.

Since the wafer was unbiased during the X-ray irradiation, it added a small uncertainty in the experiment, thus by securely preparing the wafer before and after X-ray exposure, any influence on the post-irradiation measurements, due to wafer packaging and transport, is mitigated. The uncertainty, due to unbiased wafer conditions during X-ray irradiation is addressed in the chapter 7.5. In short, due to leaving the photodiode electrodes floating, and because of the charge build-up coming from X-ray irradiation, the electric field at the silicon oxide/silicon interface was slightly reduced, resulting in a smaller amount of TID induced defects. Nonetheless, the TCAD analysis, discussed in chapter 7.5. addresses the worst-case scenario for the given irradiation condition, showing that the change of the electric field had a negligible effect on the irradiation experiment.



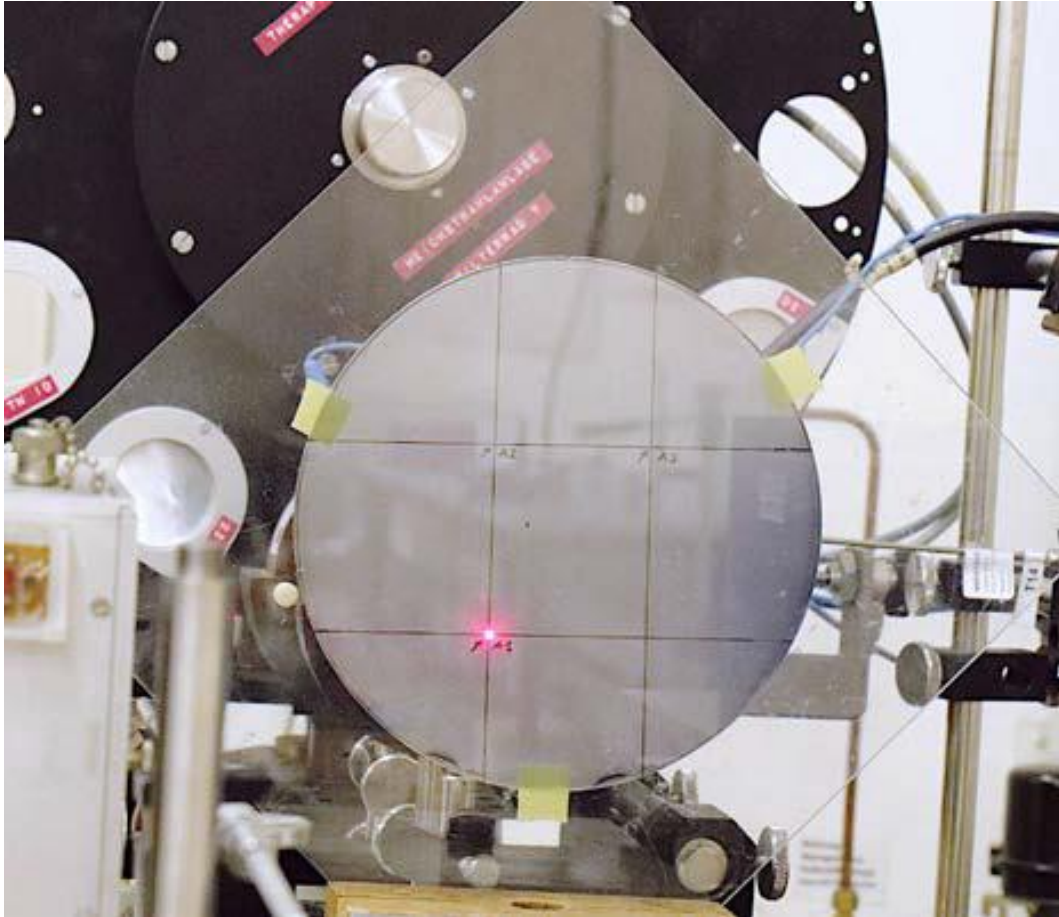


**Figure 4.5.** Alignment of the X-ray beam with the reference die A1 for X-ray exposure. After alignment, the wafer was turned around so that the X-ray beam hits the front-side of the wafer.

## 4.2. Wafer packaging

The following wafer packaging procedure is explained and discussed in order to show how carefully and securely the wafer was packaged and transported between the irradiation facility and the optical laboratory where the post-irradiation measurements were performed. Prior to irradiation, the wafer was securely placed in its wafer box, which can be seen in Figure 4.6. The contents of the box also include protective sponges and plastic layers in order to fixate and immobilize the wafer during its transport. After the X-ray irradiation concluded, wafers were securely placed in the same wafer box, which was placed inside an ESD vacuum sealer bag and evacuated, as seen in Figure 4.7. The wafer container was then placed in a cooler, where the evacuated sample was stored at low temperature,  $T = -22\text{ }^{\circ}\text{C}$ , in order to prevent any TID-induced defects from annealing. Afterwards, the wafers were transported in a cooler to the optical laboratory, where electrical and optical characterization was performed.





**Figure 4.7.** Wafer box was placed in an ESD vacuum sealer bag and evacuated so that it can be safely stored in a cooler at  $T = -22\text{ }^{\circ}\text{C}$ .

### 4.3. Summary

Wafer-level X-ray irradiation was performed at Seibersdorf laboratories, where three target dies on the wafer were irradiated with three different TIDs, 100 Gy(Si), 200 Gy(Si) and 400 Gy(Si), respectively, with the dose rate of 100 Gy/h. After the irradiation, the wafer was securely placed in the single-wafer box that was encased in the vacuum bag. The bag was evacuated and afterwards it was placed in the cooling system in order to avoid defect annealing. Finally, the wafer box was transported back to the optical laboratory, where electrical and optical measurements were performed.



## **5. Wafer-level measurements**

The following chapter gives a short introduction to wafer-level measurements. It describes how the wafer is handled at the probestation during electrical and optical measurements. Wafer-level measurements were performed at the semi-automated probestation in the optical laboratory. The probestation system enables accurate measurements since the wafers are sealed and isolated from external light. For additional protection against external light, a dark non-transparent cloth was placed over the probestation.

The wafer is placed on the thermal chuck of the probestation and is then aligned in order to allow for automated probing of the wafer. Thermal chuck allows for setting and controlling the temperature during each of the measurements. Pads of each photodiode structure were directly connected by the probes and various electrical and optical measurements were performed. During all measurements, the wafer is probed by probe-heads which are mounted on the micro-positioners that allow for careful contacting of the wafer. For optical measurements, a multi-mode optical fiber was mounted and positioned carefully above the examined photodiode structures. Furthermore, pre- and post-irradiation measurement methodologies are introduced, and the results are discussed. Finally, a comparison between pre- and post-irradiation measurements is given in order to determine the radiation-hardness of the analyzed photodiode structures.

### **5.1. Pre-irradiation characterization**

Pre-irradiation measurements were performed on the wafer, which was described in chapter 3, a few days before the same wafer was irradiated with X-rays of different TIDs. Since there were four comparison points in regard to the X-ray irradiation doses, four dies on the wafer were selected and measured before and after X-ray irradiation. Measurements after the X-ray exposure will be further discussed in chapter 5.2.

#### **5.1.1. Current-voltage characteristics**

During the current-voltage (I-V) measurements, bias was applied to the cathode pad, whereas the anode pad and the chuck were grounded. The operating temperature of a CT scanner ranges between 27 °C and 67 °C, with the standard operating conditions being around 50 °C. Therefore, the operating temperature was set to 50 °C, with the accuracy of +/- 0.5 °C. Voltage was swept between -1 V and +5 V in steps of 0.25 V, in order to measure both the forward-bias and the reverse-bias I-V characteristics. Main point of interest is the dark current

at the operating voltage  $V = 1.25$  V reverse bias and at  $50$  °C. Measurement inaccuracy was  $\pm 50$  fA during the measurements.

I-V curves of the structures depicted in Figure 3.4. are shown in Figure 5.1. The dark currents at the operating voltage and at the operating temperature, as well as the STI to photoactive area ratio for the four photodiodes are summarized in Table 5.1. Even though Device 4 has the smallest STI area distribution over the photoactive region, it shows the highest dark current compared to the other three devices. This implies that uneven separation of the islands by the STI cut-lines has a higher impact on the pre-irradiation dark current than the overall STI area of photoactive region, as long as the spacing between the closest islands and the STI cut-lines is constant. Additionally, the first three devices have roughly the same dark current at the operating voltage, around 2.7 pA, whereas the fourth device has 1 pA higher dark current due to variable spacing between the STI and the nearest NW island.

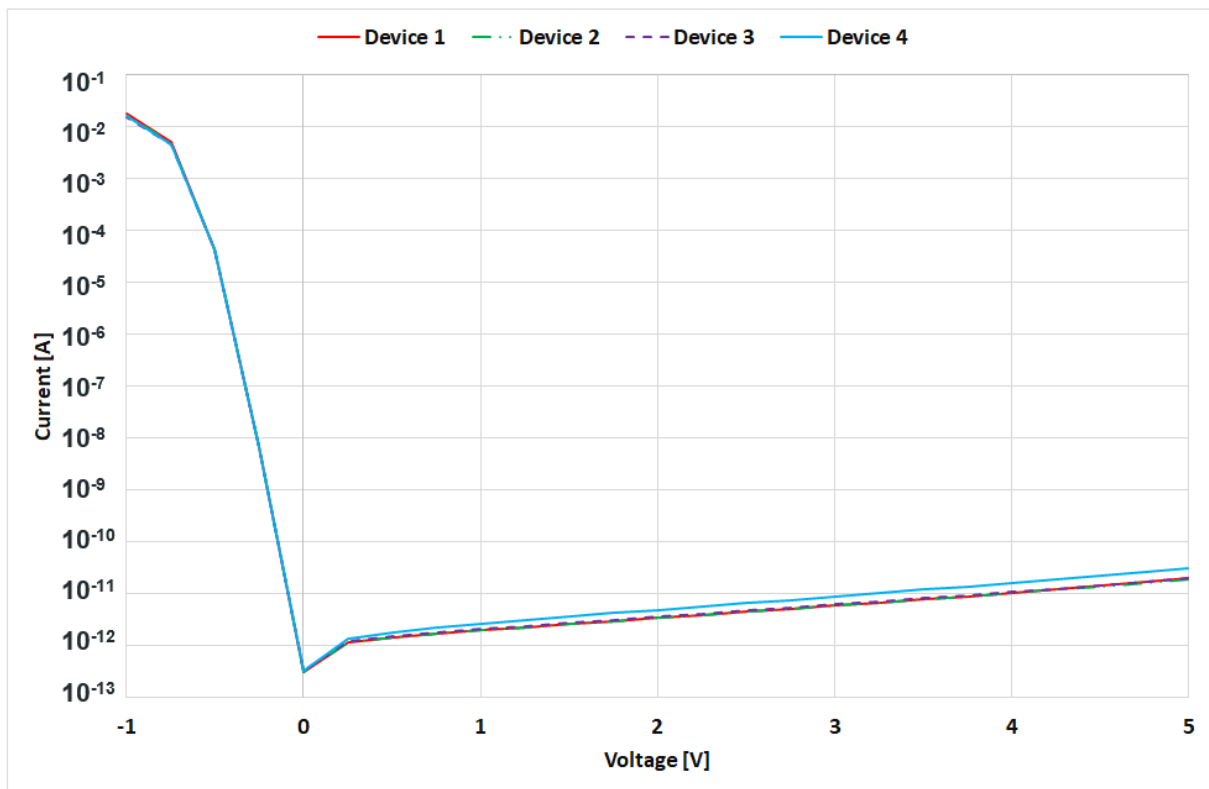


**Figure 5.1.** Current-Voltage (I-V) characteristics of the four structures depicted in Figure 3.4. Device 4 shows the highest dark current before X-ray irradiation due to uneven island separation by shallow trench isolation (STI) cut-lines.

**Table 5.1.** Pre-irradiation dark current at the operating conditions ( $T = 50$  °C,  $V_{Bias} = 1.25$  V) and shallow trench isolation (STI) to photoactive area (PA) ratio for the four photodiode versions.

Device #	I <sub>dark</sub> @ 50 °C, 1.25 V [pA]	STI/PA ratio [%]
Device 1	2.73	5.79

Device 2	2.63	4.61
Device 3	2.77	3.50
Device 4	3.66	3.18

### 5.1.2. Capacitance-voltage characteristics

In the case of capacitance-voltage (C-V) measurement, the cathode pad was grounded and a small AC signal was applied to the anode pad which was connected together with the chuck. The frequency of the AC signal was set to 100 kHz and the amplitude was set to 100 mV. Before the C-V measurements, an open-correction measurement, in which the probes were elevated and not connected on the wafer, was performed in order to mitigate the parasitic capacitance values coming from the cables, probe-heads and connectors.

Bias was applied to the Anode pad and was swept between 0 V and 5 V in reverse bias, with the step of 0.25 V. Since the SCR around the islands does not change significantly over the operating temperature range of the CT scanner, the measurements were performed at room temperature ( $T = 27\text{ }^{\circ}\text{C}$ ). Similar to the case of the I-V characteristics, four dies were measured in order to have a direct comparison with the post-irradiation measurements.

C-V characteristics of the photodiode structures shown in Figure 3.4. are depicted in Figure 5.2. and the capacitance values at the operating voltage,  $V = 1.25\text{ V}$  reverse bias, are shown in Table 5.2. There is no significant difference between the capacitance values of the four photodiode structures, since the main and dominating contributing factor to the capacitance is the number of NW islands, which is the same for all four structures. The small difference present in the measurement can be attributed to the measurement inaccuracy, which is in the range of  $\sim 40\text{ fF}$ .

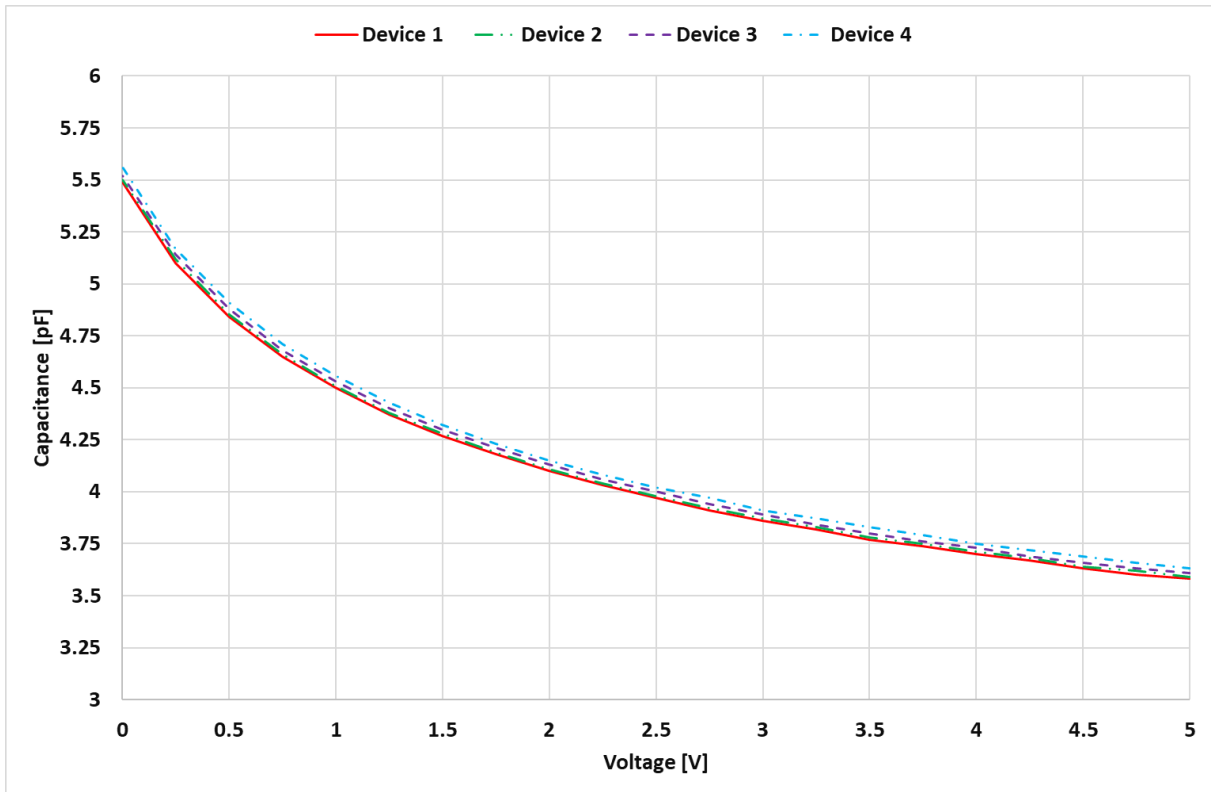


**Figure 5.2.** Capacitance-Voltage (C-V) characteristics of the four photodiode structures shown in Figure 3.4. All four photodiode structures show similar capacitance values, implying that the dominating factor that determines the total capacitance is the number of N-Well (NW) islands, which was the same for all four devices.

**Table 5.2.** Pre-irradiation capacitance at the operating conditions ( $T = 27\text{ }^{\circ}\text{C}$ ,  $V_{Bias} = 1.25\text{ V}$ ). Shallow trench isolation (STI) to photoactive area (PA) ratio is shown as a reference to each device. The difference between the photodiode structures is negligible and is in the range of measurement inaccuracy, which was in the range of  $\sim 40\text{ fF}$ .

Device #	Cap @ 27 °C, 1.25 V [pF]	STI/PA ratio [%]
Device 1	4.37	5.79
Device 2	4.38	4.61
Device 3	4.40	3.50
Device 4	4.43	3.18

### 5.1.3. Spectral responsivity characteristics

Optical measurements were performed by placing the multi-mode optical fiber above the photodiode structures on the wafer. The optical fiber, with the diameter of  $62.5\text{ }\mu\text{m}$ , was connected to the light source which uses a Xenon lamp in combination with the monochromator to generate light in spectral range between  $400\text{ nm}$  and  $900\text{ nm}$  with the step of  $5\text{ nm}$ . Before the fiber can be mounted, it must be prepared and assembled for the wafer-level measurements. The fiber preparation consists of stripping the plastic cover of the fiber and then cutting the tip

of the fiber such that the fiber-tip surface is flat. Finally, the fiber is heated by a small blowtorch and manually bent using the tweezers in order to get a  $\theta = 90^\circ$  angle between the fiber tip and the wafer surface.

Before the optical measurements, the optical power was calibrated by carefully positioning the optical fiber as close as possible to the surface of the external reference photodiode, which was connected to the power meter. The calibration is done over the relevant spectral range (400 nm – 900 nm) and is needed to overcome the inherent instability of the Xenon lamp and to get stable optical power at the output of the optical fiber. Even after the calibration, the optical power can vary up to 20 % between the two measurements done under the same conditions after the optical fiber was removed and reapplied to the measurement setup. Furthermore, the manual preparation and positioning of the fiber above the reference photodiode, can further contribute to the optical power variation. Because of that, similar variation of the photocurrent is expected. Still, the optical power, over the relevant spectral range, was in the order of 50 nW – 500 nW, for which the photodiode spectral responsivity (SR) was constant. On the other hand, during the consecutive measurements, the optical power remains constant, as long as the fiber is not removed from the light source.

During the SR measurements, bias was applied to the cathode pad and was set to 1.25 V in order to bring the photodiode in reverse bias operating condition. The anode pad, together with the chuck were grounded. The temperature was set to  $T = 27^\circ\text{C}$  during the measurements. Finally, four dies were selected and measured, similar to as in the I-V and C-V measurements. The fiber was carefully placed and elevated to such height that it illuminates a large portion of the photodiode structure, covering mainly the island region, but also partially the guard-ring region.

Furthermore, SR measurements are quite sensitive to fiber position above the photodiode structure, as illustrated in Figure 5.3. The optical fiber was placed above the center of the photodiode structure, which was located on the middle die of the wafer. Even though the wafer was automatically aligned on the chuck, there was a small misalignment, in the range of  $\sim 20\ \mu\text{m}$ , present over the wafer. Because of that, the optical fiber was slightly misaligned on the measured dies from the reference position. For larger photodiode structures, such as the ones analyzed in this experiment, the position of the fiber is less impacting and has negligible impact on the SR results. Additionally, since the fiber is manually prepared, there could be a small misalignment in the tilt of the fiber, resulting in a small variation ( $\delta$ ) of the angle between the fiber-tip and the wafer surface. Therefore, the final angle between the fiber-tip and the surface of the wafer can be approximated as  $\theta = 90^\circ \pm \delta$ . The added tilt of the fiber has

negligible impact since the photodiode structures were relatively large, compared to the fiber diameter. Finally, measurement repetition, due to wafer exchange, also adds a small variation in the fiber position. The change in fiber position relative to the photodiode layout can have a stronger impact on the SR measurements. The impact of said change in fiber position and the resulting systematic error, as well as its calculation will be addressed in chapter 5.2.3, where the post-irradiation spectral responsivity characteristics are analyzed.

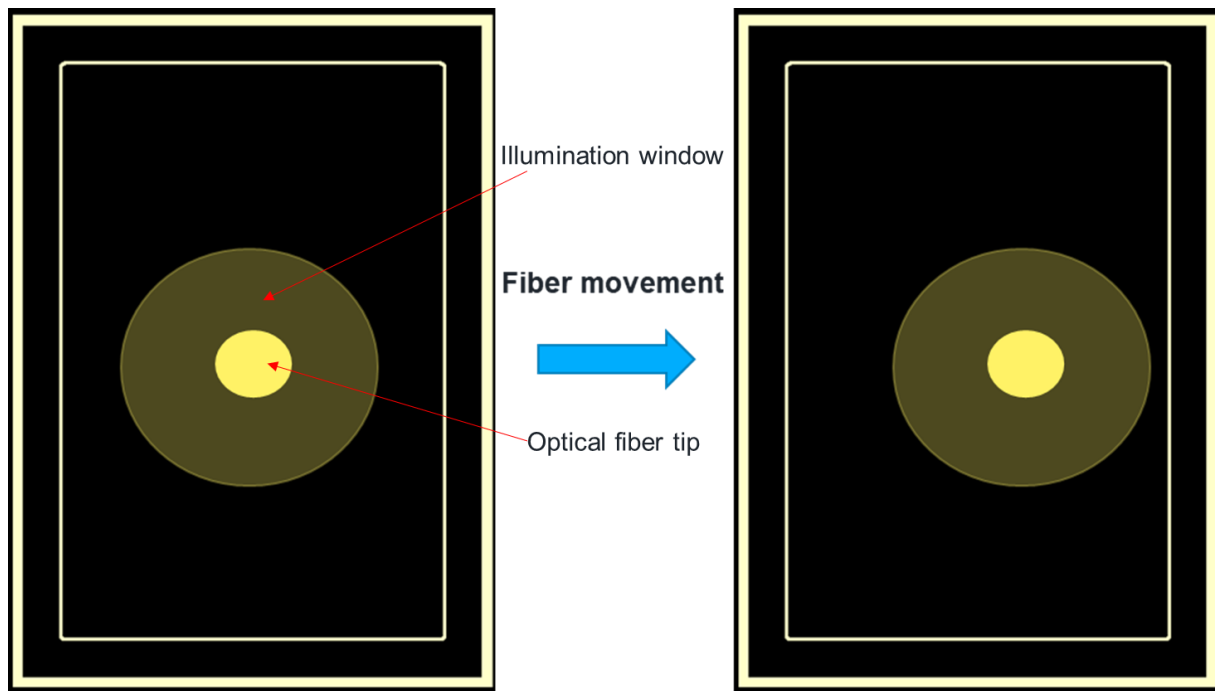


**Figure 5.3.** Illustrative impact of the fiber position on the large photodiode structure due to wafer misalignment ( $\sim 20 \mu\text{m}$ ) and manual fiber preparation. Highlighted areas include the optical fiber tip (small yellow circle) and the illumination window (transparent, large yellow circle). Due to wafer misalignment, small fiber misposition is expected. In the case of the analyzed photodiodes, the impact of the fiber misposition was minimal.

SR characteristics of photodiode structures, shown in Figure 3.4, are shown in Figure 5.4. Ripples in the SR curves exist because the light is propagating through multiple layers of thin dielectric films with different refractive indexes, before reaching the silicon surface. The thin dielectric films are a combination of different thicknesses of silicon oxide and silicon nitride layers. Target wavelengths are 510 nm, 670 nm and 780 nm. SR values for each photodiode structure at the target wavelengths, as well as the STI to photoactive area ratios are given in Table 5.3. It is expected that the STI had a small impact on lower wavelengths, compared to the case where there are no STI cut-lines present at all. Comparing the SR of the four analyzed photodiode structures, it can be concluded that small difference in the ratio of STI over the photoactive area had a negligible impact on optical performance before X-ray exposure and the difference was in the range of measurement inaccuracy.

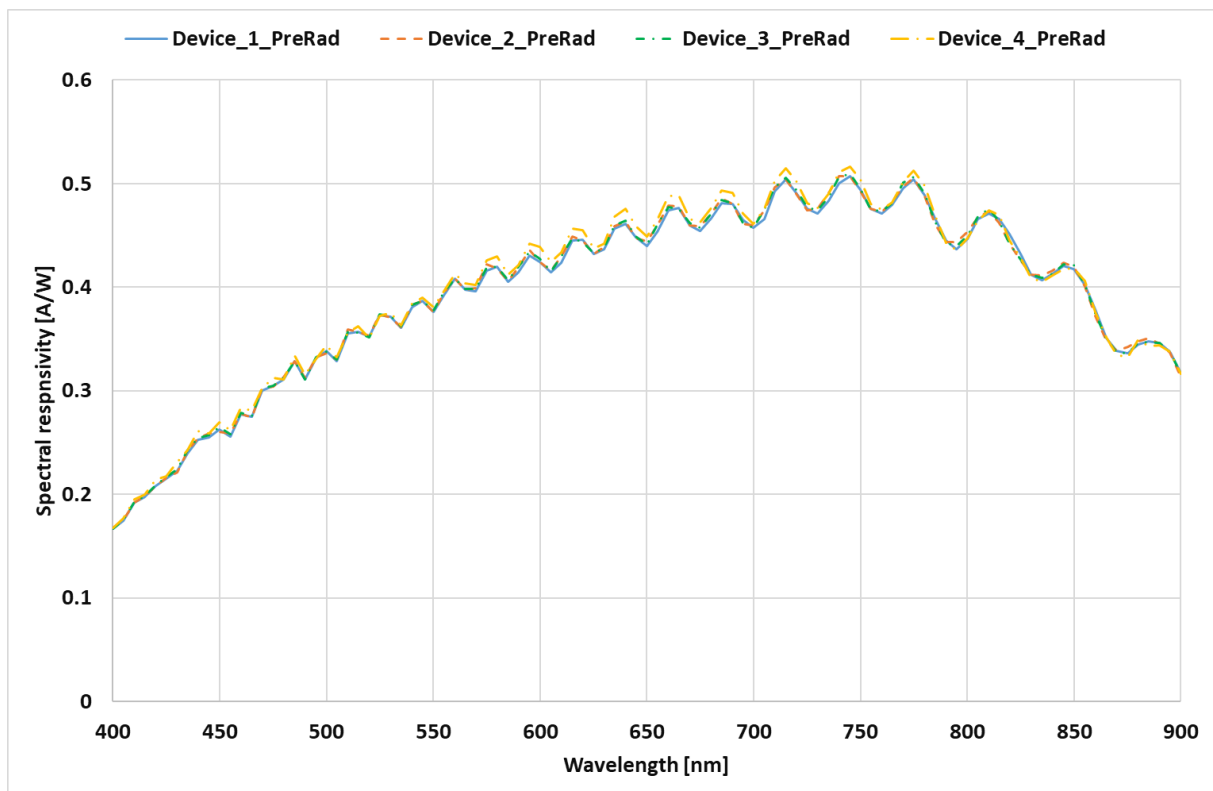


**Figure 5.4.** Spectral responsivity (SR) characteristics of the photodiode structures shown in Figure 3.4. Ripples observed in the characteristics are present because of the light propagation through thin silicon oxide and silicon nitride layers before reaching the silicon surface, resulting in an interference.

**Table 5.3.** Comparison between spectral responsivity (SR) values at target wavelengths for the four analyzed photodiode structures. Shallow trench isolation (STI) to photoactive area (PA) ratio is given as a reference to each photodiode. The difference between the four photodiodes is negligible and in the range of measurement inaccuracy.

Device #	SR [A/W] @ 510 nm	SR [A/W] @ 670 nm	SR [A/W] @ 780 nm	STI/PA ratio [%]
Device 1	0.3556	0.4600	0.4892	5.79
Device 2	0.3590	0.4595	0.4879	4.61
Device 3	0.3571	0.4616	0.4907	3.50
Device 4	0.3560	0.4661	0.4983	3.18

## 5.2. Post-irradiation characterization

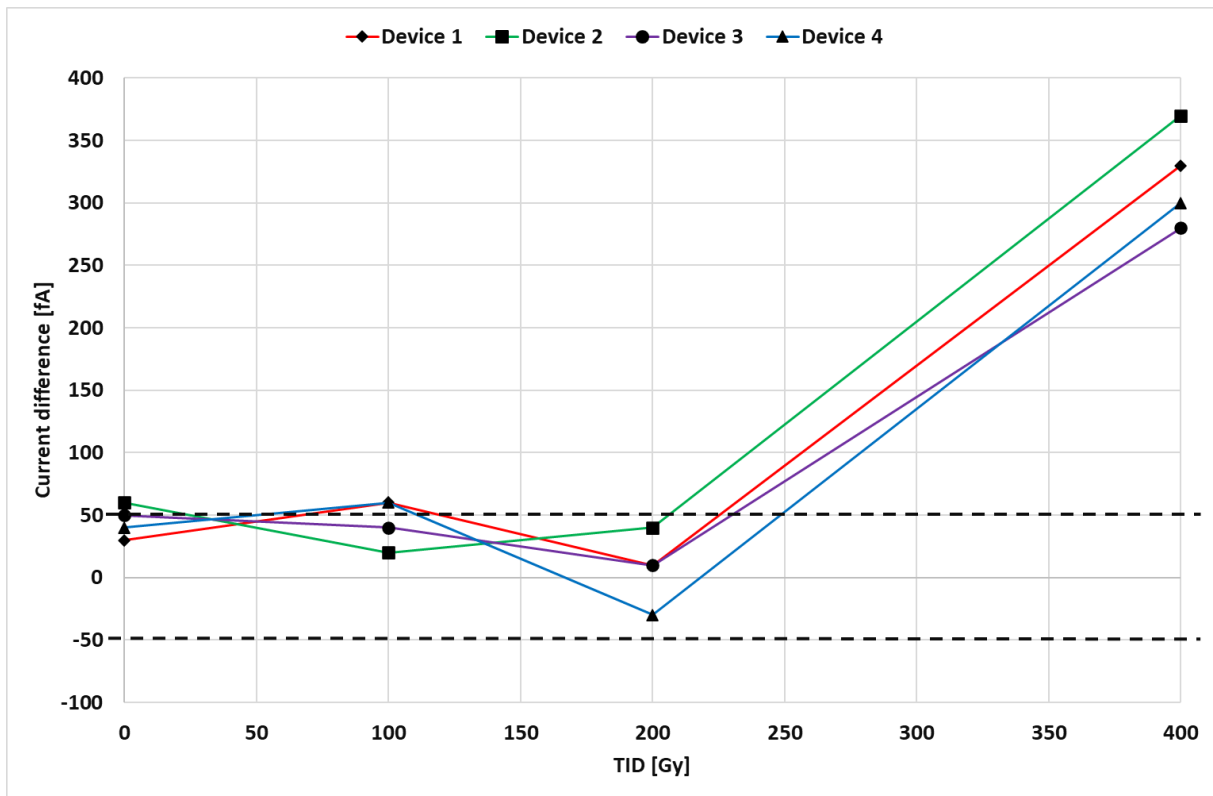
Once the wafers arrived back in the optical laboratory, the post-irradiation wafer-level electrical and optical measurements were performed, under the same conditions as the pre-irradiation measurements. In the following chapters, the main electrical and optical characteristics after X-ray irradiation are presented. Additionally, a comparison between

pre- and post-irradiation measurements is given in order to define radiation-hardness of the analyzed photodiode structures.

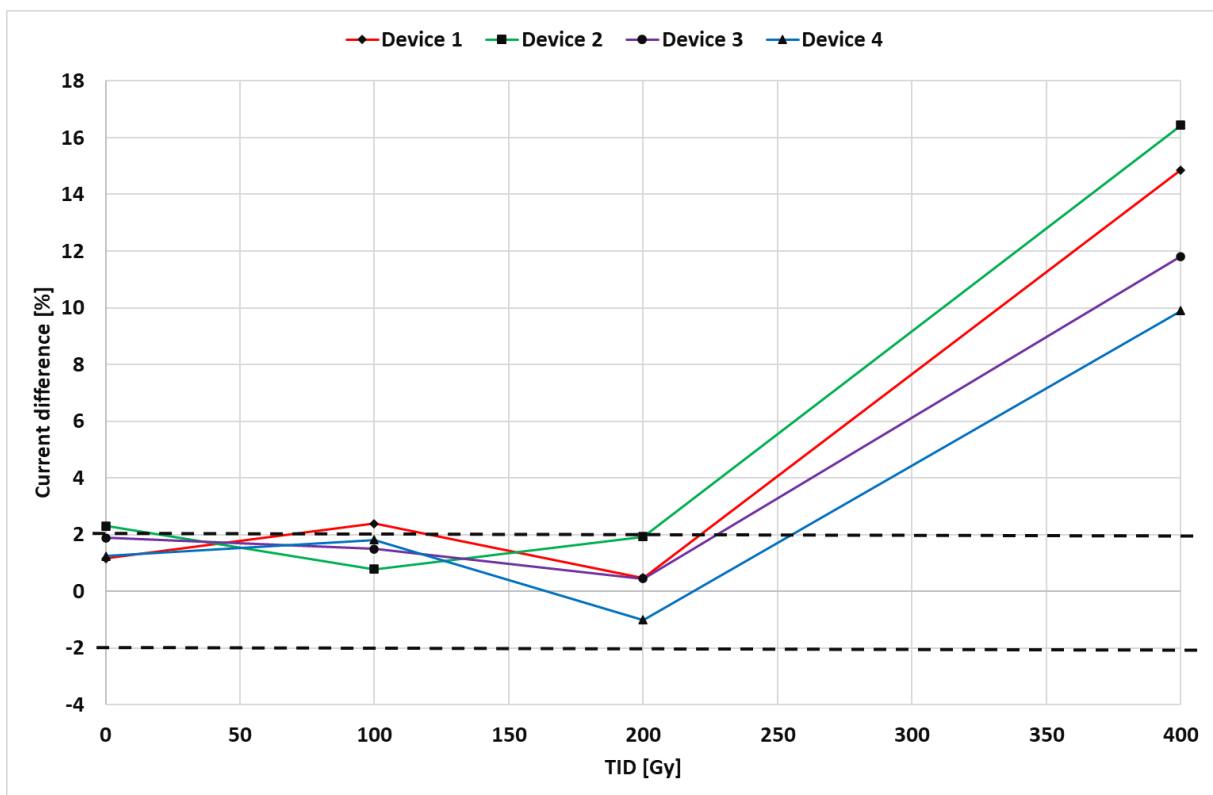
### 5.2.1. Current-voltage characteristics

Figure 5.5. shows dark current increase due to the increase of the TID, of the four photodiode structures. The measurement inaccuracy was  $\pm 50$  fA, corresponding to less than 2 % of the measured dark current. It is shown that the photodiodes are radiation-hard up to TID = 200 Gy(Si). At TID = 400 Gy(Si), all structures show an average increase of the dark current of  $\Delta I = 320$  fA. The increase is between 10 % and 16 % compared to the pre-irradiation values, which is shown in Figure 5.6. Additionally, the dark current difference between the non-irradiated and the irradiated case up to TID = 200 Gy(Si) is within the measurement inaccuracy of  $\sim 2$  %. Both conclusions are summarized in Table 5.4. The shown figure and the table are based on [102], with small additions, such as the TID value and STI/PA ratio column. Even though this could indicate that for smaller STI area, the dark current is higher, on the other hand, after irradiation it is shown that the dark current degradation is constant for all devices, meaning that initial dark current is not dependent on the STI area, but rather on the spacing between the nearest island and the STI. Devices 1 – 3 have constant spacing between the STI and the nearest island and show lower pre-irradiation dark current than Device 4, which has smaller STI area, but inconsistent spacing between the STI and the nearest island. Similar current increase after X-ray irradiation for all four photodiodes, indicates that the size of the unit cell does not impact the current degradation, but rather the un-passivated region, where the SCR reaches the silicon oxide/silicon interface. This is the most critical region where TID induced defects impact the electrical photodiode performance. The impact of the TID induced defects, as well as their modelling, will be discussed in chapter 7.





**Figure 5.5.** Absolute difference in dark current in fA, before and after X-ray irradiation, at each total ionizing dose (TID), for the four photodiodes shown in Figure 3.4. Dashed line represents the measurement inaccuracy, which was  $\pm 50$  fA. Photodiodes are radiation-hard up to TID = 200 Gy(Si), whereas an average increase of the dark current of  $\Delta I = 320$  fA for all four photodiodes can be observed after the TID = 400 Gy(Si) [102].



**Figure 5.6.** Dark current increase in [%] with increasing total ionizing dose (TID), up to 400 Gy(Si). The black dashed lines show the measurement inaccuracy, which was in the range of  $\sim 2$  %.

difference up to TID = 200 Gy(Si) is within the measurement inaccuracy, implying that the structures are radiation-hard up to that TID. After the TID = 400 Gy(Si), the current increase is between 10 % and 16 %.

**Table 5.4.** Post- and pre-irradiation dark current difference for the four photodiode structures at the operating conditions and at the TID = 400 Gy(Si) [102].

Device #	STI/PA ratio [%]	$\Delta I_{\text{dark @ 1.25 V, 400 Gy}}$ [fA]	$I_{\text{dark increase}}$ [%]
Device 1	5.79	330	14.86
Device 2	4.61	370	16.44
Device 3	3.50	280	11.81
Device 4	3.18	300	9.91

### 5.2.2. Capacitance-voltage characteristics

The capacitance of the analyzed photodiodes dominantly depends on the volume of the SCR, which is defined by the number of NW islands. Figure 5.7. shows capacitance change due to increasing TID. All capacitance values are within the measurement inaccuracy range of  $\sim 40$  fF, therefore the structures are radiation-hard in terms of capacitance up to TID = 400 Gy(Si). Table 5.5. summarizes the conclusions and gives a reference to the STI/PA ratio.

In the TCAD Sentaurus analysis, discussed in chapter 7, it is implied that SCR at the surface expands due to the irradiation-induced defects. Even though this heavily impacts the dark current, the capacitance at the operating voltage (1.25V reverse bias) remains unchanged. This is because the change in the total SCR volume is negligible to have a significant impact on the photodiode capacitance.

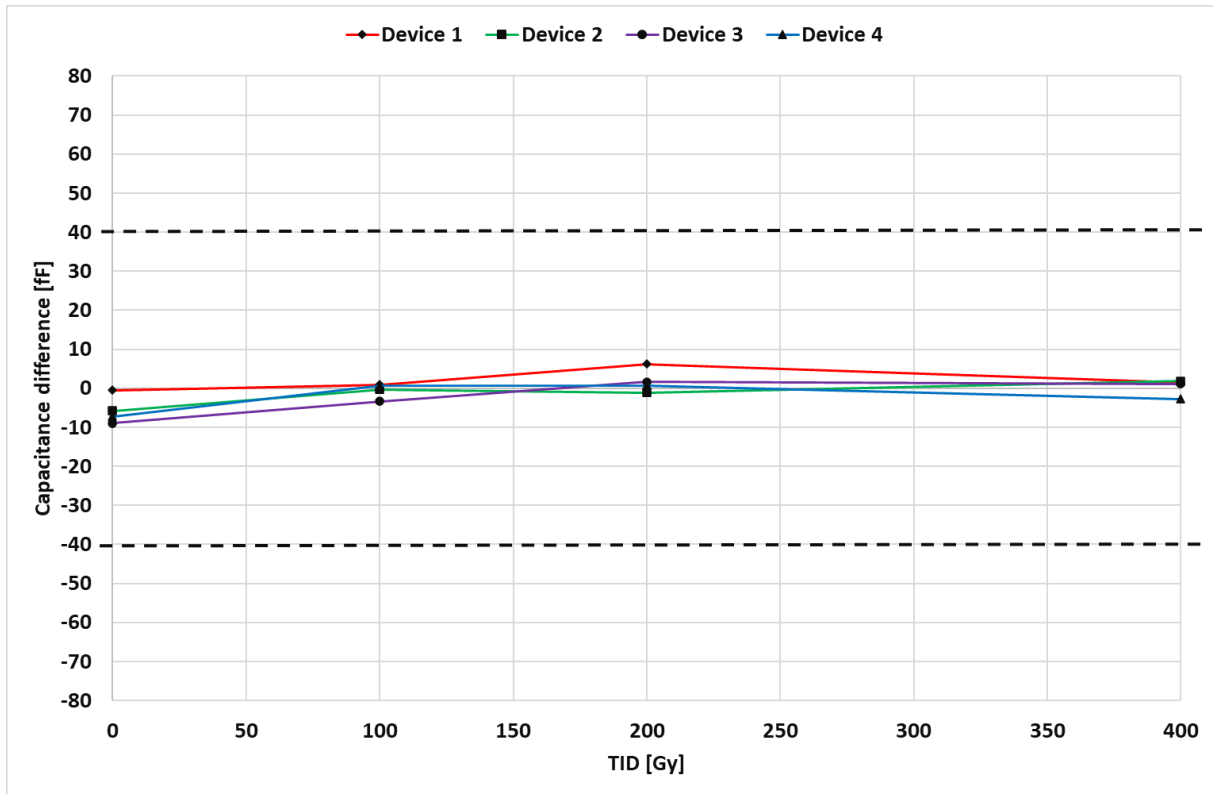


**Figure 5.7.** Photodiode capacitance vs total ionizing dose (TID) characteristics. Difference in capacitance due to increasing TID is within the measurement inaccuracy, indicated by black dashed lines, which is in the range of  $\sim 40$  fF. Even though the space charge region (SCR) at the surface expands after the TID induced defects are generated, the change in the total SCR volume is too small to have any impact on the photodiode capacitance.

**Table 5.5.** Post- and pre-irradiation capacitance difference for the four photodiode structures at the operating conditions. The change in capacitance is  $\ll 1\%$ , therefore the structures are radiation-hard up to TID = 400 Gy(Si).

Device #	STI/PA ratio [%]	$\Delta\text{Cap @ 1.25 V, 400 Gy [fF]}$	Cap increase [%]
Device 1	5.79	1.39	$\ll 1\%$
Device 2	4.61	1.86	$\ll 1\%$
Device 3	3.50	1.12	$\ll 1\%$
Device 4	3.18	-2.76	$\ll 1\%$

### 5.2.3. Spectral responsivity characteristics

Optical performance of the photodiode structures strongly depends on the peripheral area of the photodiodes, e.g. the spacing between the NW islands, because the collection of optically generated carriers is dominated by diffusion mechanism. Because of that the impact of the STI, its passivation and the proximity to the closest NW island, heavily affects the SR characteristics, especially after X-ray irradiation.

As mentioned before, in the pre-irradiation SR characteristics, the position of the optical fiber can shift between the measurements as well as during the same measurement. The latter situation, where due to a small wafer misalignment the fiber position shifts, has a negligible effect on the spectral responsivity measurements. On the other hand, since the fiber was manually placed above the wafer surface, the misposition of the fiber can have a major effect on the measured optical performance of the photodiode structures.

In order to understand the impact of the optical fiber misposition error, due to manual fiber placement between the measurements, SR measurements were carried out on the reference die, marked by the red cross in Figure 4.1. As an example, a comparison between SR measurements before and after irradiation of the first photodiode structure is shown in Figure 5.8. In the name of the curves, it was indicated which measurement was done before and which measurement was done after the wafer was exposed to X-rays, even though the reference die did not receive any TID. It is clearly indicated that there is a change in the SR characteristics, especially in the longer wavelength range (750 – 900 nm) due to the optical fiber misposition. The purpose of that analysis is to calculate the systematic error,  $Q_{SR}$ , which is a normalization factor used to mitigate the added influence of the fiber misposition between the measurements on the SR characteristics. The systematic error was calculated for each of the four analyzed photodiode structures on the reference die according to:

$$Q_{SR} = \frac{SR_B}{SR_A}, \quad (2)$$

where  $SR_B$  [A/W] and  $SR_A$  [A/W] are the spectral responsivity, at each measured wavelength, before and after X-ray irradiation respectively. Afterwards, the normalization was applied to the SR values on the dies that received X-ray irradiation:

$$SR'_A = SR_A \cdot Q_{SR}, \quad (3)$$

where  $SR'_A$  [A/W] is the adjusted SR characteristics after normalizing the measured values by applying the systematic error.

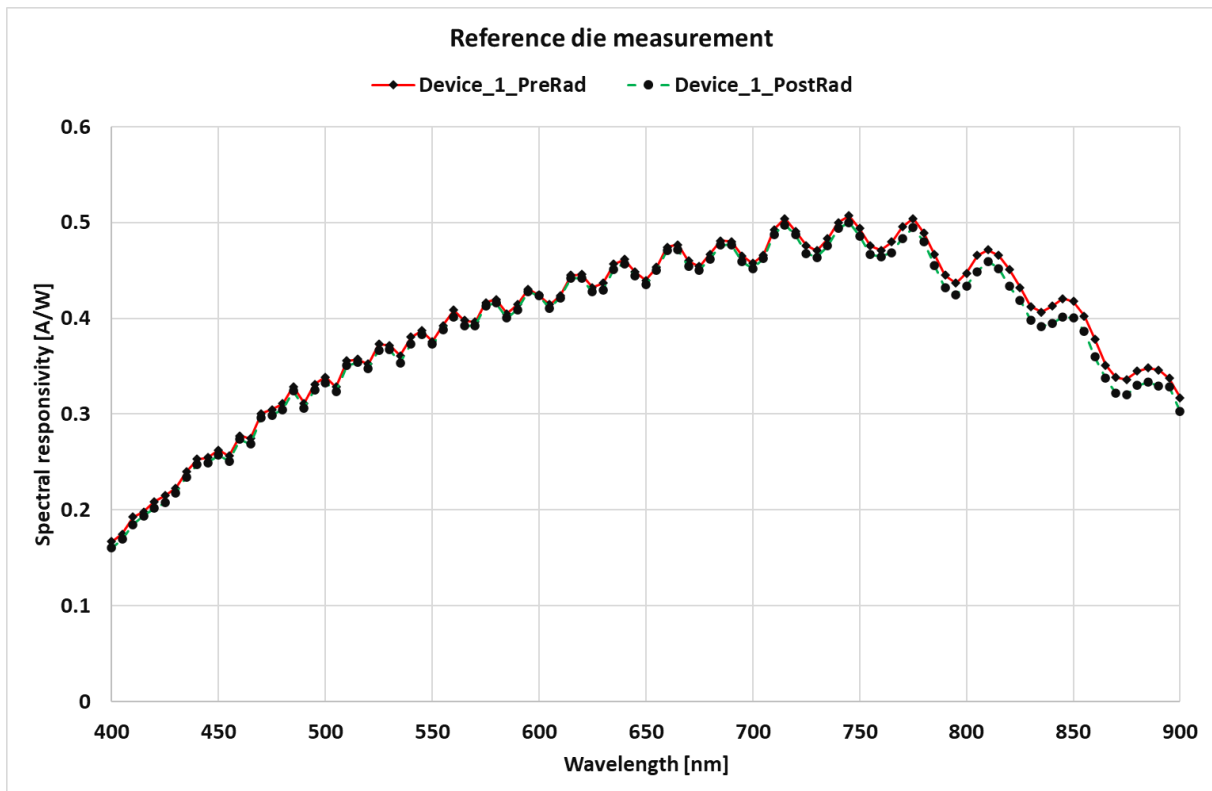


**Figure 5.8.** Comparison of the spectral responsivity (SR) measurement, on the reference die, of the first photodiode device before and after X-ray irradiation. Due to optical fiber misposition, there is a clear mismatch between the two characteristics, especially in the longer wavelength range (750 – 900 nm). Even though the reference die did not receive any total ionizing dose (TID), for consistency reasons, the curves were named such that it can be clearly indicated which measurement was done before X-ray and which measurement was done after X-ray irradiation.

The adjusted SR characteristics of the first structure (Device 1) on the reference die, after applying the normalization factor, is shown in Figure 5.9. After the adjustment, the mismatch in the SR characteristics due to the optical fiber offset was completely removed. The systematic error is expressed in [%] and it goes up to 4 % at lower wavelengths (< 450 nm) and up to 5.2 % at higher wavelengths (> 750 nm), as seen in Figure 5.10.

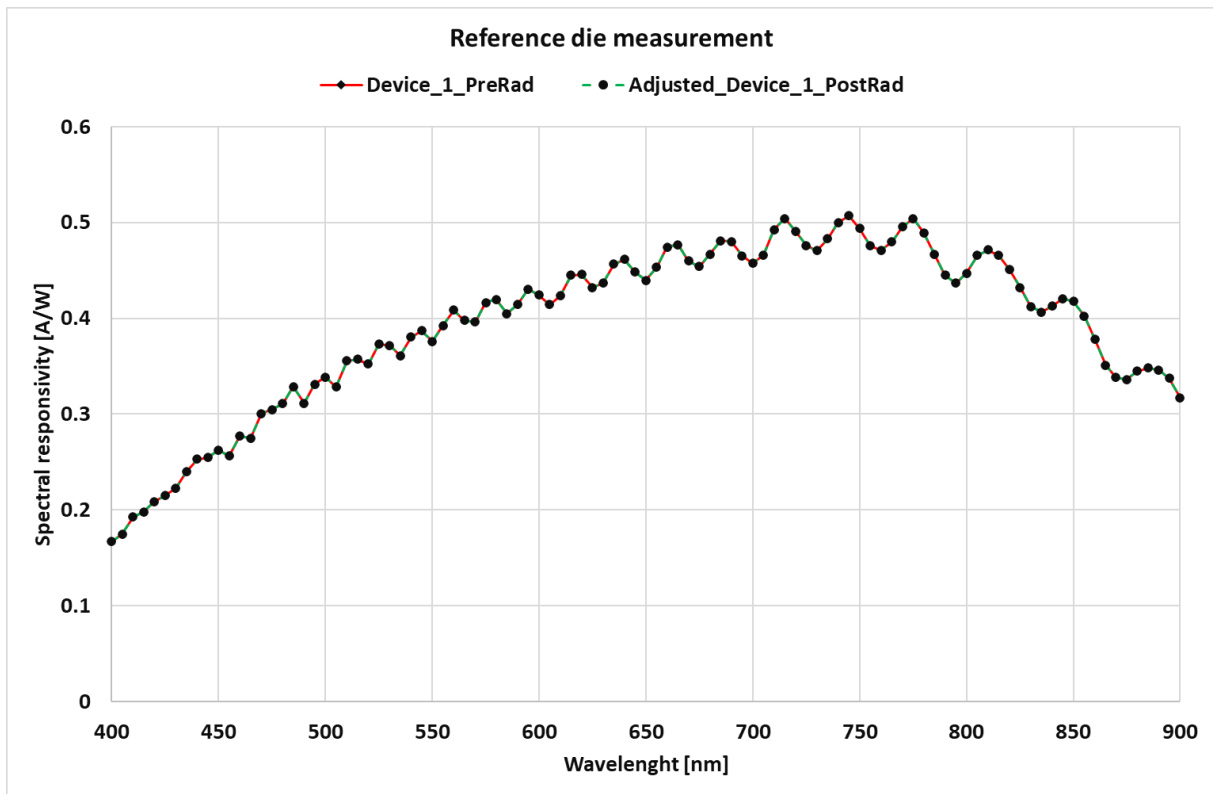


**Figure 5.9.** Adjusted spectral responsivity (SR) characteristics of the Device 1 after applying the normalization factor. After the adjustment, the mismatch in the SR characteristics due to the optical fiber offset was completely removed.

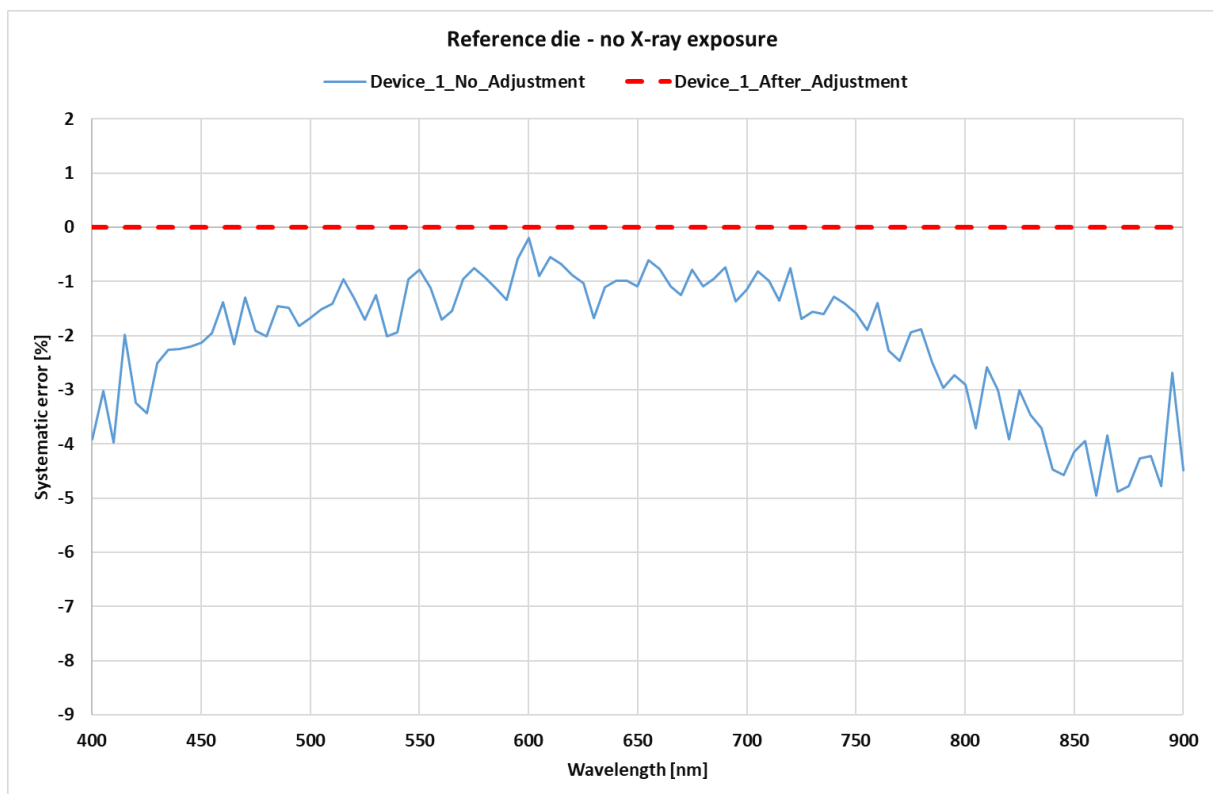


**Figure 5.10.** Systematic error adjustment for Device 1 at the reference (non-irradiated) die. The systematic error was in the range of 4 – 5 % and after the spectral responsivity (SR) adjustment, the error dropped to 0%, implying that the SR measurement inaccuracy, due to optical fiber offset, was mitigated.

The systematic error normalization was performed on all four structures (devices 1 – 4) and was applied to the spectral responsivity data on the remaining three sites, which were irradiated by different TID, as indicated in Figure 4.1. The systematic error before and after normalization of the SR measurement of Device 1 for each TID is depicted in Figures 5.11. a) – c). Negative values indicate the reduction of the SR characteristics after X-ray exposure. After the adjustment, there are still spikes present in the systematic error, because of the ripples in the SR characteristics. Therefore, the average of the adjusted systematic error is highlighted by the red dashed line, indicating the flat degradation of the SR characteristics due to the increasing TID dose. In the case of TID = 100 Gy(Si), there is no degradation. Furthermore, after the exposure with TID = 200 Gy(Si), the degradation was quite small and in the range of  $\sim 0.79\%$ . Considering that the reduction of the SR was  $< 1\%$  after TID = 200 Gy(Si), it can be concluded that the photodiode structure is radiation-hard for the given TID. Finally, after the TID = 400 Gy(Si), the average degradation of the SR of the first photodiode structure is in the range of  $\sim 2.29\%$ . The jump in degradation between the two TIDs can be attributed to the non-passivated STI/Silicon interface in the case of the larger TID. The reason for a flat degradation over the whole spectrum range is the high-lifetime property of the epitaxial layer. Because of that, the optically generated minority carriers can diffuse long distance. Most of them are collected by the NW islands, but some of them may get trapped at the STI/Silicon interface, where the trap centers are located. Additionally, if the interface is not passivated, which is the case of the die that received the highest TID, more interface traps will be generated, thus the optically generated minority carriers will have a higher probability to be trapped at the non-passivated interface, compared to the passivated one, resulting in a reduced SR.

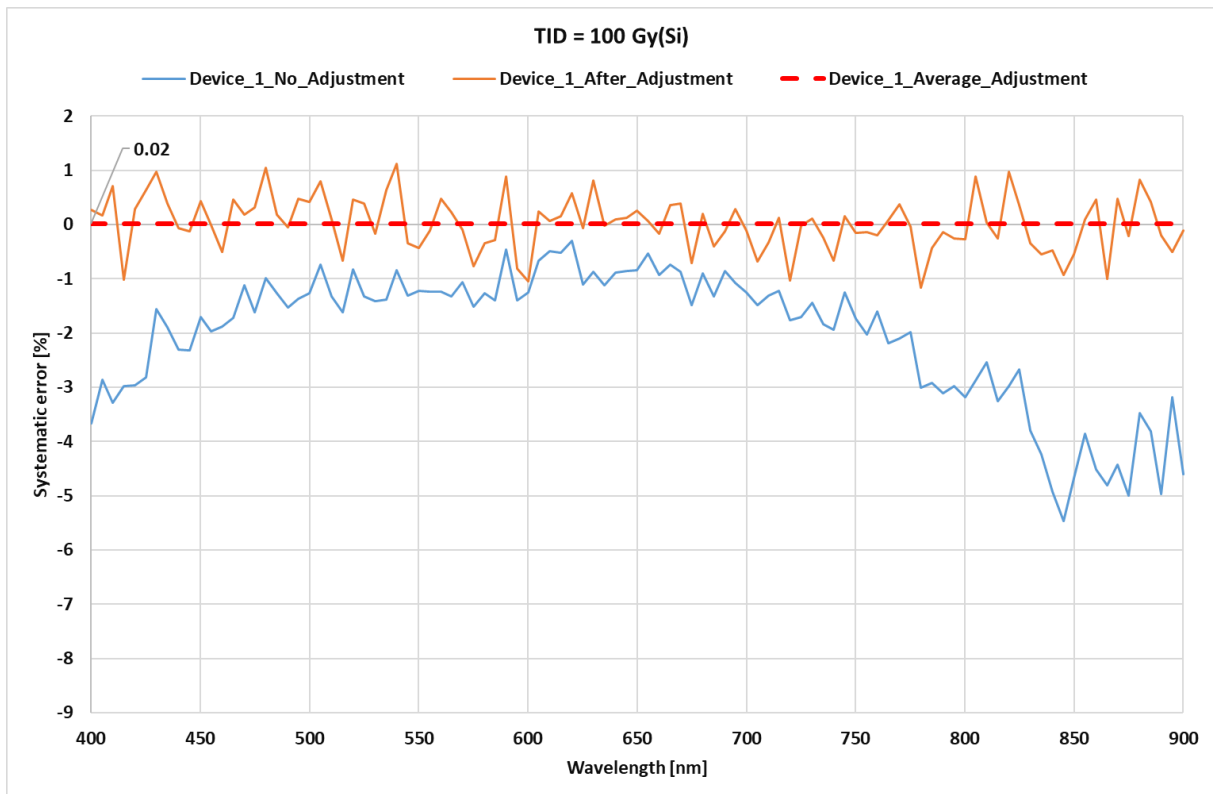


**Figure 5.11. a)** Systematic error adjustment for Device 1 at die A1, that received TID = 100 Gy(Si). After the adjustment, there are still spikes present in the systematic error, because of the ripples in the spectral responsivity (SR) characteristics. After the TID = 100 Gy(Si), there is no significant degradation observed in the SR characteristics of the first photodiode structure.

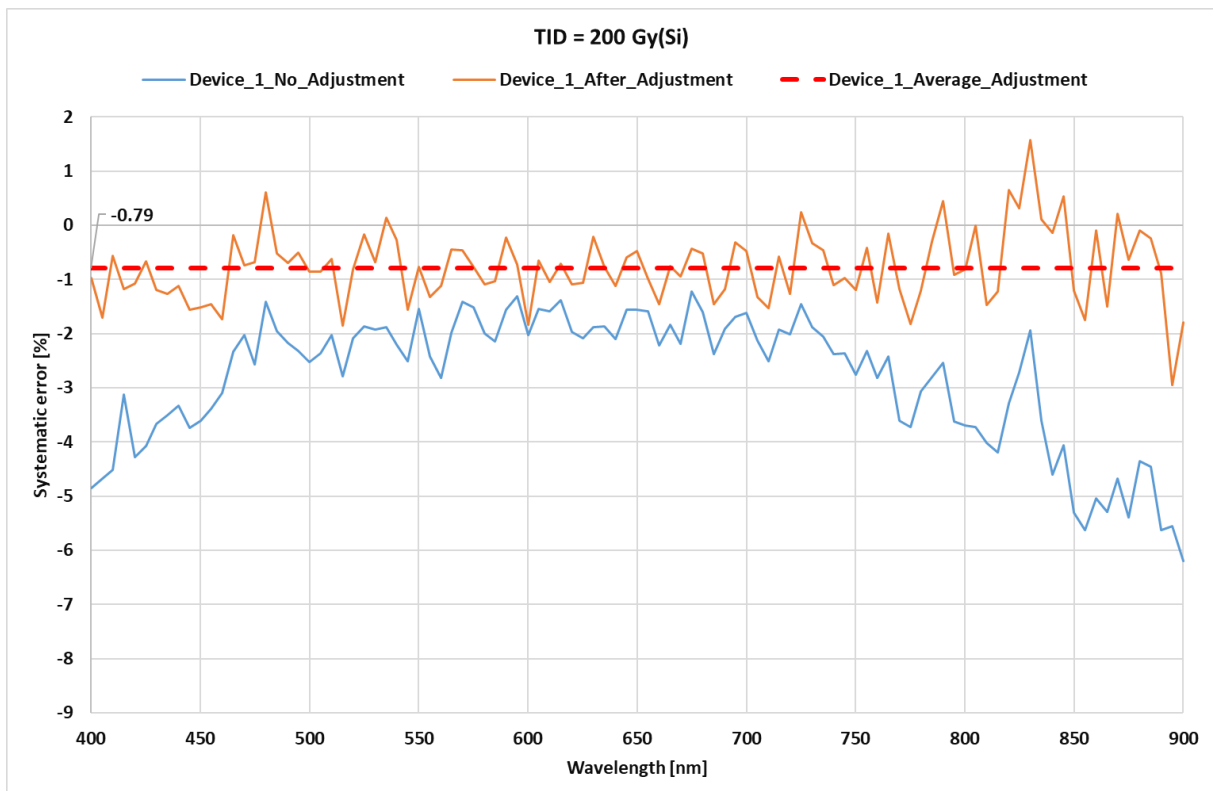


**Figure 5.11. b)** Systematic error adjustment for the Device 1 at die A2, that received TID = 200 Gy(Si). The degradation of spectral responsivity (SR) characteristics of the first photodiode was in the range



~ 0.79 %. Even though there is a small degradation in the optical performance, the reduction of the SR is < 1% and the photodiode can be considered to be radiation-hard up to 200 Gy(Si).

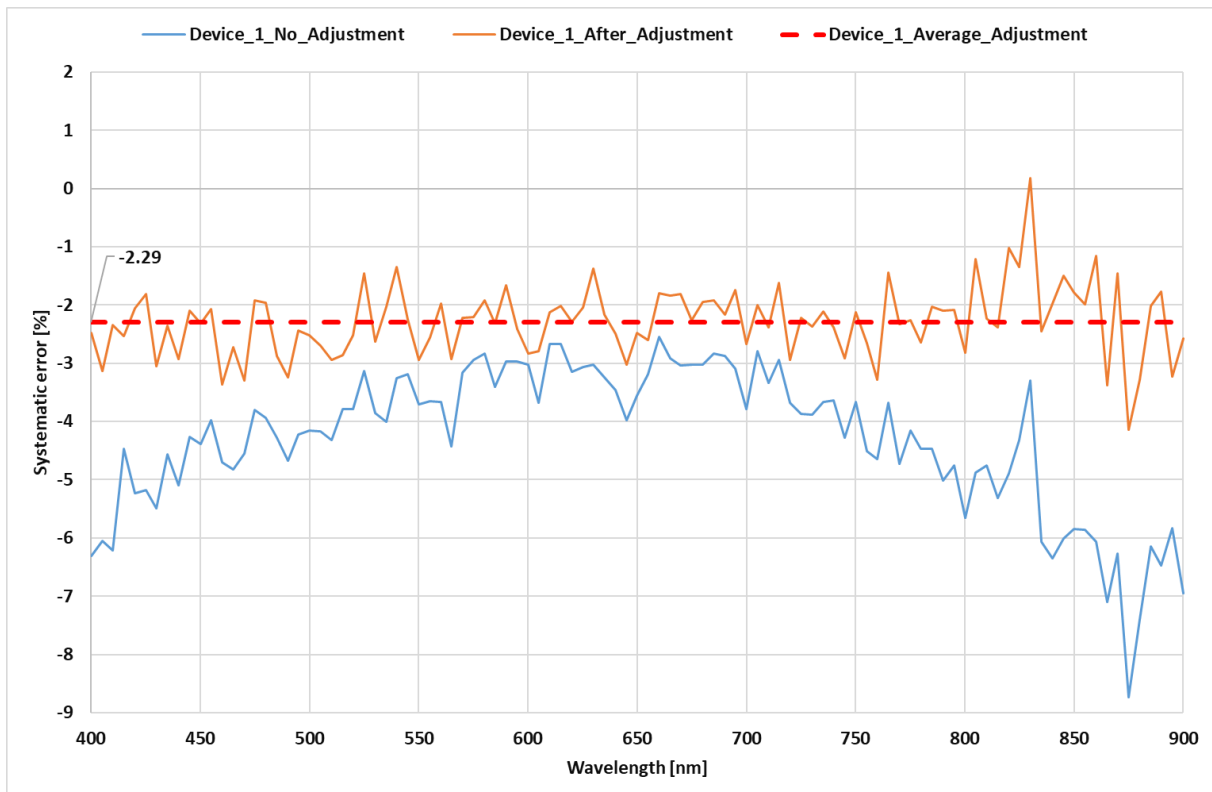


**Figure 5.11. c)** Systematic error adjustment for Device 1 at die A3, that received TID = 400 Gy(Si). The degradation of spectral responsivity (SR) is in the range of ~ 2.29 %. Even though the degradation of the SR was not significant, it could be further improved by including the shallow p-type implant (SPI) below the shallow trench isolation/silicon (STI/Si) interface in order to better passivate the interface.

Overall, the degradation after the X-ray irradiation is not significant, implying that SPI present in the first three quadrants of the wafer passivated the STI/Silicon interface well. Additionally, considering the fact that the fourth quadrant, where the die was irradiated with the highest TID = 400 Gy(Si), did not have the SPI present, it can be concluded that the electric field present at the STI/Silicon interface was relatively low. If the electric field is small, the fraction of unrecombined holes will also be small, resulting in an even lesser amount of interface traps. The influence of the SPI, as well as the electric field distribution and the doping profile comparison of the two cases, with and without the SPI, will be discussed in chapter 7.6.

Comparison of the SR characteristics of the four analyzed photodiode structures after TID = 400 Gy(Si) is shown in Figure 5.12. The curves were adjusted with the systematic error value that was calculated according to (2) and (3). Device 4, the photodiode structure with the smallest STI /PA ratio shows the lowest SR degradation, compared to Device 1, which had the largest STI/PA ratio. Figure 5.13. shows the degradation of the SR of the four analyzed photodiode structures with the increasing TID. The industry specification for the CT-scanner

sensor effective lifetime dose is  $TID = 200 \text{ Gy(Si)}$  and since the SR degradation at that TID is  $< 1 \%$ , the devices are considered to be radiation-hard. Clear indication of SR degradation starts to be visible after the  $TID = 400 \text{ Gy(Si)}$ . Even at  $TID = 400 \text{ Gy(Si)}$ , the reduction of the SR is only in the range of  $\sim 2.29 \%$ , which for industry standards is quite robust. Another perspective to consider is the STI/PA ratio in regard to the TID. Figure 5.14. shows the degradation of the SR characteristics with the increasing STI/PA ratio for the given TIDs. Larger STI area results in more degradation of the SR curve. The conclusions for all four photodiode structures are summarized in Table 5.6., where the differences in the SR at target wavelengths, 510 nm, 670 nm and 780 nm respectively, as well as the overall degradation in [%] is shown.

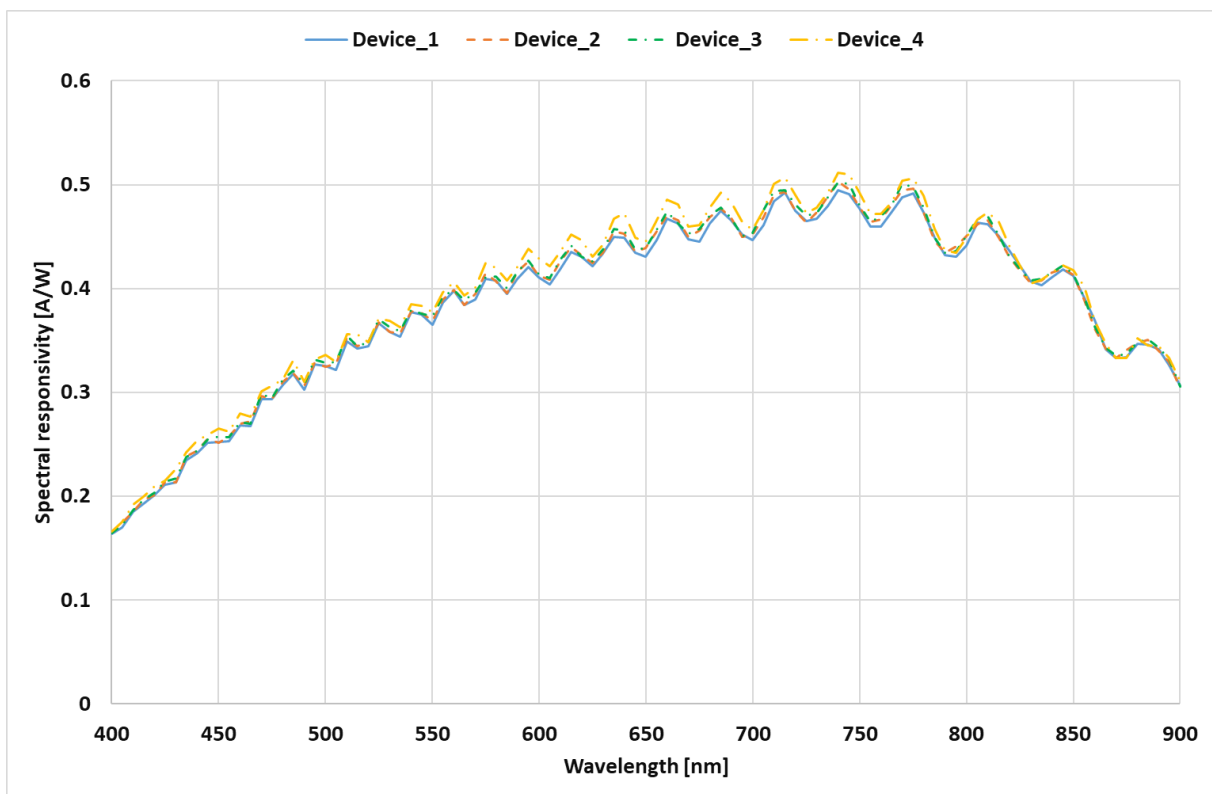


**Figure 5.12.** Spectral responsivity (SR) characteristics of the four analyzed photodiodes after the  $TID = 400 \text{ Gy(Si)}$ . The curves were adjusted with the systematic error value. Device 4, the photodiode structure with the smallest shallow trench isolation (STI) over the photoactive area (PA) ratio shows the lowest degradation, compared to Device 1, which had the largest STI/PA ratio and therefore the biggest degradation.

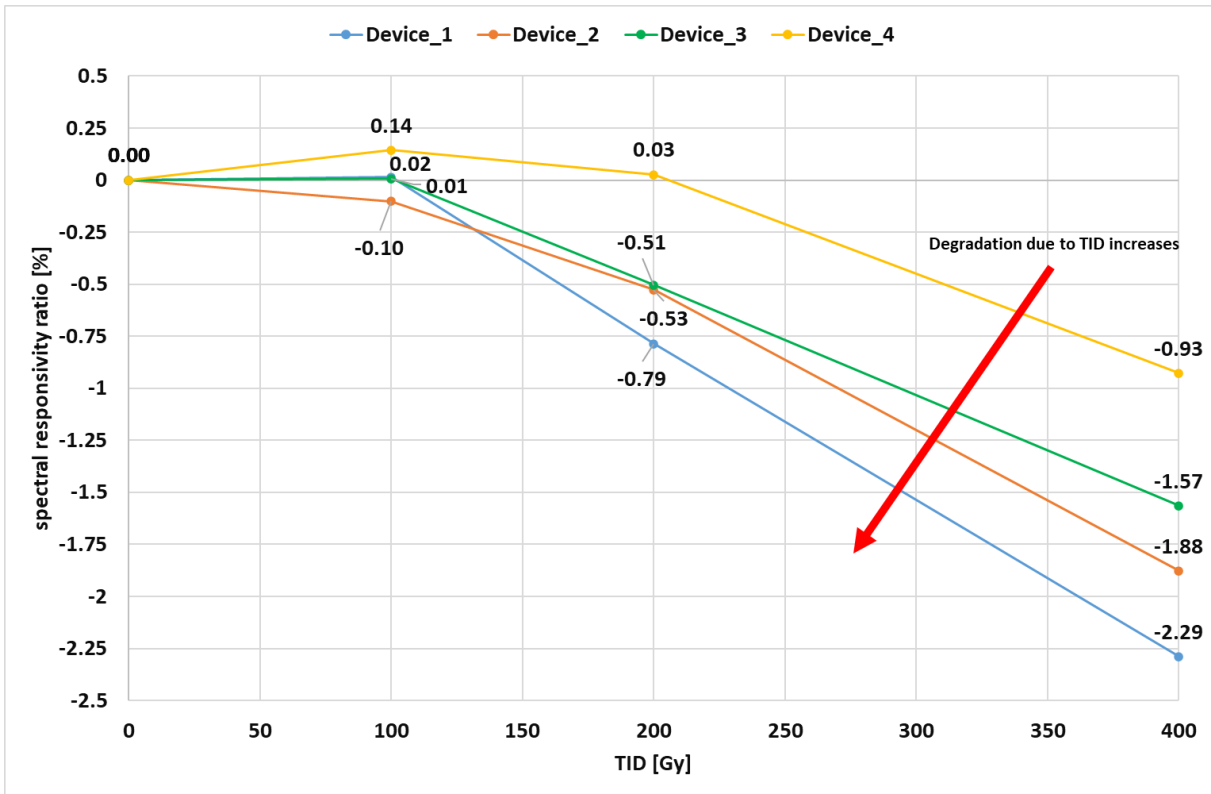


**Figure 5.13.** Degradation of spectral responsivity (SR) of the four analyzed photodiodes with increasing total ionizing dose (TID). The industry specification for the CT-scanner sensor effective lifetime dose is TID = 200 Gy(Si) and since the degradation at that TID is < 1 %, the devices are considered to be radiation-hard. Clear indication of degradation starts to be visible after the TID = 400 Gy(Si). Even at TID = 400 Gy(Si), the reduction of the SR is only in the range of ~ 2.29 %, which for industry standards is quite robust.

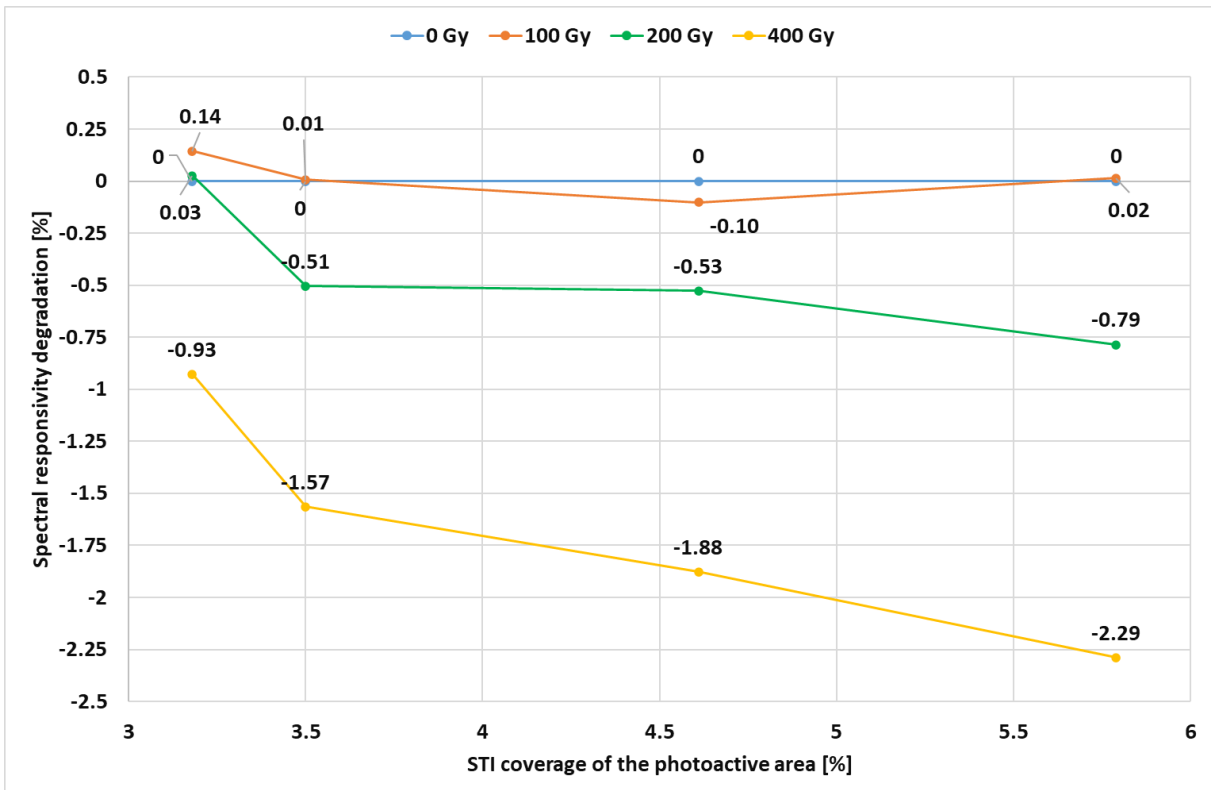


**Figure 5.14.** Degradation of the spectral responsivity (SR) characteristics with the increasing shallow trench isolation (STI) over the photoactive area (PA) ratio for the given TIDs. Larger STI area results in more degradation of the SR curve, thus the optical performance of Device 1 degraded the most.

**Table 5.6.** Spectral responsivity (SR) degradation on the target wavelengths, after TID = 400 Gy(Si) for the four analyzed photodiodes at the operating conditions. The overall degradation is < 2.3 %, which is quite small indicating robustness and radiation-hardness of the devices.

Device #	STI/PA ratio [%]	ΔSR  @ target wavelengths, 1.25 V reverse bias, TID = 400 Gy(Si)			Average SR degradation ratio [%]
		510nm	670nm	780nm	
Device 1	5.79	0.011	0.008	0.013	-2.29
Device 2	4.61	0.008	0.007	0.008	-1.88
Device 3	3.50	0.006	0.005	0.003	-1.57
Device 4	3.18	0.004	0.003	0.004	-0.93

### 5.3. Summary

Both the pre- and post-irradiation measurements were performed at a semi-automated probestation. The contacts on the wafer were directly probed and electrical and optical measurements were carried out. Pre-irradiation measurements showed that the dark current depends mainly on the total number of islands and that an inconsistent spacing between the closest island and the STI lines leads to a small increase in the dark current. Furthermore, capacitance measurements showed a similar trend, where the total capacitance depends on the total number of islands. SR measurements introduced the relevance of optical fiber positioning above the photodiode surface. The wavelength spectrum range was between 400 nm and 900 nm, with the target wavelengths being 510 nm, 670 nm, and 780 nm respectively.

In terms of the dark current, the photodiode structures were radiation-hard up to TID = 200 Gy(Si) and only after the TID = 400 Gy(Si), the dark current increased by  $\Delta I = 320$  fA, which was around 10 – 16 % higher than the dark current before X-ray irradiation. Considering the measurement offset of ~ 50 fA, the dark current increase was constant for all four devices, implying that the increase of the dark current due to X-ray irradiation only depended on the critical region where the SCR reaches the un-passivated interface between the silicon oxide and the silicon. In that region, the TID induced defects increase the surface recombination velocity and widen the SCR, degrading the electrical performance and increasing the dark current.

In regard to the C-V characteristics, the photodiode structures were radiation-hard up to  $TID = 400 \text{ Gy(Si)}$ , implying that the change in the SCR width at the silicon oxide/silicon interface did not have a meaningful impact on the total SCR volume.

Finally, in optical characterization, it was important to calculate the systematic error, which was present in the measurements due to the fiber position misalignment between the measurements. After the measurement normalization, it can be concluded that all four photodiode structures are radiation-hard up to  $TID = 200 \text{ Gy(Si)}$ . After the  $TID = 400 \text{ Gy(Si)}$ , the SR degradation was constant over the wavelength range, with the maximum degradation in the range of  $\sim 2.3 \%$  for the device with the largest STI area, Device 1. Since the optical performance mainly depends on the diffusing optically generated minority carriers in the quasi-neutral region, between the islands and the area towards the guard-ring, some of them may get trapped at the STI/silicon interface, resulting in SR degradation.

## 6. Technology comparison (180 nm vs 350 nm)

The following chapter shows a comparison between the two *ams OSRAM* CMOS technologies. The prototype device was fabricated in the 350 nm CMOS technology, whereas the photodiode structures analyzed and measured in this dissertation were fabricated in the 180 nm technology. The maximum TID used in the experiments of the structures fabricated in 350 nm technology was  $TID = 200 \text{ Gy(Si)}$ , whereas in the case of the structures fabricated in the 180 nm technology, the dose was twice as high,  $TID = 400 \text{ Gy(Si)}$ . Since the comparison between the four photodiode structures, processed in 180 nm technology was analyzed in the previous chapter, only the first device, Device 1, will be considered in the technology comparison analysis. The comparison is given between the measured electrical and optical characteristics, that were previously analyzed in chapter 5. Finally, the radiation-hardness of both technologies is discussed in order to determine the performance and robustness of both technologies.

### 6.1. Current-voltage characteristics comparison

Based on the analysis of the post-irradiation measurements presented in chapter 5.2.1, it was concluded that the photodiode structures processed in 180 nm CMOS technology were radiation-hard up to  $TID = 200 \text{ Gy(Si)}$ . In order to compare the radiation hardness of the two similar photodiodes, fabricated in 180 nm and 350 nm CMOS technologies, a qualitative comparison of the pre- and post-irradiation dark current measurements at  $T = 323 \text{ K}$  is shown in Figure 6.1. Comparing the dark current before X-ray irradiation, it can be concluded that the photodiode structures processed in 180 nm CMOS technology have slightly higher dark current, due to layout modifications, such as the STI lines. Even though the STI is partially passivated with the SPI, there are still interface traps located at the STI/Si interface, contributing towards the increase of the dark current before X-ray irradiation. On the other hand, after two times higher irradiation dose, structures processed in 180 nm technology showed significantly lower dark current than the structures processed in 350 nm technology. After the  $TID = 400 \text{ Gy(Si)}$ , the dark current increases by only 15 % for the first photodiode structure processed in 180 nm technology, compared to the increase of 89 % of the structures processed in 350 nm technology already after the TID of 200 Gy(Si). In terms of absolute values, this is a 38 % reduction in dark current after a TID of 200 Gy(Si) in the 180 nm technology, compared to 350 nm technology. The photodiodes processed in 350 nm technology do not have the nitride layer. Instead, a thicker oxide layer is deposited directly on the surface. In addition to that, LOCOS oxide is used instead of the STI. A higher radiation hardness in 180 nm technology could be attributed

to the additional trapping of positive charges in the nitride layer, that compensates the effect of the interface traps. Apart from the technology differences described above, small differences in other parameters, such as differences in thermal budget and in the doping profiles further contribute to the radiation hardness of the photodiodes processed in 180 nm technology [102].

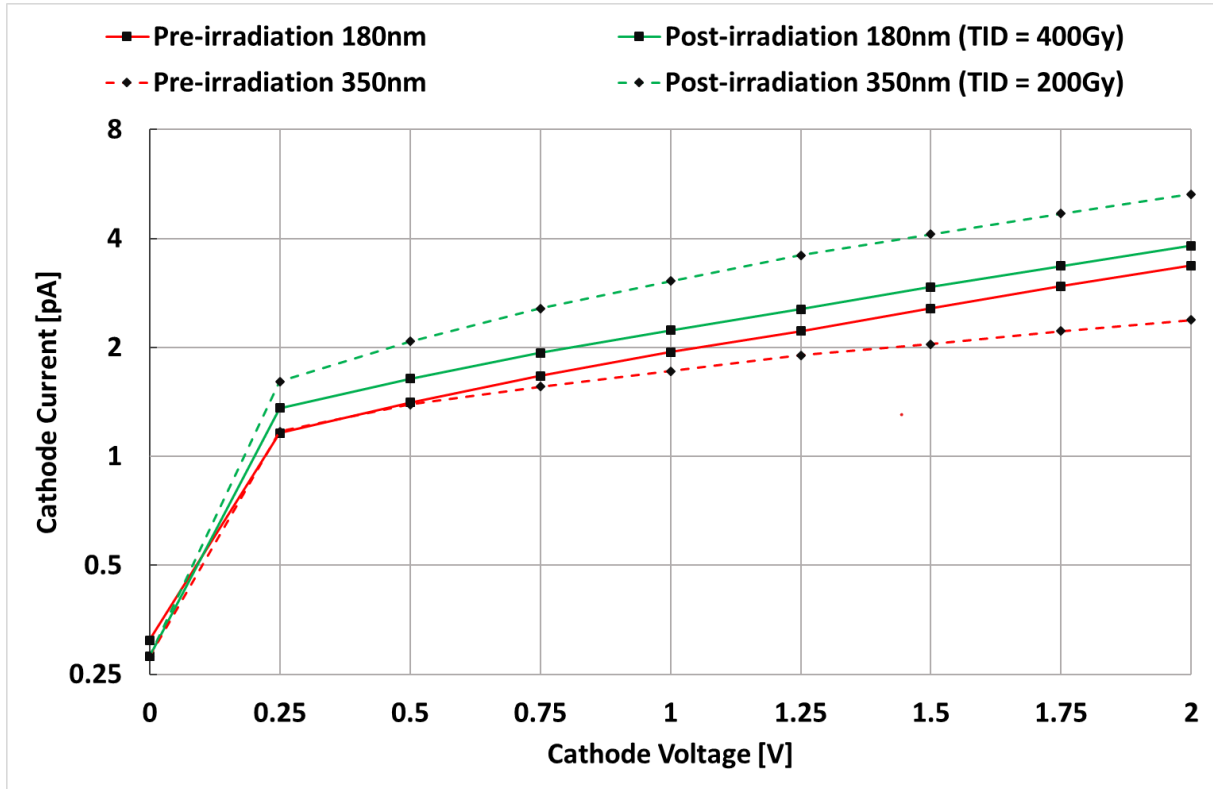


**Figure 6.1.** Comparison of the pre- and post-irradiation dark current measurements between photodiodes fabricated in 180 nm (Device 1) and 350 nm technologies, at  $T = 323$  K. Photodiodes processed in 350 nm technology shows lower pre-irradiation current. On the other hand, after the TID = 400 Gy(Si), the dark current increases by only 15 % for the first photodiode structure processed in 180 nm technology, compared to the increase of 89 % of the structures processed in 350 nm technology already after the TID of 200 Gy(Si) [102].

## 6.2. Capacitance-voltage characteristics comparison

Comparison of the capacitance values between the two similar photodiodes fabricated in the two previously mentioned CMOS technologies, is shown in Figure 6.2. Comparing the capacitance values between the technologies, it is concluded that the photodiodes fabricated in 350 nm technology show lower capacitance values in both cases, before and after X-ray irradiation. On the other hand, the radiation hardness of the photodiodes processed in the 180 nm technology is better as there is no change in the capacitance values, compared to the degradation of  $\sim 3 - 4$  % in the case of 350 nm technology. Technological differences, such as different thermal budget, implant conditions and steepness of doping profiles contribute to the

narrowing of the SCR in the area where the highly doped p-type surface implant overlaps with the NW, thus increasing capacitance of the photodiodes fabricated in 180 nm technology. On the other hand, the aforementioned technological differences and the addition of the thin nitride layer improve the radiation hardness of the photodiodes fabricated in 180 nm technology, similar to the conclusion made in chapter 6.1.

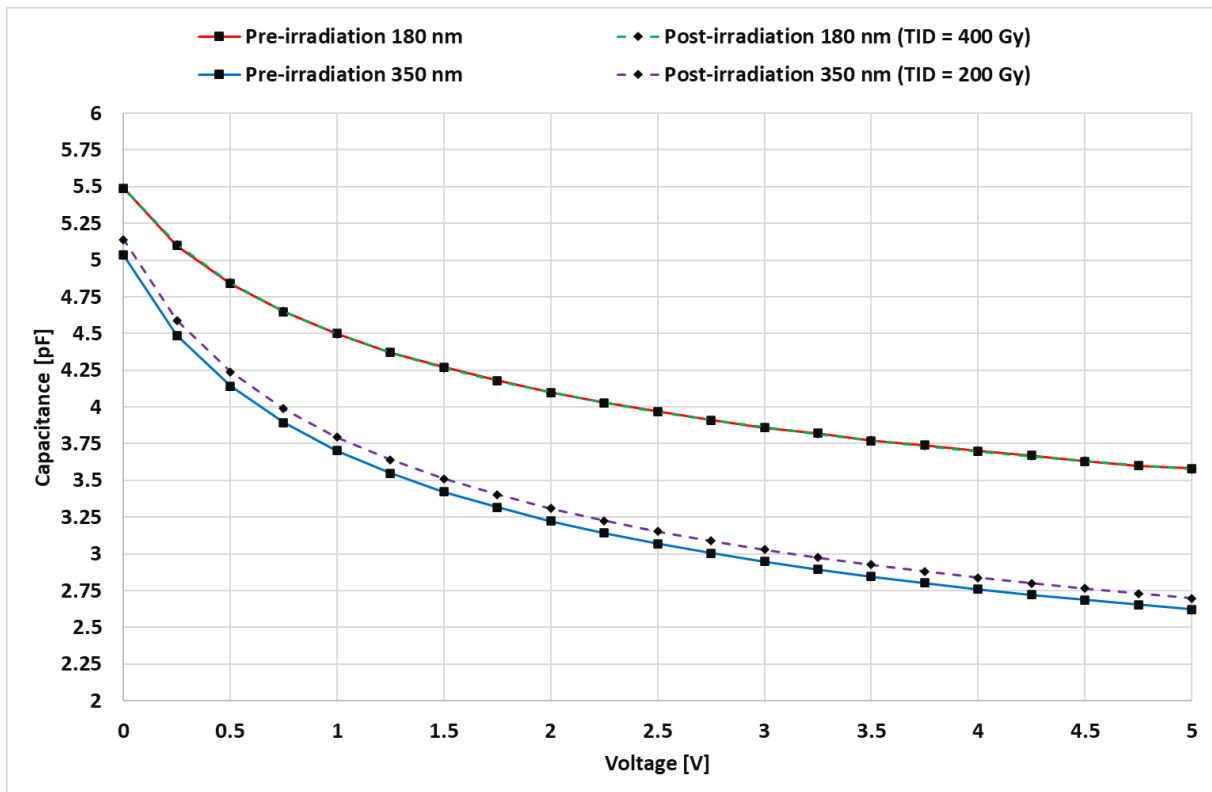


**Figure 6.2.** Comparison of the two similar photodiode structures, fabricated in 180 nm (Device 1) and 350 nm CMOS technologies, respectively. Structures fabricated in 350 nm technology show lower capacitance before and after X-ray irradiation, whereas the radiation hardness of the structures fabricated in 180 nm technology is better, as the capacitance is not affected by irradiation exposure at all.

### 6.3. Spectral responsivity characteristics comparison

Finally, a SR characteristics comparison between the two technologies is depicted in Figure 6.3. The structures processed in 180 nm technology show minor degradation after TID = 400 Gy(Si), whereas the structures processed in 350 nm technology are radiation-hard up to TID = 200 Gy(Si). On the other hand, the photodiodes processed in 180 nm technology node perform much better than the similar device processed in 350 nm technology, showing an increase in responsivity values between 20 – 45 % over the whole spectrum range. The difference in SR values between the two photodiode structures, before X-ray irradiation, is shown in Figure 6.4. The curve was smoothed by calculating the moving average of the ratio. The moving average calculation excludes the first few points, equal to the size of the interval - 1, thus the first few



plot points are missing. At lower wavelengths ( $< 450$  nm), the difference is in the range of 30 – 45 % and as the wavelength increases, the difference becomes smaller, averaging around ~ 20 – 25 %. The improvement in SR comes from the fact that the thin nitride layer acts as an anti-reflective coating (ARC) layer, mainly increasing the SR values at lower wavelengths (400 – 600 nm), while moderately improving the responsivity at higher wavelengths (600 – 900 nm).

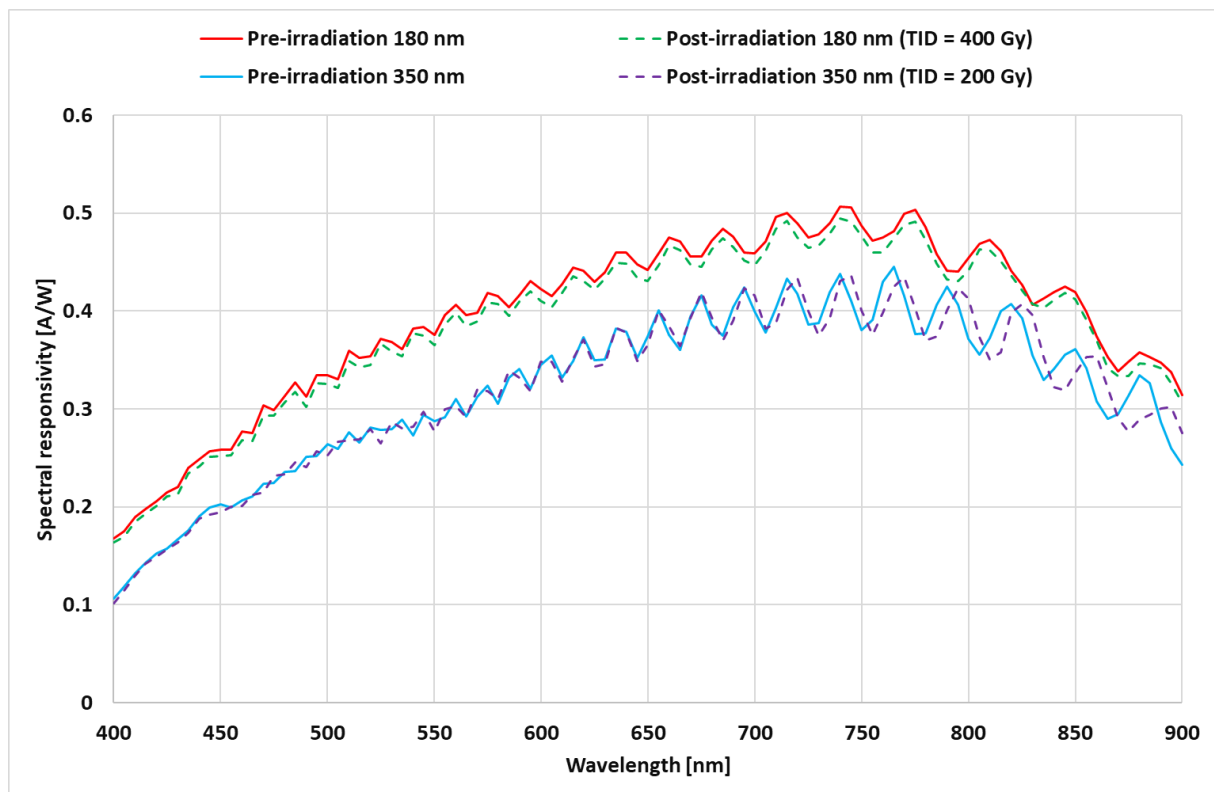


**Figure 6.3.** Comparison of pre- and post-irradiation spectral responsivity (SR) characteristics for the two photodiode structures fabricated in 180 nm (Device 1) and 350 nm CMOS technologies, respectively. The photodiodes processed in 350 nm technology are radiation-hard up to TID = 200 Gy(Si). On the other hand, the photodiode processed in 180 nm technology node performs much better than the similar device processed in 350 nm technology, showing an increase in SR values between 20 – 45 % over the whole spectrum range.

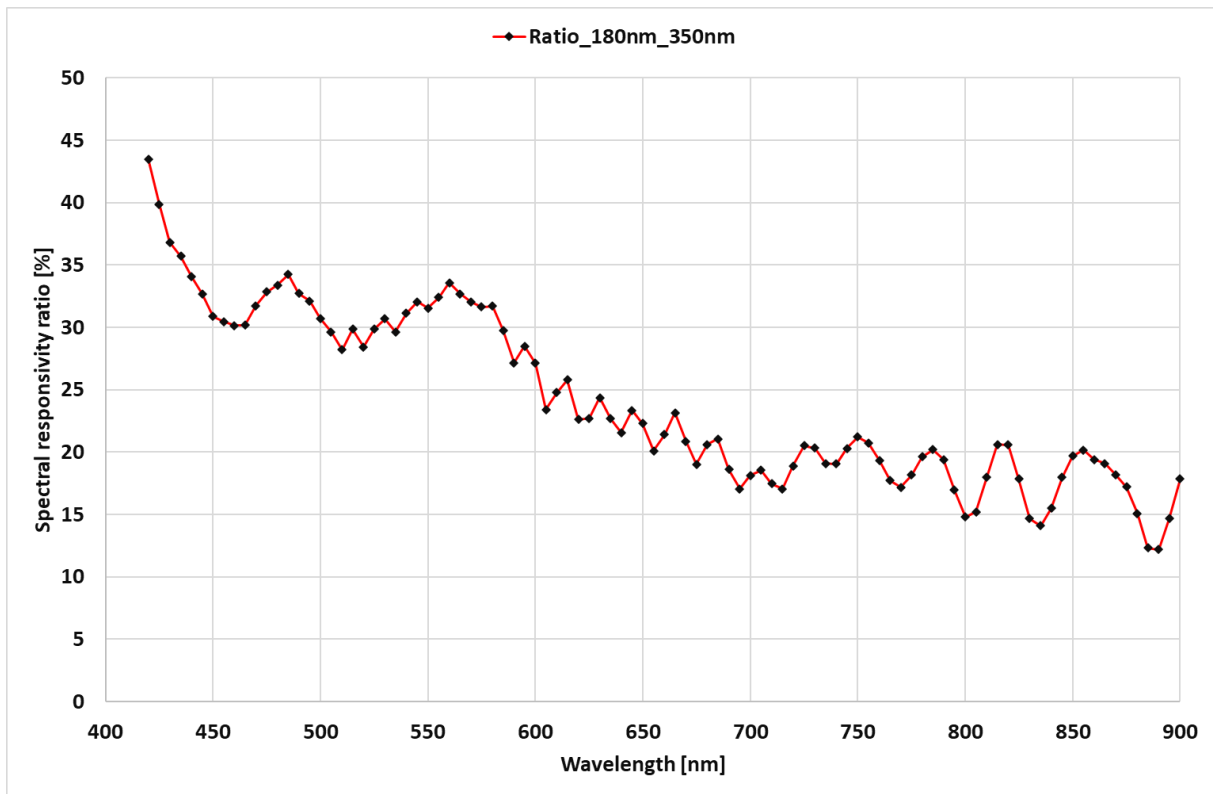
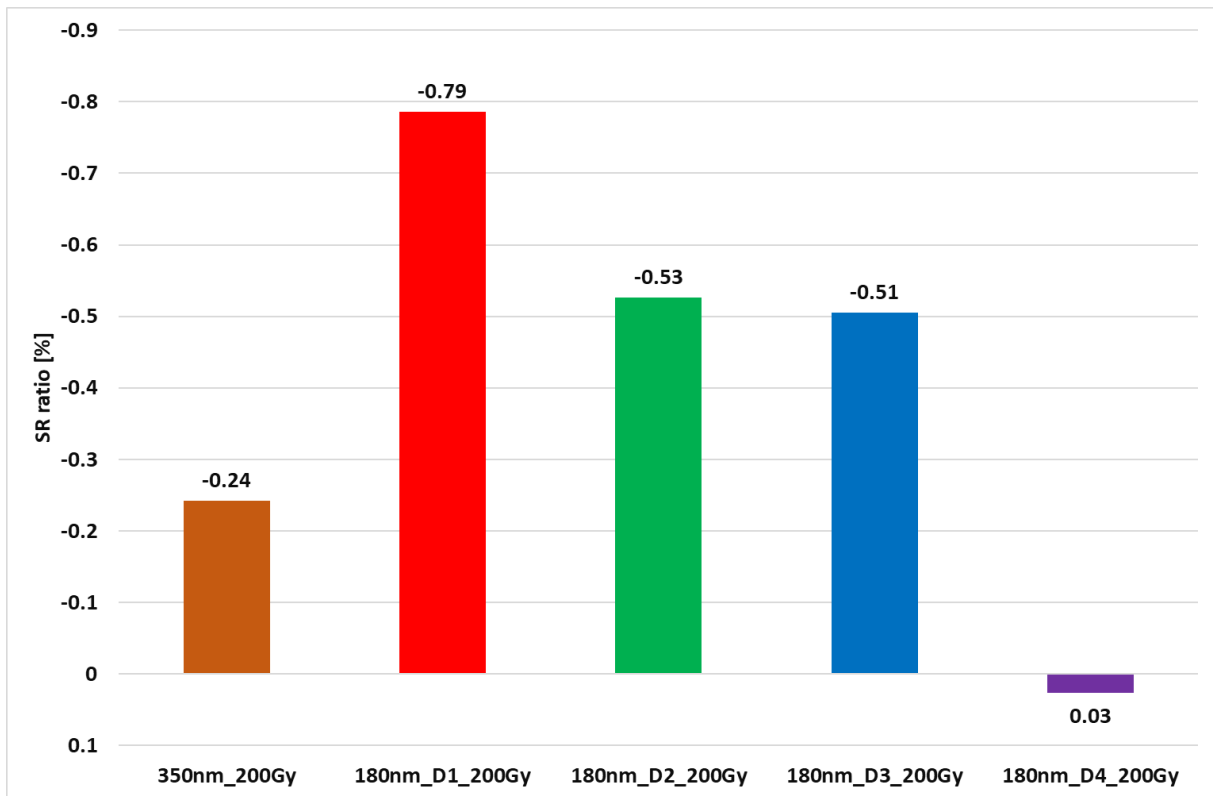
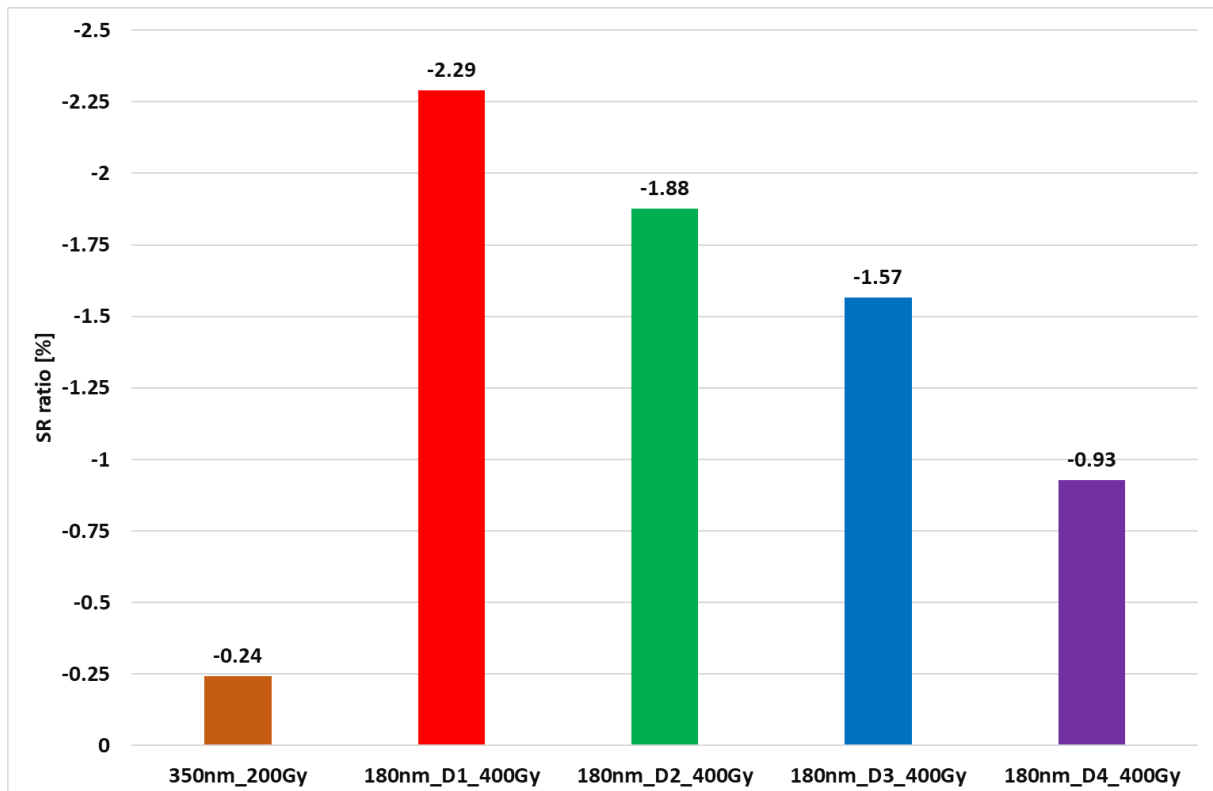


**Figure 6.4.** The difference in spectral responsivity (SR) values between the two photodiode structures, before X-ray irradiation. The photodiodes processed in 180 nm technology (Device 1) have 20 – 45 % higher SR over the wavelength spectrum, compared to the photodiodes processed in 350 nm technology.

The next point to consider is the radiation hardness of the optical performance of the two presented CMOS technologies. In both cases, the degradation was constant and present over the whole wavelength range (400 – 900 nm). In the case of 180 nm technology, all four photodiode structures were plotted. In Figures 6.5. a) and b), a comparison is given between the two technologies, relative to the maximum TID used during the experiments in the 350 nm technology and 180 nm technology, respectively. After the TID = 200 Gy(Si), both technologies are radiation-hard, as the maximum degradation is in the range of 0.79 % in the case of the first device fabricated in 180 nm technology, which had the largest STI/PA ratio. After the TID = 400 Gy(Si), the degradation of photodiodes processed in 180 nm technology slightly increases, up to 2.29 %, as previously discussed in chapter 5.2.3. The small difference in the radiation hardness, between the two technologies, is due to the STI that was implemented in 180 nm technology in order to allow correct processing.



a)



b)

**Figure 6.5.** a) Comparison of the radiation hardness of the spectral responsivity (SR) of the two technologies at TID = 200 Gy(Si) and b) TID = 400 Gy(Si). After the TID = 200 Gy(Si), both technologies are radiation-hard, as the maximum degradation in the range of 0.79 % in the case of the first device fabricated in 180 nm technology. After the TID = 400 Gy(Si), the degradation is in the range of ~ 2.3 % for the structures processed in 180 nm technology. The small difference in the radiation

hardness, between the two technologies, is due to the STI that was implemented in 180 nm technology in order to allow correct processing.

Furthermore, a comparison in normalized photo-to-dark current ratio (nPDR) degradation after TID = 400 Gy(Si) in the case of photodiode processed in 180 nm technology (Device 1), and TID = 200 Gy(Si) in the case of the photodiode processed in 350 nm technology, is depicted in Figure 6.6. In both technologies the dark current degradation was more affected by the TID, compared to the SR. It is therefore concluded that the nPDR is dominantly impacted by the dark current increase after the TID. The degradation of the nPDR was in the range of 15 % for the photodiodes processed in 180 nm technology, compared to 45 % – 50 % degradation for the photodiodes processed in 350 nm technology.

Since the photodiodes in both technologies are linear over a wide range of the incoming light intensities, the nPDR was calculated by normalizing the photocurrent by the optical power and then dividing it with the dark current value, at the operating temperature and bias conditions. The normalized photocurrent is in fact spectral responsivity. This way, the change in the optical power, which was in the order of ~ 20 % between the pre- and post-irradiation measurements, and hence in the photocurrent, is mitigated.

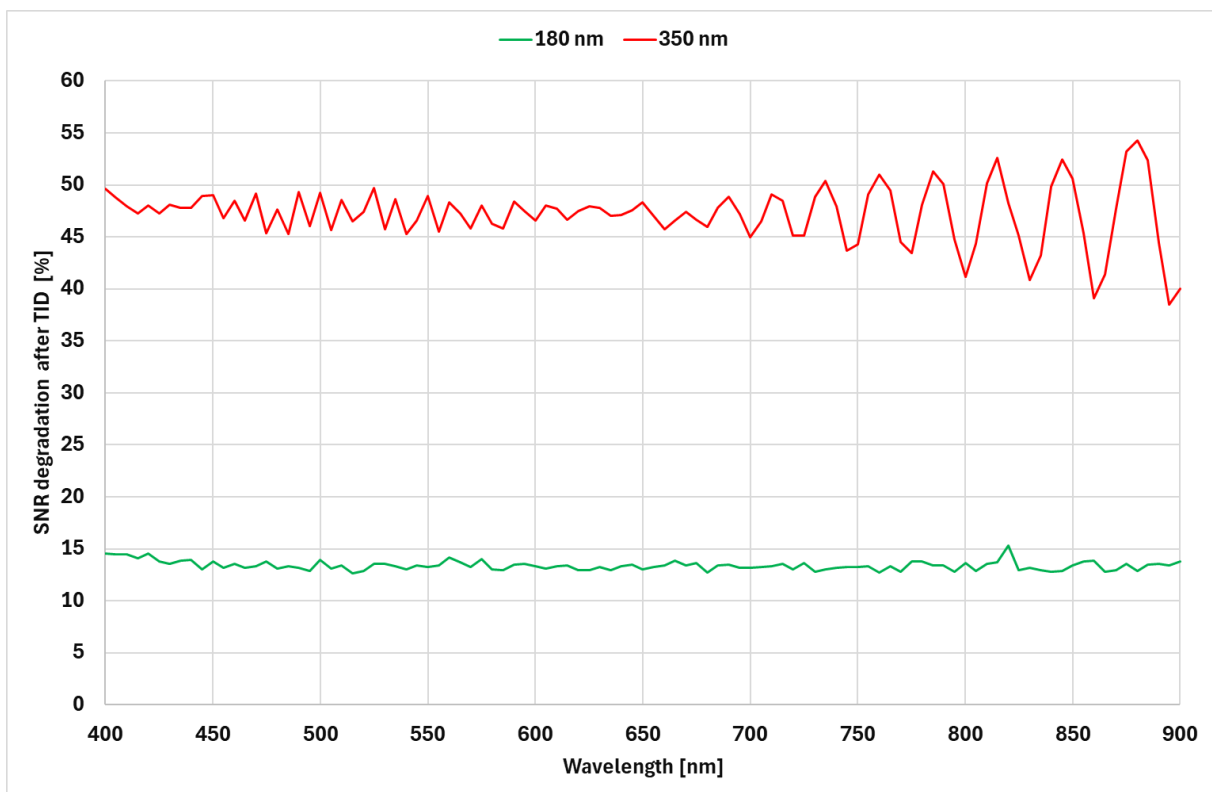


**Figure 6.6.** Comparison of normalized photo-to-dark current ratio (nPDR) degradation after X-ray irradiation: TID = 400 Gy(Si) in the case of the 180 nm technology (Device 1) and TID = 200 Gy (Si) in the case of the 350 nm technology.

Finally, in order to improve the radiation hardness of the structures fabricated in 180 nm technology, further optimization of the STI lines can be made, e.g. the width of the STI lines, in order to mitigate both the spectral responsivity and the dark current before and after X-ray irradiation. Furthermore, the SPI should also be implemented below the STI in order to passivate the interface against TID induced defects.

#### **6.4. Summary**

The summary of technology comparison is shown in Table 6.1. It shows comparison in dark current, capacitance and SR at operating conditions and target wavelengths as well as the difference in characteristics values after X-ray exposure. Photodiodes processed in 180 nm technology are labeled D1 – D4, and the photodiode processed in 350 nm technology is labeled as D350.

Even though the dark current before X-ray irradiation was smaller for the photodiode structures fabricated in 350 nm CMOS technology, after the TID = 200 Gy(Si), the dark current increased by 89 %. On the other hand, the photodiode structures fabricated in the 180 nm CMOS were radiation-hard up to TID = 200 Gy(Si) and only had dark current degradation up to 16 % after TID = 400 Gy(Si). In terms of absolute values, this is a 38 % reduction in dark current after a TID of 200 Gy(Si) in the 180 nm technology, compared to 350 nm technology. A possible explanation for higher radiation hardness in 180 nm technology could be the additional trapping of positive charges in the nitride layer, that compensates the effect of the interface traps. Additionally, small differences in other parameters, such as differences in thermal budget and in the doping profiles further contribute to the radiation hardness of the photodiodes processed in 180 nm technology.

In terms of photodiode capacitance, devices fabricated in 180 nm technology had higher capacitance before and after irradiation, compared to the similar photodiodes fabricated in 350 nm technology. On the other hand, the photodiodes fabricated in 350 nm technology had a degradation of ~ 3 – 4 % after TID = 200 Gy(Si), whereas the photodiodes fabricated in 180 nm technology were radiation-hard up to TID = 400 Gy(Si). Technological differences, such as different thermal budget, implant conditions and steepness of doping profiles contribute to the increasing capacitance of the photodiodes fabricated in 180 nm technology. On the other hand, the aforementioned technological differences and the addition of the thin nitride layer improve the radiation hardness of the photodiodes fabricated in 180 nm technology.

Finally, the SR of the photodiodes fabricated in 180 nm technology was 20 – 45 % higher, than the SR of the similar devices fabricated in 350 nm technology. In terms of radiation

hardness, after the TID = 400 Gy (Si) there was a small degradation of the SR, ranging between 0.93 and 2.29 %, in case of the devices fabricated in 180 nm technology. The reason for that degradation are the STI lines, which were implemented in 180 nm technology in order to allow correct processing.

In addition to that, a comparison in normalized photo-to-dark current ratio (nPDR) degradation after TID = 400 Gy(Si) in the case of photodiode processed in 180 nm technology (Device 1), and TID = 200 Gy(Si) in the case of the photodiode processed in 350 nm technology, is analyzed. In both technologies the dark current degradation was more affected by the TID, compared to the SR. It is therefore concluded that the nPDR is dominantly impacted by the dark current increase after the TID. The degradation of the nPDR was in the range of 15 % for the photodiodes processed in 180 nm technology, compared to 45 % – 50 % degradation for the photodiodes processed in 350 nm technology.

Furthermore, in order to improve the radiation hardness of the structures fabricated in 180 nm technology, further optimization of the STI lines can be made, e.g. the width of the STI lines, in order to mitigate the degradation of both the SR and the dark current before and after X-ray irradiation. Comparing the radiation hardness of the similar photodiodes between the two CMOS technology, at the same TID = 200 Gy(Si), it can be concluded that both structures are radiation-hard, as the degradation is < 0.8 %.

**Table 6.1.** The summary of technology comparison: absolute dark current ( $I_{\text{Dark}}$ ), capacitance (Cap) and spectral responsivity (SR) values at the operating conditions. Additionally, the differences in values of each analyzed characteristics, after X-ray exposure, is also given. Photodiodes processed in 180 nm technology are labeled D1-D4, and the photodiode processed in 350 nm technology is labeled as D350.

	$I_{\text{Dark}} @ 1.25\text{V}, 50^\circ\text{C}$		$\text{Cap} @ 1.25\text{V}, 27^\circ\text{C}$		$\text{SR} @ 1.25\text{V}, 27^\circ\text{C}$					
	Pre-Xray [pA]	$\Delta I$ [fA]	Pre-Xray [pF]	$\Delta C$ [fF]	Pre-Xray, [A/W]			$\Delta \text{SR}$ [A/W]		
					510nm	670nm	780nm	510nm	670nm	780nm
<b>D350</b>	1.90	1690	3.55	90	0.276	0.395	0.377	0.008	0.008	0.008
<b>D1</b>	2.73	330	4.37	1.39	0.356	0.460	0.489	0.011	0.008	0.013
<b>D2</b>	2.63	370	4.38	1.86	0.359	0.460	0.488	0.008	0.007	0.008
<b>D3</b>	2.77	280	4.40	1.12	0.357	0.462	0.491	0.006	0.005	0.003
<b>D4</b>	3.66	300	4.43	-2.76	0.356	0.466	0.498	0.004	0.003	0.004

## 7. Electrical and optical characteristics analysis and simulations

The following chapter will present and discuss the TCAD simulations of the key regions in the analyzed photodiode structures that are affected by X-ray irradiation.

First, a cross-section of a photodiode structure simulated in *ams OSRAM* 350 nm CMOS technology is presented. In the design of the radiation-hard photodiodes, it is important to understand the impact of different geometrical and physical parameters. Using TCAD Sentaurus software [106], it is possible to simulate a statistical variability experiment of these parameters. Furthermore, the statistical calibration methodology of the input parameters that define the dark current and SR of the photodiodes fabricated in 350 nm CMOS technology is used to calibrate the pre-irradiation simulations with the respective measurements. Satisfactory calibration is achieved in both the dark current and SR simulations, with a small mismatch present in the optical simulations since the simulation domain was quite simplified, compared to the real device.

Next, a cross-section of the photodiode fabricated in *ams OSRAM* 180 nm CMOS technology is shown. A similar statistical methodology was used to calibrate the dark current and capacitance simulations, before and after X-ray irradiation, with their respective measurements. In post-irradiation simulations, screening and modeling of the X-ray induced defects, such as the fixed charges in the insulating layers and interface traps at the silicon oxide/silicon interface, was used to calibrate the simulations with the measurements. Due to the complexity of the layout of the photodiode structure in 180 nm technology, e.g. the STI lines, the optical simulations were not performed. Instead, a short discussion, covering the impact of the STI on the optical performance, as well as the passivation of the STI with the SPI layer is given. Dark current simulations showed appropriate fitting over a larger voltage range, focused around the operating bias conditions, in both pre- and post-irradiation simulations. Capacitance simulations confirmed that there is no change in the capacitance values due to the added irradiation-induced defects. The mismatch between the capacitance simulations and the measurements is present because the parasitic capacitance components coming from metallization lines, ILDs, etc., were omitted in the simulations.

Finally, a TID model is presented, which considers the effects of the TID induced defects on the critical photodiode regions. In the proposed model, the impact of the energy levels of acceptor and donor interface traps, relative to the quasi-Fermi energy level, in combination with the added fixed charges in the insulating layers, on the surface SCR width is given as a possible

explanation for better radiation hardness of photodiodes processed in 180 nm technology compared to the similar photodiodes processed in the 350 nm technology node.

### **7.1. Simulated photodiode structure in *ams OSRAM* 350 nm CMOS technology**

There are different geometrical factors that influence the reverse and the forward I-V characteristics, as well as the SR, thus the simulation domain was divided in multiple segments.

The first simulation domain, describing the reverse bias cross-section of the photodiode processed in *ams OSRAM* 350 nm CMOS technology, is modeled by one-island structure and its periphery, as shown in Figure 7.1. [107]. The simulated photodiode structure consists of a small circular NW island that is surrounded by a highly-doped shallow p-type passivation ( $N_A > 10^{19} \text{ cm}^{-3}$ ) layer. It is positioned in the high-lifetime p-type epitaxial layer, which was thermally grown on top of the low resistivity p-type substrate material [107]. The out-diffusion region is the area between the substrate and the epitaxial layer where the gradient in the doping profile is present. The total simulation domain was equal to the spacing between the neighbouring two islands, with the symmetry point located at the central point of the NW island. In 2D simulations, the third dimension is defined by an area factor which extends the structure in the Z-direction. By default, the area factor is fixed to 1  $\mu\text{m}$ . This results in the NW island to have a rectangular shape in the TCAD simulations. Because of that, area normalization is required where the rectangle top-view of the 2D TCAD simulation is adjusted to the circular top-view of the fabricated NW island. Furthermore, a statistical Design of Experiment (DoE) is introduced in order to calibrate the simulations with the measurements. This will be further discussed in the following two chapters. Finally, since the fabricated photodiode consists of 242 NW islands, the simulations are normalized to the total number of NW-islands in order to achieve satisfactory dark current fitting with the measurements.

In the case of SR simulations, the same one-island structure was simulated, but with larger area factor. Since the photocurrent depends on lifetime of minority carriers in the quasi-neutral region, the area factor was adjusted such to compensate for the small periphery of the one-island simulation domain. In optical simulations, quantum yield models are used that describe how many of the absorbed photons are converted to generated electron-hole pairs. Photon absorption in silicon is modeled with the complex refractive index (CRI) model where wavelength dependency of the refractive index and extinction coefficient values is implemented. Transfer matrix method (TMM) is the optical solver model that is used in the simulations. With TMM,



the amplitudes of forward and backward running waves in each layer of the structure are calculated with the help of transfer matrices [107].

In forward bias characteristics, the charge carriers are injected from the island region towards the quasi-neutral periphery. Therefore, a multiple-island structure was implemented in order to simulate the influence of the neighboring islands and the peripheral area of the photodiode on the forward current. The simulation domain is depicted in Figure 7.2. and it includes seven NW islands, named C1 – C7, as well as the left and the right guard-rings. Each of the islands has the same cross-section as the island shown in Figure 7.1. The bias was applied on the cathode contact of each island, whereas the anode and the guard-ring contacts were grounded. The fabricated photodiode consists of rows and columns of alternating number of NW islands. That is 12 and 11 islands in rows and 11 and 10 islands in columns. The simulated structure was minimized to 7 islands, as the middle island, C4, represents the central islands of the 242-island structure, where each of the central islands contribute equally to the total forward current. The islands C1 – C3 have slightly different contributions due to different peripheral areas which surround the islands. For example, the island C1 only has one island next to it, island C2, whereas on the other side, there is a large gap between the island and the guard-ring. Therefore, the contribution of C1 will be the highest on the forward characteristics. The structure is symmetrical, meaning that islands C5 – C7 will have the same impact as islands C3 – C1 on the forward characteristics. The contribution of each island to the total forward current, where the NW bias was swept from 0 V to -1 V, is shown in Figure 7.3. The seven-island structure was scaled to 242 islands by multiplying each island in the simulation, by the number of corresponding islands in the fabricated photodiode structure.

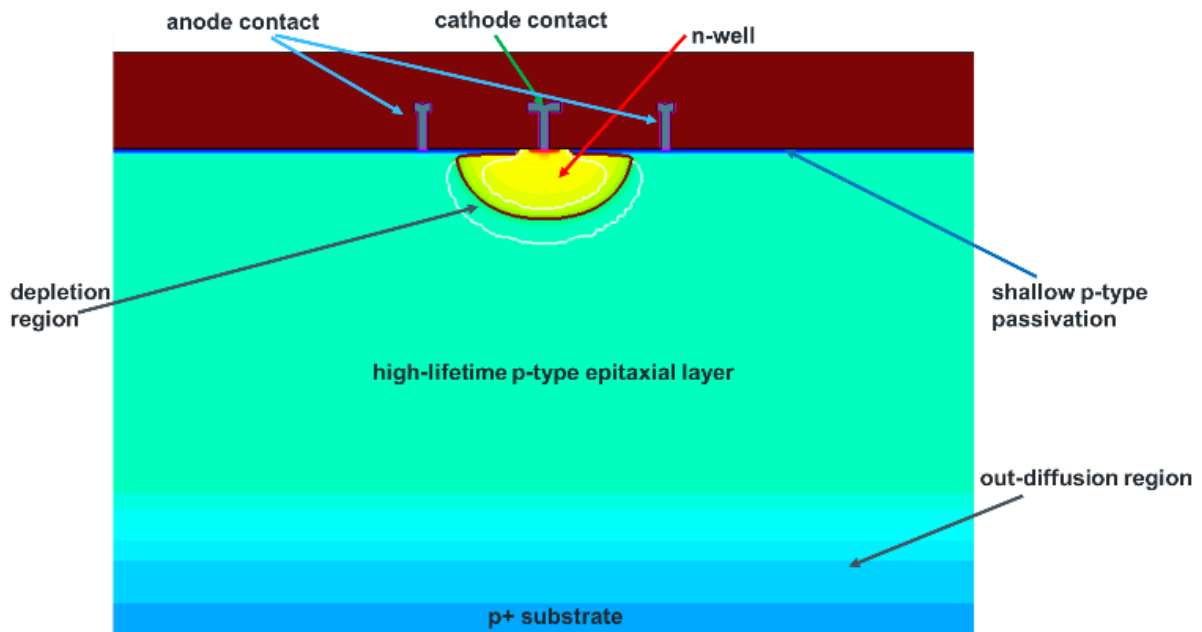


**Figure 7.1.** Cross-section of the simulated reference photodiode processed in *ams OSRAM* 350 nm CMOS technology. The cathode bias was 1.25 V, whereas the anode contacts were grounded. The photodiode consists of a small N-Well (NW) island that is surrounded by highly-doped shallow p-type passivation ( $N_A > 10^{19} \text{ cm}^{-3}$ ) layer. It is positioned in the high-lifetime p-type epitaxial layer, which was thermally grown on top of the low resistivity p-type substrate material. The out-diffusion region is the area between the substrate and the epitaxial layer where a gradient in doping profile is present [107].

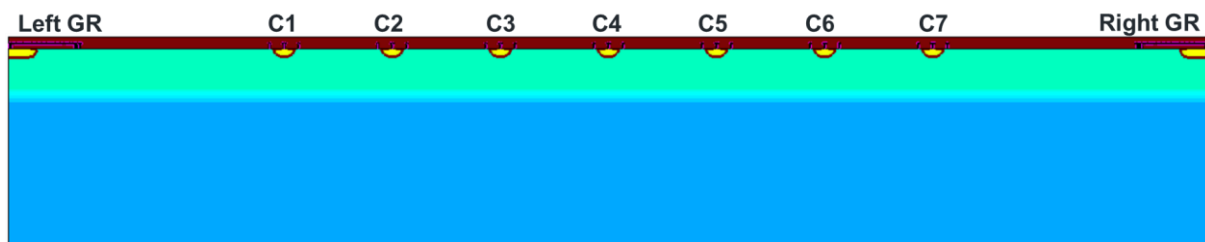


**Figure 7.2.** The simulation domain of the forward current-voltage (I-V) characteristics. It consists of N-Well (NW) seven islands, named C1 – C7, which are surrounded by the guard-rings (GR) that are placed left and right of each of the outmost NW islands. Bias was applied on each of the NW islands, whereas the anode and the GR contacts were grounded. The structure is symmetrical, meaning that islands C5, C6 and C7 yield the same forward current contribution as islands C3, C2 and C1 respectively. C4 island represents the central islands of the 242-island structure, where each of the central islands equally yields to the total forward current.

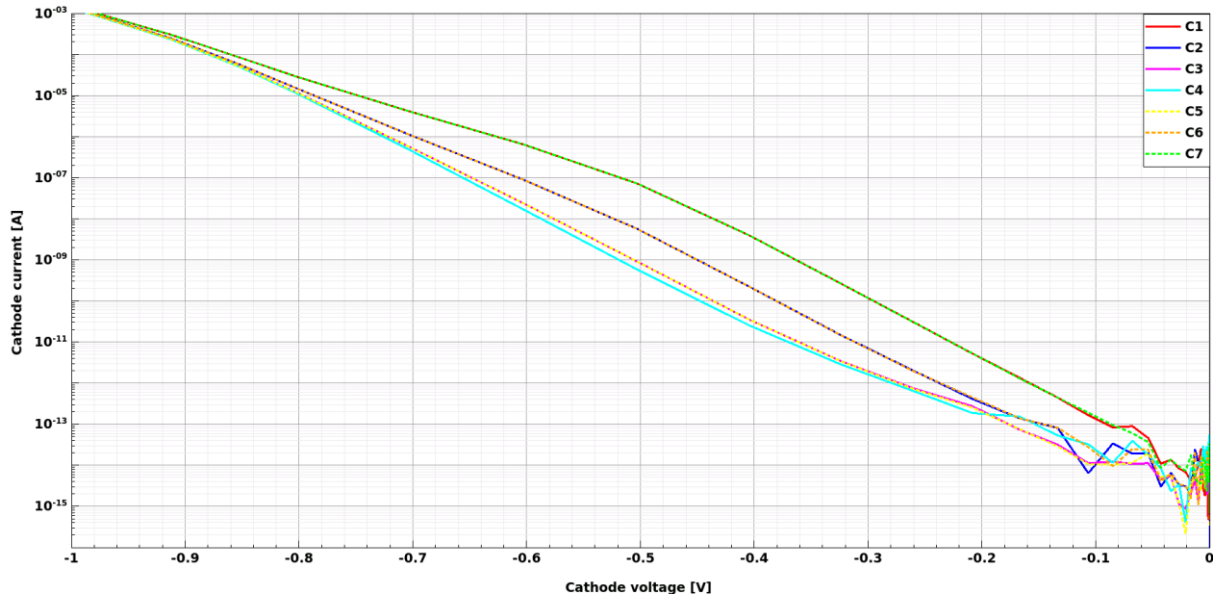


**Figure 7.3.** Current contribution of each of the seven islands on the forward characteristics. Cathode bias is swept between 0 V and -1 V, whereas the anode and the guard-ring (GR) contacts were grounded. For the larger peripheral area that surrounds the island, the current contribution of that island will be higher. Therefore, islands C1 and C7 have the highest contribution, whereas the island C4 has the lowest contribution on the forward current. The symmetry in forward current contribution between islands C1 – C3 and C7 – C5 can be observed.

## 7.2. TCAD parameter variability for calibration of pre-irradiation simulations

Simulation calibration with the measurements included different physical parameters, that were varied within their physical range. The simulations of these varied parameters give information on how each parameter impacts the observed responses, i.e. the dark current and the SR characteristics. In Table 7.1., parameters with their initial values are shown [107]. The parameters are placed in four groups, where each group describes different physical settings: energy bandgap, doping dependent mobility, Shockley-Read-Hall (SRH) recombination and Auger recombination.

**Table 7.1.** Simulation input parameters and their initial values. Parameters are shown in 4 groups that describe energy bandgap, doping-dependent mobility, Shockley-Read-Hall (SRH) recombination and Auger recombination settings [107].

Variability table		
<i>Group</i>	<i>Parameter</i>	<i>Initial value</i>
Energy bandgap	$E_{g0}$	1.16964 eV
Doping dependent mobility of electrons	$\mu_{min1}$	52.2 cm <sup>2</sup> /Vs
	$\mu_{min2}$	52.2 cm <sup>2</sup> /Vs

	$\mu_l$	43.4 cm <sup>2</sup> /Vs
	$C_r$	9.68·10 <sup>16</sup> cm <sup>-3</sup>
	$C_s$	3.43·10 <sup>20</sup> cm <sup>-3</sup>
	$\alpha$	0.68
	$\beta$	2
SRH recombination	$\tau_{maxE}$	1 ms
	$\tau_{maxH}$	one third of $\tau_{maxE}$
Auger recombination	$A_{AE}$	6.7·10 <sup>-32</sup> cm <sup>6</sup> s <sup>-1</sup>
	$A_{AH}$	7.2·10 <sup>-32</sup> cm <sup>6</sup> s <sup>-1</sup>
	$B_{AE}$	2.45·10 <sup>-31</sup> cm <sup>6</sup> s <sup>-1</sup>
	$B_{AH}$	4.5·10 <sup>-33</sup> cm <sup>6</sup> s <sup>-1</sup>
	$C_{AE}$	-2.2·10 <sup>-32</sup> cm <sup>6</sup> s <sup>-1</sup>
	$C_{AH}$	2.63·10 <sup>-32</sup> cm <sup>6</sup> s <sup>-1</sup>
	$H_{AE}$	3.46667
	$H_{AH}$	8.25688
	$N_{0E}$	10 <sup>18</sup> cm <sup>-3</sup>
	$N_{0H}$	10 <sup>18</sup> cm <sup>-3</sup>

In simulations, the energy bandgap is calculated according to [108]:

$$E_g(T) = E_{g0} + \delta E_{g0} + \frac{\alpha T^2}{\beta + T}, \quad (7.1.)$$

where  $T$  is the temperature,  $E_{g0}$  is the energy bandgap at 0 K, and  $\alpha = 4.73 \cdot 10^{-4}$  eV/K and  $\beta = 636$  K are the material parameters.

Doping dependent mobility of electrons is modeled by the Masetti model [109, 110]:

$$\mu_{dop} = \mu_{min1} + \frac{\mu_{const} - \mu_{min2}}{1 + \left(\frac{N_{A,0} + N_{D,0}}{C_r}\right)^\alpha} - \frac{\mu_1}{1 + \left(\frac{C_s}{N_{A,0} + N_{D,0}}\right)^\beta}, \quad (7.2.)$$

where  $\mu_{min1}, \mu_{min2}, \mu_1$  are reference mobilities,  $C_r, C_s$  are reference doping concentrations,  $\alpha, \beta$  are the exponents,  $\mu_{const}$  is the low-doping reference mobility and  $N_{A,0}$  and  $N_{D,0}$  are acceptor and donor concentrations.

SRH parameters are modeled by the Scharfetter equation [111]:

$$\tau_{dop}(N_{A,0} + N_{D,0}) = \frac{\tau_{max}}{1 + \left(\frac{N_{A,0} + N_{D,0}}{N_{ref}}\right)^\gamma}, \quad (7.3.)$$

where  $N_{ref} = 10^{16} \text{ cm}^{-3}$  is the reference doping profile and  $\gamma = 1$  is the exponent. The electron effective mass is lower than that of the holes, therefore, the electron mobility is higher than the mobility of the holes. This results in longer electron diffusion lengths, than the diffusion length of holes. Furthermore, the lifetime of electrons is higher than the lifetime of holes, additionally increasing the electron diffusion length [112]. In TCAD it was modeled so that the maximum hole lifetime is one third of the maximum electron lifetime.

Auger recombination is modeled in TCAD by [113-115]:

$$R_{net}^A = (C_n n + C_p p)(np - n_{i,eff}^2), \quad (7.4.)$$

where  $n, p$  are electron and hole concentrations respectively and the  $n_{i,eff}$  is the effective intrinsic concentration.

$C_n$  and  $C_p$  parameters from equation (7.4.), are dependent on the Auger parameters and are calculated according to:

$$C_x(T) = \left( A_{A,x} + B_{A,n} \left(\frac{T}{T_0}\right) + C_{A,n} \left(\frac{T}{T_0}\right)^2 \right) \left[ 1 + H_x \exp\left(-\frac{x}{N_{0,x}}\right) \right], \quad (7.5.)$$

where  $x$  represents electrons ( $n$ ) or holes ( $p$ ) depending on whether electrons or holes are used.

The aforementioned parameters affect the generation/recombination rate of the minority carriers as well as their diffusion length, thus impacting the dark current and the SR. The consequence of varying these parameters will be analyzed in the next chapter. In addition to these parameters, different operating temperatures were simulated. Since the photodiodes are used in a CT scanner, where the operating temperature can go up to 67 °C (340 K), the simulations were performed at 320 K (spectral responsivity) and 340 K (spectral responsivity and dark current).

### **7.3. Statistical design of experiment**

In order to see the impact of the aforementioned parameters, the following calibration methodology is presented, and its block diagram is shown in Figure 7.4. [107]. In the first set of simulations, a study of the impact of each parameter within their physically defined range of variations is performed. The study highlights the relative contribution of each parameter to the responses considered, e.g. the dark current and the SR characteristics. The parameters that have negligible impact on the responses are then removed from the statistical experiment. Next, parameter screening is performed, where the remaining parameters are varied and sorted out according to the impact they have on photodiode electrical and optical characteristics. Based on the statistical significance, which is defined by the statistical model, all parameters which are statistically insignificant are also removed from the experiment. Finally, a response-surface model (RSM) is built with the remaining parameters. In the RSM, the observed responses are modeled as a quadratic relation of the remaining input parameters. The analysis of the DoE shows the variability of the simulated responses as a function of the varied parameters such that the simulations could be calibrated with the measurements [107]. The implemented methodology is presented in the following few paragraphs.

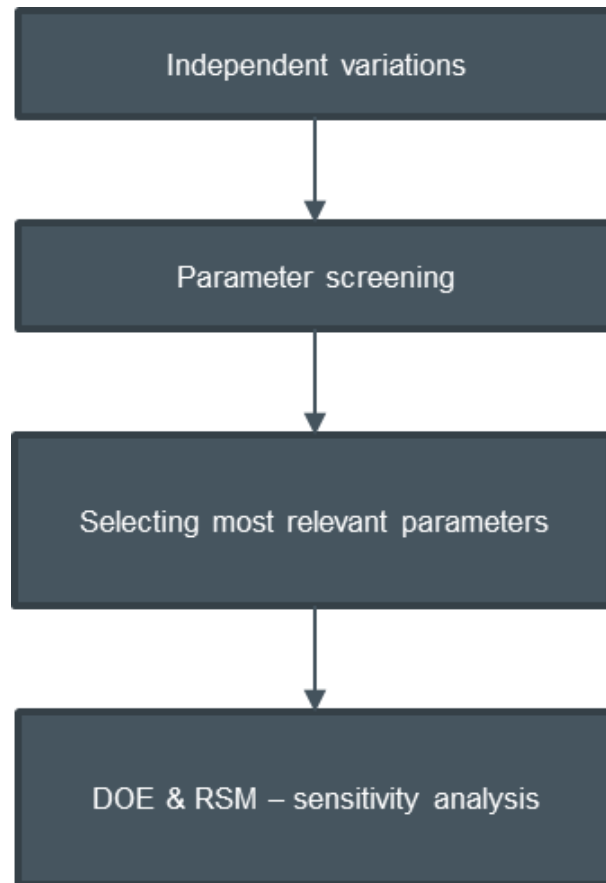


**Figure 7.4.** Block diagram of the calibration methodology. First, the input parameters are varied within their physical range to determine whether a parameter has an impact or not, on the observed responses. The remaining parameters are then screened based on the statistical model. Parameters that are statistically insignificant are removed from the experiment. Finally, the Response Surface Model (RSM) gives statistical parameter variability according to the quadratic relation of the remaining input parameters [107].

As an example of the independent variations step, the effect of varying the parameter  $\alpha$ , ranging from 0.374 to 0.986, and implemented in the doping dependent mobility equation (7.2.), is shown in Figure 7.5. [107]. It can be noted that the SR curve decreases in value as the parameter increases. Larger  $\alpha$  values mean that the minority carrier mobility is reduced, thus reducing the diffusion constant of the minority carriers as well. The optically generated charge carriers recombine at shorter distances, reducing the collection efficiency at the NWs, as seen in the reduced SR values. Furthermore, the variability of this parameter mostly influences shorter and longer spectrum regions. The absorption of the photons is determined by the absorption coefficient. At shorter wavelengths, the absorption of the photons is closer to the photodiode surface, where the SCR is placed. In that region, the doping levels are higher, either in NW or in p-passivation region implying a smaller mobility and a higher impact of  $\alpha$  for the same physical distance. At longer wavelengths, the light is absorbed deeper in the structure, partially in the substrate and also in the region with the out-diffusion from the substrate into the

epitaxial layer. The absorption region is further away from the collection electrode, and because of that the diffusion length and hence the charge carriers are more likely to recombine before reaching the depletion region. Therefore, the mobility has a higher impact in the longer wavelength spectrum region (800 nm – 900 nm) [107]. The same procedure is applied to each parameter from Table 7.1.

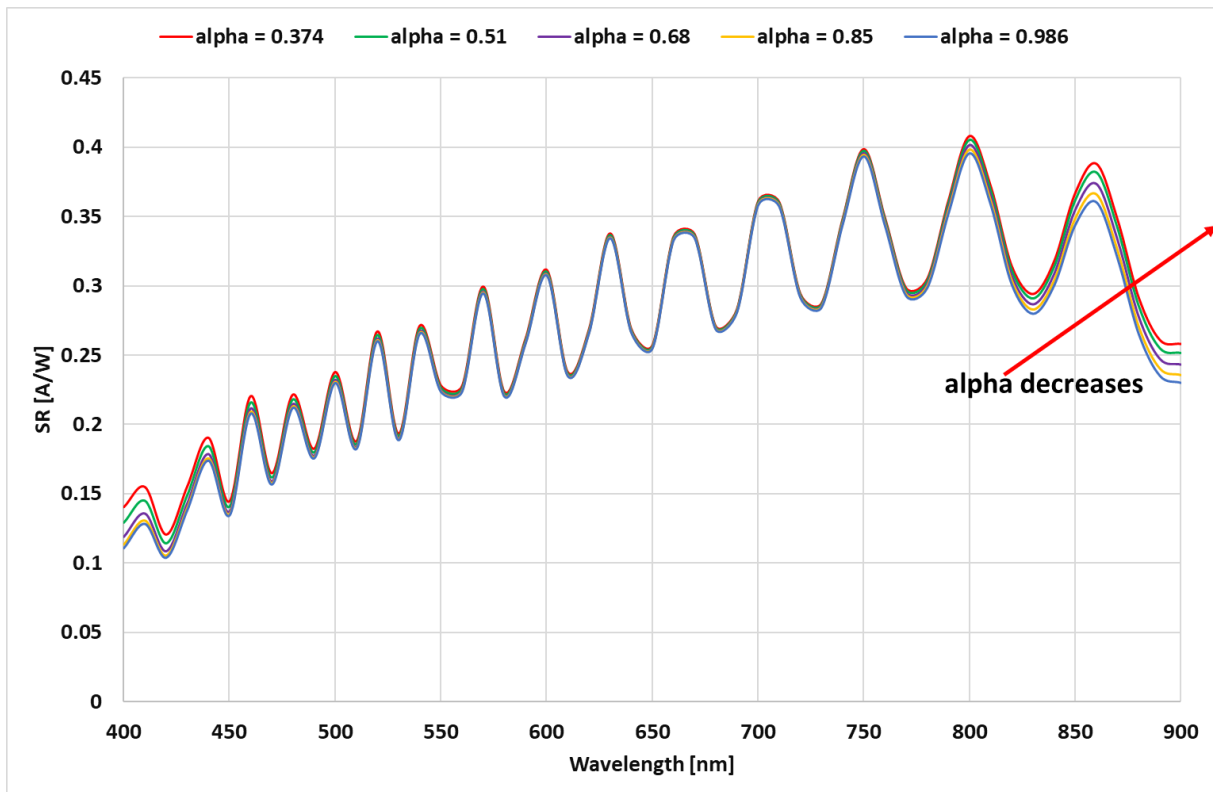


**Figure 7.5.** Impact of different  $\alpha$  values from equation (7.2.) on the spectral responsivity (SR) simulation at 340 K. Parameter  $\alpha$  is ranging from 0.374 to 0.986. The variation of parameter  $\alpha$  mainly influences shorter and longer spectrum regions. For larger  $\alpha$  values, mobility is reduced, resulting in a shorter diffusion length of the minority carriers, thus reducing the SR at longer wavelengths (800 nm – 900 nm). At shorter wavelength range (400 nm – 550 nm), absorption of the photons is closer to the surface of the photodiode where the space charge region (SCR) is placed. In that region, the doping levels are higher, either in N-Well (NW) or in p-passivation region implying a smaller mobility and a higher impact of  $\alpha$  for the same physical distance [107].

In the screening design, the L24 Plackett and Burman model has been generated in Minitab software [116]. The L24 model minimizes the total number of parameter variation combinations by omitting some combinations, while still preserving the relevant statistical significance. The screening percentages of all input parameters are selected such that the parameter values are in physical range of their initial values. In Table 7.2., the screening percentages of each input parameter are shown [107]. For example, energy bandgap has been reported to vary between 1.11 eV and 1.12eV and therefore it is implemented in the variability design with a relatively small screening percentage [48]. Afterwards, the screening model was imported in TCAD



software and was simulated [117]. Analysis of the screening model provided a Pareto graph, as shown in Figure 7.6. [107]. It indicates the relative importance of the impact of each parameter on the SR (at 320 K and 340 K, and at 500 nm and 900 nm) and the dark current (at 340 K and 1.25 V). Minority carrier lifetime, mobility and auger parameter variability have the highest impact on the SR characteristics. Furthermore, the energy bandgap and the minority carrier variations have the highest impact on the dark current. Since the change in the energy bandgap is highly unlikely, the variation range was taken as only +/- 1.5 % [107].

**Table 7.2.** Screening of all input parameters according to the parameter groups mentioned in Table 7.1. [107].

Screening percentage			
<i>Energy bandgap</i>	<i>Doping dependent mobility of electrons</i>	<i>SRH recombination</i>	<i>Auger recombination</i>
+/- 1.50%	+/- 20%	+/- 5000%	+/- 20%

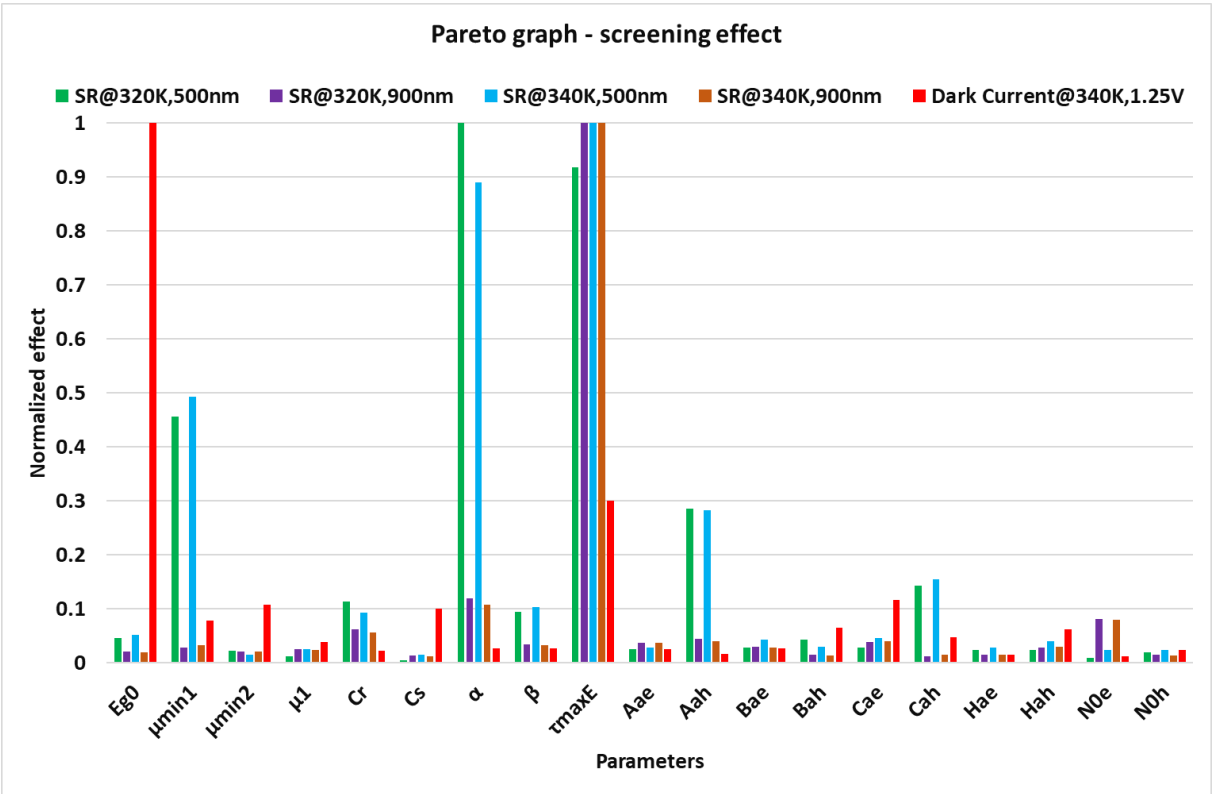


**Figure 7.6.** Pareto graph indicating the relative importance of the impact of each parameter on the spectral responsivity (SR) (at 320 K and 340 K, and at 500 nm and 900 nm) and the dark current (at 340 K and 1.25 V). It can be observed that for spectral responsivity, the largest effect comes from the lifetime, mobility and auger parameter variability, and for the dark current, the largest impact has the energy bandgap variation as well as the lifetime variations [107].

Following the screening analysis, the parameters with the highest impact are selected and implemented in the DoE. In the case of SR characteristics,  $\tau_{maxE}$ ,  $\alpha$ ,  $\mu_{min1}$ ,  $A_{AH}$ ,  $C_r$  and  $N_{OE}$  parameters were selected as the most important parameters. The most impacting parameters on the dark current were  $E_{g0}$  and  $\tau_{maxE}$ . The other parameters are neglected as they have a considerably smaller effect, below a statistical threshold determined for each response studied.

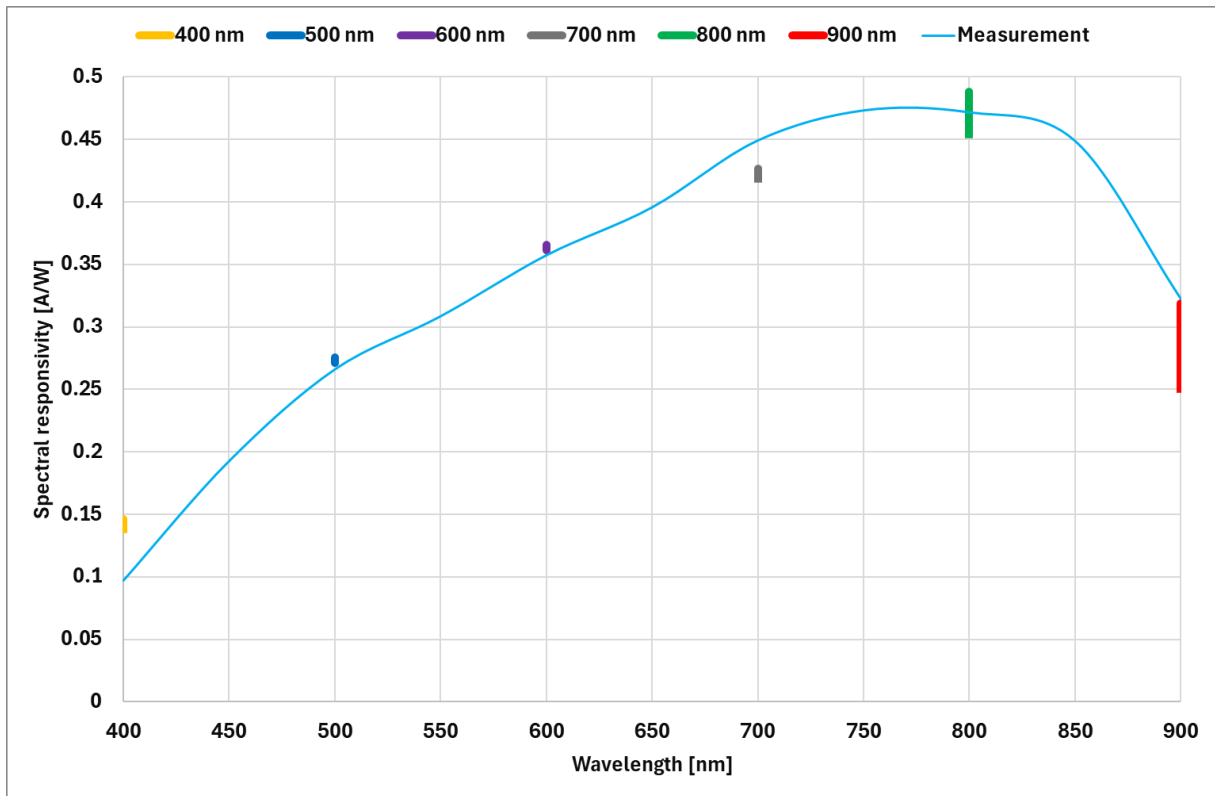
According to a face-centered central composite full design, a RSM was designed by considering the initial values of the selected parameters in the screening step and their variability range. Face-centered distribution means that the parameters were varied by a percentage around the initial value. The RSM gives information on how the observed responses behave according to a quadratic function of the most impacting parameters. The sensitivity analysis of each parameter is obtained by RSM techniques that deliver the variability of each response according to the variation of the input parameters within their range. After the sensitivity analysis, calibrated parameter values that achieve the best fitting of spectral responsivity have been extracted and are shown in Table 7.3. [107].

An example, showing the variability of the simulated SR as a function of the variability of  $\tau_{maxE}$ , at 340 K, in comparison with the normalized measurement, is depicted in Figure 7.7. [107]. The measurement was normalized to one island, by dividing the measured values by the total number of NW islands. The columns at discrete wavelengths which are multiples of 100 nm represent the simulated SR at that wavelength for different minority carrier lifetime values. The tip of each of the columns indicates longer lifetime, hence higher SR. Minority carrier lifetime has the highest impact in the longer wavelength range (800 nm – 900 nm), as it affects the recombination rate. For lower lifetime, the recombination rate increases, reducing the diffusion length and leading to the degradation in SR. Figure 7.8. shows the comparison between the initial and calibrated simulations with the measurements. The simulated SR characteristics are the same up to 800 nm, and from 800 nm to 900 nm the improvement of 10% is seen on the calibrated curve [107]. Even though the simulation domain was quite simplified (only one-island structure), the mismatch between the measurement and the calibrated simulation is relatively small. The sensitivity analysis of RSM for the dark current is shown in Figure 7.9. [107]. It can be noted that the calibrated curves match the measured curve quite accurately [107].

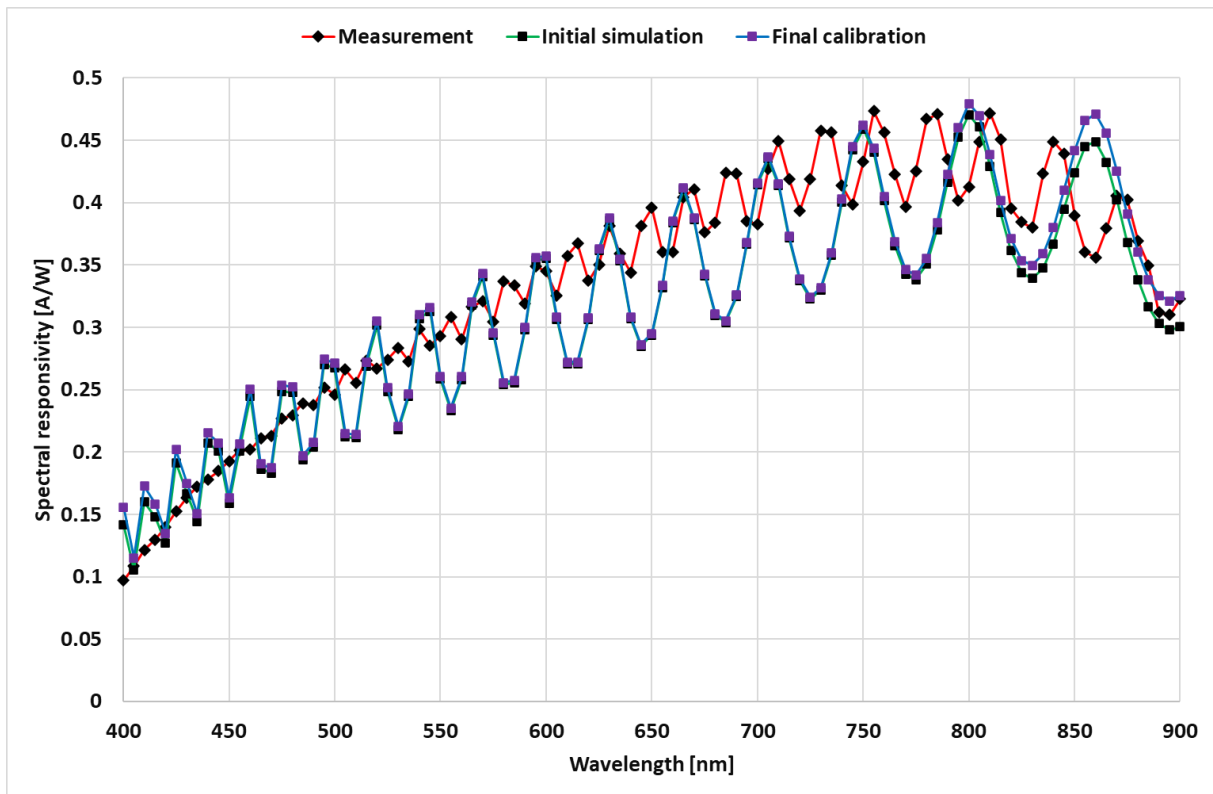
**Table 7.3.** Calibrated parameter values for spectral responsivity (SR) simulation [107].

<i>Parameter</i>	<i>Initial value</i>	<i>Calibrated value</i>
$\mu_{min1}$	52.2 cm <sup>2</sup> /Vs	62.64 cm <sup>2</sup> /Vs

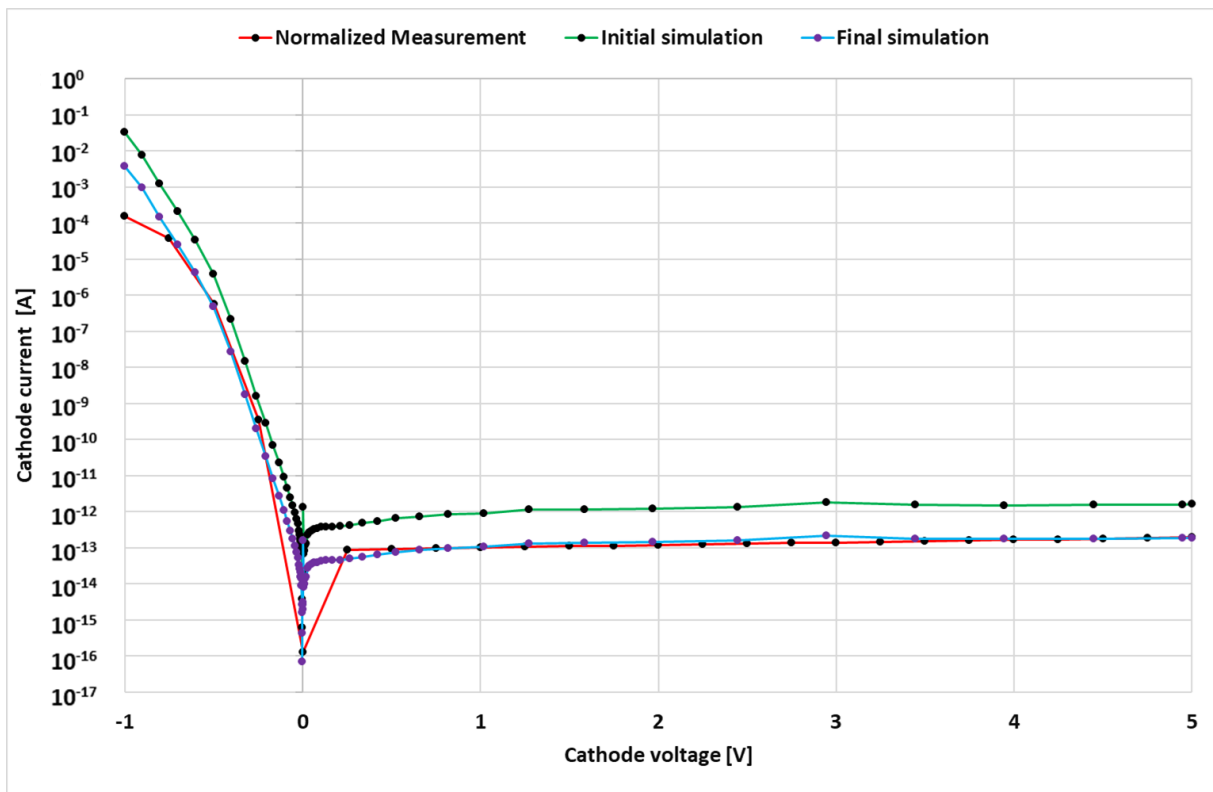
$C_r$	$9.68 \cdot 10^{16} \text{ cm}^{-3}$	$11.6 \cdot 10^{16} \text{ cm}^{-3}$
$\alpha$	0.68	0.544
$\tau_{maxE}$	0.001 s	0.05 s
$A_{AH}$	$7.2 \cdot 10^{-32} \text{ cm}^6 \text{ s}^{-1}$	$5.76 \cdot 10^{-32} \text{ cm}^6 \text{ s}^{-1}$
$N_{0E}$	$10^{18} \text{ cm}^{-3}$	$0.8 \cdot 10^{18} \text{ cm}^{-3}$



**Figure 7.7.** Variation of spectral responsivity (SR), at 340 K, as a function of variability of the electron lifetime in the range from 0.001 s to 0.05 s. The columns at discrete wavelengths which are multiples of 100 nm represent the simulated SR at that wavelength for different minority carrier lifetime values. The tip of each of the columns indicates longer lifetime, hence higher SR. Minority carrier lifetime has the highest impact in the longer wavelength spectrum region (800 nm – 900 nm), as it affects recombination rate and for lower lifetime, recombination increases, reducing the diffusion length and leading to the degradation in SR [107].



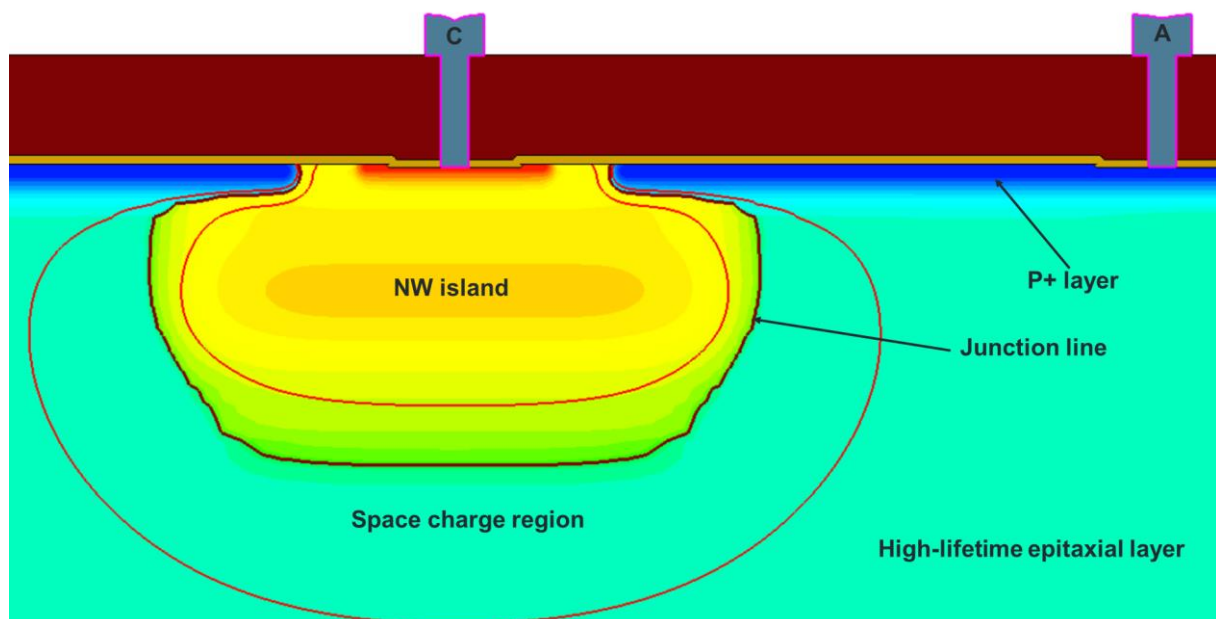
**Figure 7.8.** Comparison of the calibrated and non-calibrated spectral responsivity (SR) curves with the measurements of the photodiode structure fabricated in *ams OSRAM* 350 nm CMOS technology. The calibrated curve shows improvements of 10% at longer wavelength range (800 nm – 900 nm) compared to the non-calibrated curve. The small mismatch between the calibrated simulations and the measurements is present due to the simplified simulation domain, which only included one N-Well (NW) island [107].



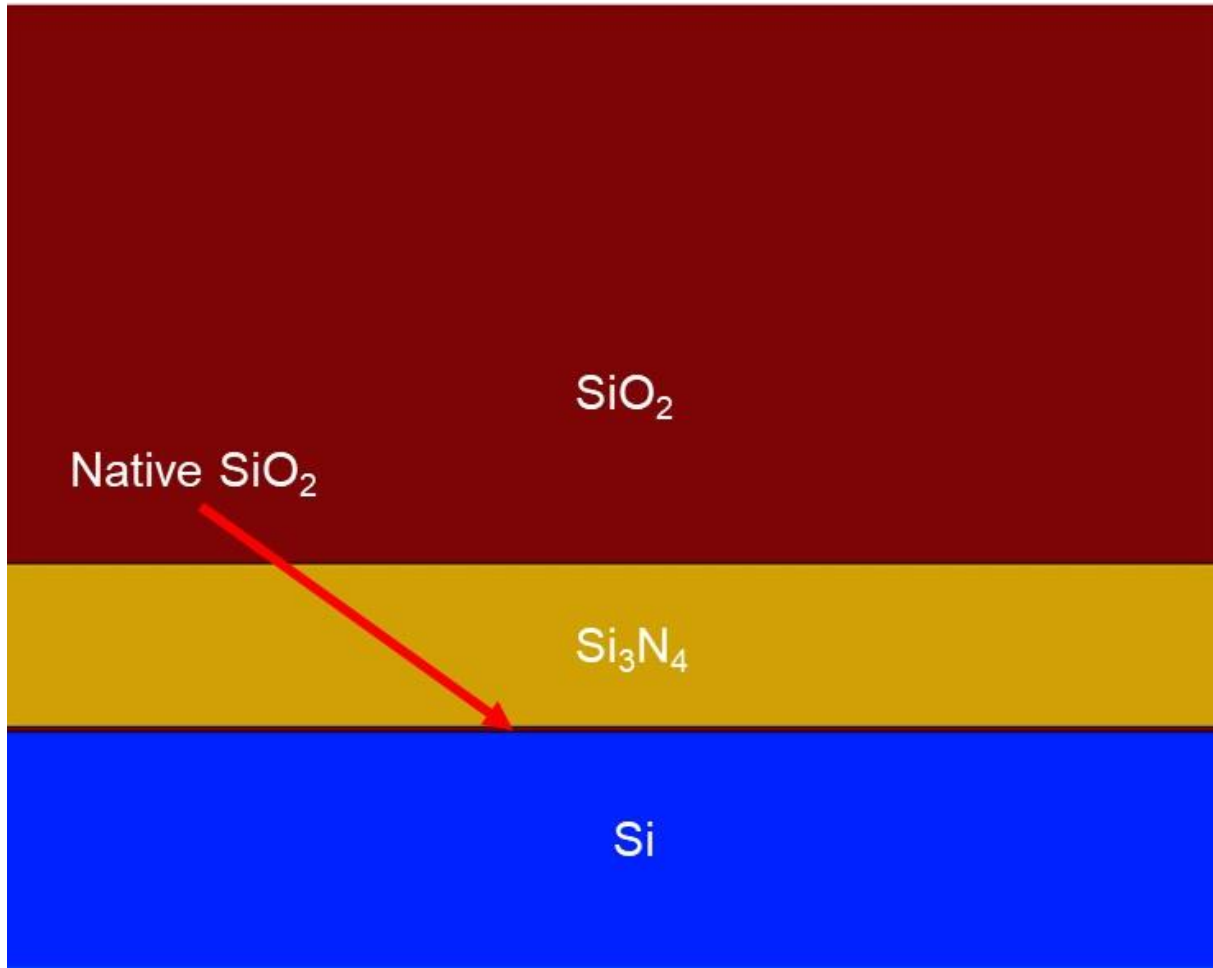
**Figure 7.9.** Comparison between the initial, calibrated simulation and the normalized dark current measurements at 340 K. The normalized measurement curve indicates that the measurement was normalized to one N-Well (NW) island, by dividing the measured values by the total number of NW islands. Good calibration is achieved between the final TCAD simulation and the normalized measurements [107].

#### 7.4. Photodiode structure simulation in *ams OSRAM 180 nm CMOS* technology and pre-irradiation electrical characteristics measurement fitting

Following the same approach regarding simulation domains, the reverse I-V characteristics in 180 nm technology is also modeled by one-island structure and then normalized to the total number of NW islands in order to achieve appropriate dark current simulation fitting with the measurements. The cross-section of the aforementioned one-island structure simulation is shown in Figure 7.10. [102]. It consists of one NW, which is surrounded by the highly-doped p-type layer, which is used to passivate the surface. The parameter determining the minority carrier lifetime was modified to  $\tau = 1\text{ms}$  in SRH generation/recombination model. Cathode and anode contacts are named “C” and “A” respectively. The junction line is represented by the dark brown line. Furthermore, the operating voltage was set at 1.25V reverse bias and the resulting space charge region is the area between the two red lines. The dielectric stack, that was placed on top of the photodiode surface, consists of different insulating layers, i.e. the native silicon oxide, the silicon nitride, and an additional ILD silicon oxide, which is shown in Figure 7.11. [102].

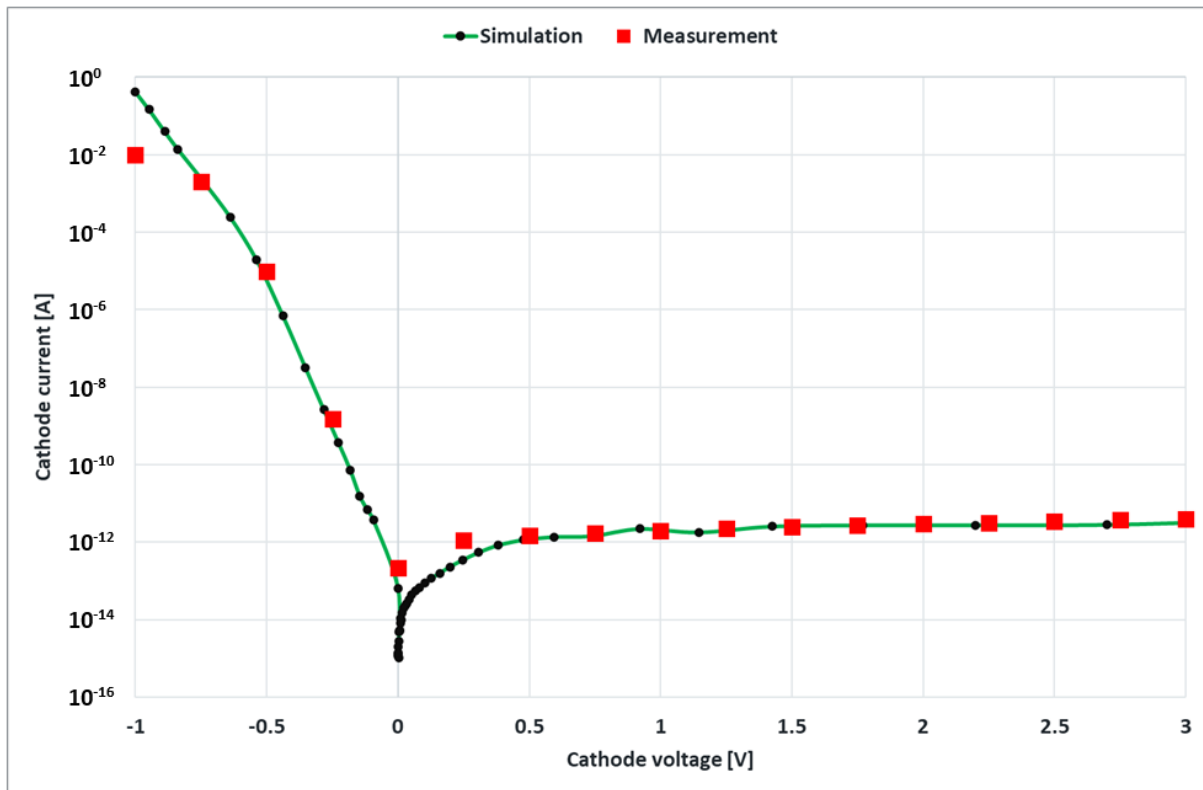


**Figure 7.10.** Simulated photodiode structure, which consists of one N-Well (NW) island, passivating highly-doped p-type layer and high-lifetime epitaxial layer. Highlighted space charge region (SCR), the area between the two red lines, is given for 1.25V reverse bias condition. Cathode and anode contacts are named “C” and “A” respectively [102].



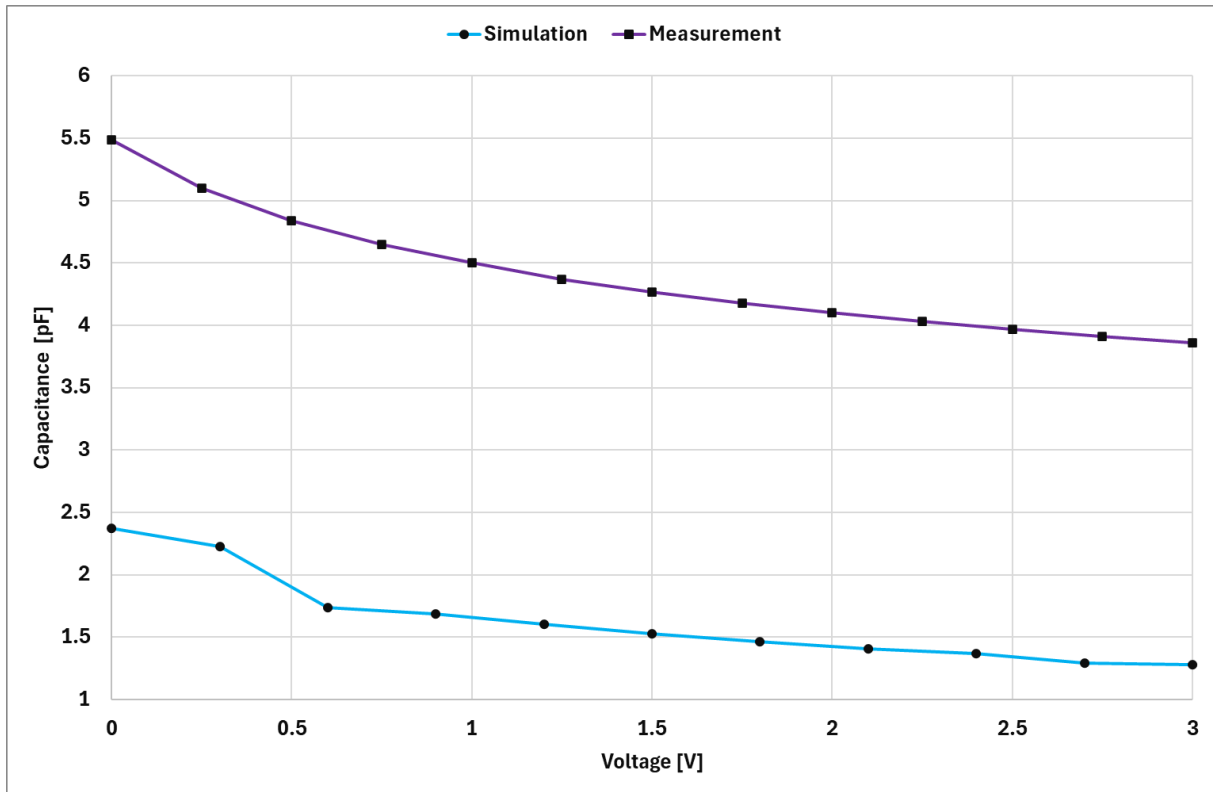
**Figure 7.11.** Dielectric stack composition above the photodiode surface. Dielectric stack consists of a native silicon oxide, a silicon nitride layer, and an inter level dielectric (ILD) silicon oxide [102].

Figure 7.12. shows calibrated pre-irradiation I-V simulations with the measured characteristics [102]. The simulation was normalized to 242 islands. As mentioned in chapter 7.1., the forward bias characteristics was calibrated using multiple island structure, in order to take the island periphery into account as well. Furthermore, in order to convert a 2D rectangular simulation domain into a 3D circular island perimeter, a numerical area factor of 3.42 was applied. Small deviation between measurement and simulation can be observed in the high-current region of the forward characteristics. In the simulation, not all 242 islands were taken into account and the contact resistance and metal lines resistance were not modeled in the simulations, which resulted in a slightly higher forward current [102].



**Figure 7.12.** Comparison between pre-irradiation current-voltage (I-V) simulation and measurement. Simulation was normalized to 242 islands. A numerical area factor of 3.42 was applied to the rectangular 2D simulation domain in order to convert it into a 3D circular island perimeter. Desired fitting is achieved for the majority of the characteristics. A minor deviation is observed in the high-current region of the forward characteristics, due to a different contact and metal lines resistance [102].

Comparison between the pre-irradiation C-V simulations and measurements is shown in Figure 7.13. As in the I-V simulations, the C-V simulations were normalized to 242 islands and to the circular shape of the islands. After the normalization, a difference in the order of  $\sim 2.7$  times can be noted. The mismatch is present, because in the simulations, the parasitic capacitance, coming from the metallization and ILDs were not included.



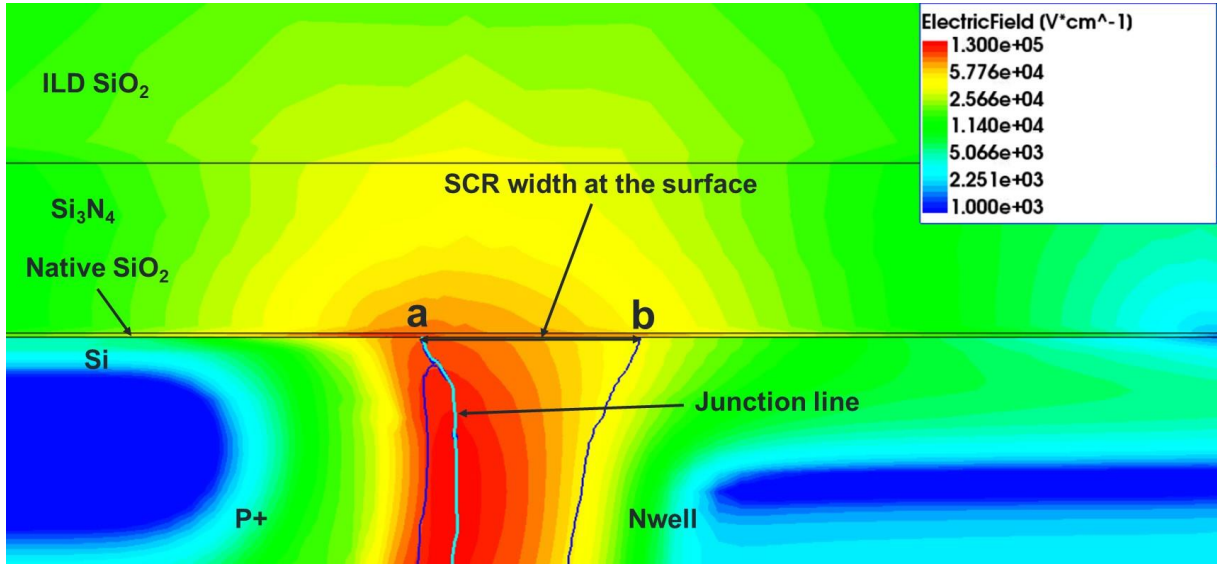
**Figure 7.13.** Comparison between the pre-irradiation capacitance-voltage (C-V) simulations and measurements. As in the current-voltage (I-V) simulations, the C-V simulations were normalized to 242 islands and to the circular shape of the islands. After the normalization, a difference in the order of  $\sim 2.7$  times can be noted. The mismatch is present, because in the simulations, the parasitic capacitance coming from the metallization and inter level dielectric (ILD), was not included.

## 7.5. Implementation of TID induced defects in TCAD environment

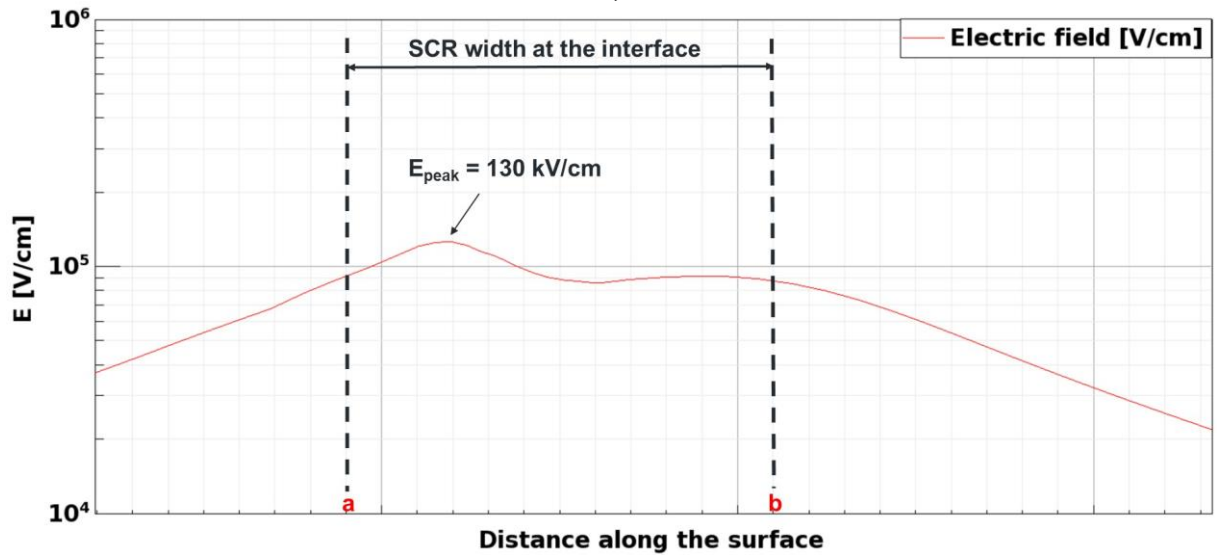
Implementation of TID induced defects in TCAD environment included fixed charges and interface traps modeling.

The fixed charges, present in the insulating layers, i.e. the silicon nitride and the silicon oxide, are a function of the hole yield ( $Y(E)$ ) and total radiation dose ( $D$ ), ( $Q_{f\_oxide} \sim f(Y(E), D)$ ). The density of fixed charges in the native oxide was calculated by performing unbiased (both cathode and anode contacts were grounded) electrical simulation at the irradiation temperature ( $T = 21\text{ }^{\circ}\text{C}$ ). The electric field distribution, as well as its peak field value in the native oxide region was extracted from such simulations, as shown in Figures 7.14. a) and b) [102].





a)



b)

**Figure 7.14.** Electric field distribution **a)** in the photodiode region where the space charge region (SCR) reaches the photodiode surface and **b)** in the native oxide region, along the interface with silicon. Simulation was performed at 0 V bias and at  $T_{Xray} = 21$  °C. Points a and b indicate the edges of the SCR that reaches the photodiode surface. The peak electric field value in the native oxide is located where the SCR reaches the photodiode surface [102].

From the peak electric field value, which equals 130kV/cm, the hole yield, which defines the fraction of unrecombined holes in the oxide, was calculated:

$$Y(E) = \left( \frac{|E| + E_0}{|E| + E_1} \right)^m, \quad (7.6)$$

where  $E$  is the electric field in the native oxide layer,  $E_0 = 0.1$  V/cm,  $E_1 = 0.55$  MV/cm and  $m = 0.9$  for X-ray irradiation. Finally, similar to equation (2.1), fixed charges were calculated according to the TCAD TID model:

$$N_{ot} = g_0 \cdot D \cdot Y(E), \quad (7.7)$$

where  $g_0 = 7.88 \cdot 10^{12} \text{ rad}^{-1} \text{cm}^{-3}$  is the pair generation rate and  $D$  is the total absorbed dose in rad [118, 119]. In addition to fixed charges in the native oxide ( $N_{ot} = 5.35 \cdot 10^{16} \text{ cm}^{-3}$  at the peak electric field  $E = 130 \text{ kV/cm}$ ), positive fixed charges in the silicon nitride layer were added [120, 121]. Fixed charges in the nitride layer are present because of the silicon nitride deposition procedure, and also partially due to X-ray irradiation [122]. After X-ray irradiation, electron-hole pairs are generated in the nitride layer, where holes have a trapping probability 10 times higher than electrons, and are mostly trapped near the interface with the oxide layers surrounding the nitride, as shown in [123, 124]. Positive charges in the nitride were included only in the post-irradiation simulation, in order to simulate their interaction with the radiation-induced defects [102].

Since the bias was not controlled during X-ray irradiation experiments, due to floating photodiode electrodes on the wafer, the radiation-induced photocurrent results in charge build-up at neutral n- and p-sides and the small forward bias of the photodiode. However, the pn-junction's knee voltage limits the forward bias build-up to open-circuit voltage, i.e. 0.5 – 0.7V. Because of that, the peak electric field value was slightly lower ( $E = 60 \text{ kV/cm}$ ) compared to the simulated electric field, meaning that presented simulation results at zero bias represent the worst-case scenario in the given irradiation conditions. Considering that, the actual hole yield with forward biased photodiode would be lower than the hole yield that was extracted from the simulations. Nevertheless, in both cases the electric fields are quite low, and the differences are expected to be negligible [46, 56].

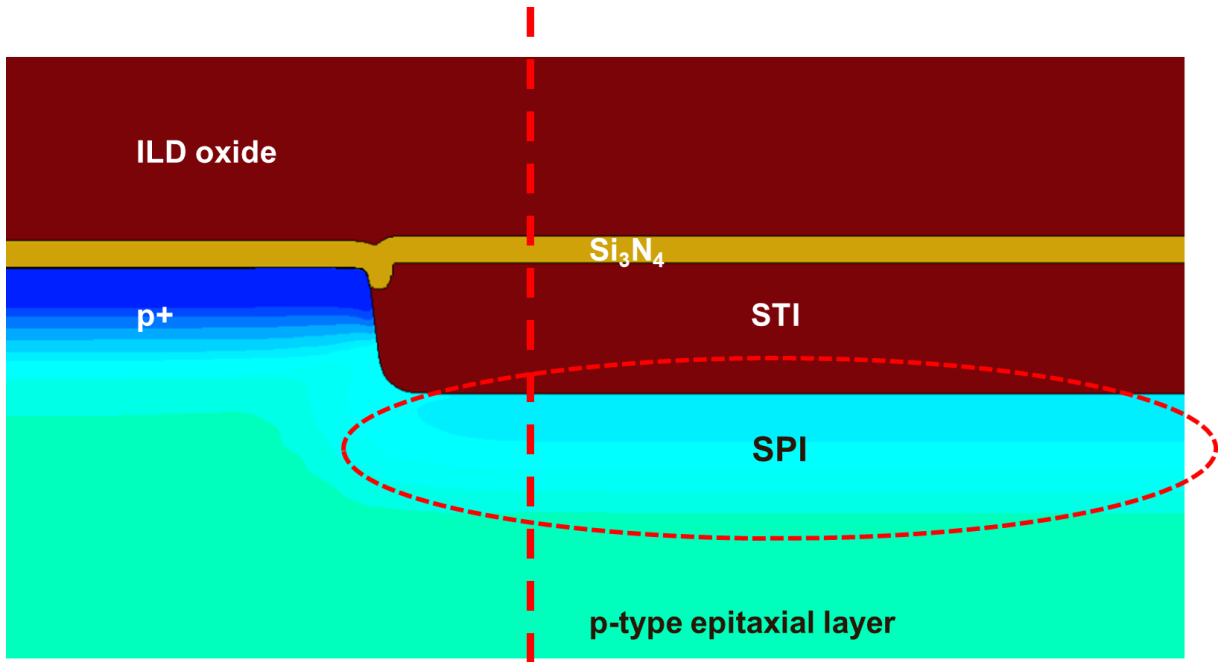
The model additionally calculates interface traps density at the silicon/silicon oxide interface. The interface trap density,  $N_{it} \sim f(D, \alpha, \beta)$ , is a function of the total irradiation dose,  $D$ , and two additional parameters,  $\alpha$  and  $\beta$ , which are defined for nMOS or pMOS structures. Since the relevant region of the photodiode is the junction of highly-doped p-type layer with the NW island, the  $N_{it}$  was calculated using the TID model for the pMOS. Additionally, according to [125], two acceptor levels and one donor trap level were added around the midgap energy. Finally, capture cross-section values for electrons and holes were selected and were kept the same for said acceptor and donor traps. The interface trap parameters, with their initial values, are given in Table 7.4. [102]. The trap density distribution for acceptor traps was distributed 40% of the total interface trap density to first acceptor trap and 60% to the second acceptor trap [125].

**Table 7.4.** Initial defect parameters implemented in TCAD simulations. These parameters include density of fixed charges in the silicon oxide and silicon nitride, respectively. Additionally, interface traps include trap densities, energy levels and electron and hole capture cross sections for the donor and two acceptor type interface traps [102].

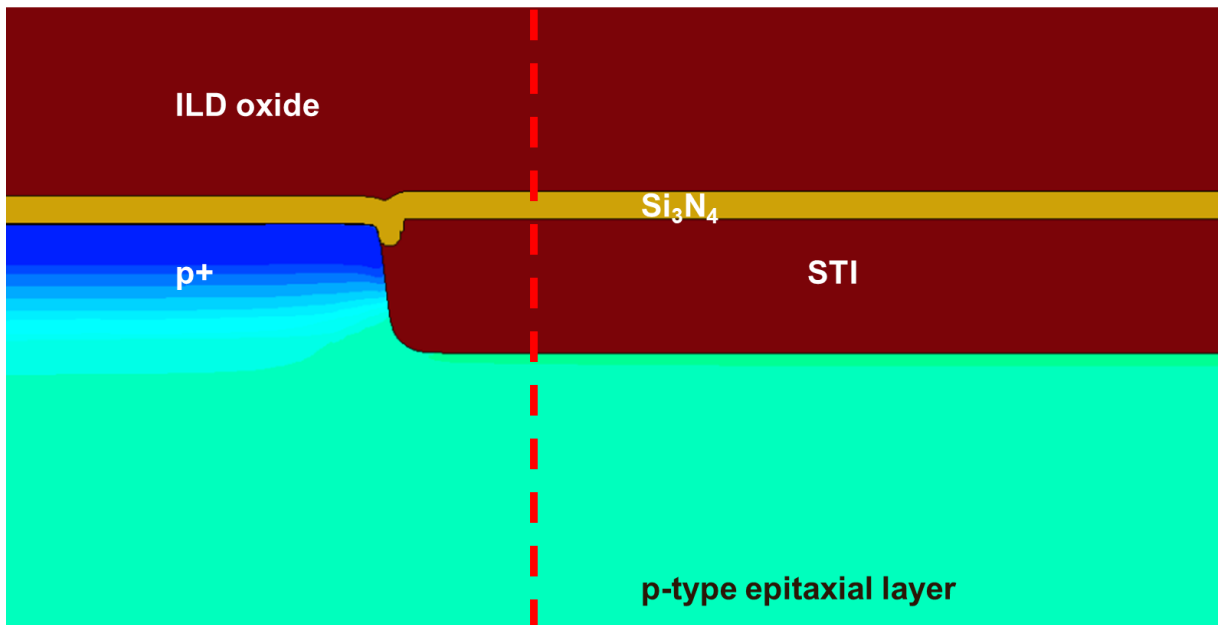
Symbol	Quantity	Initial value
$Q_{f\_oxide}$	Fixed charges in the native oxide	$8 \cdot 10^9 \text{ [cm}^{-2}\text{]}$
$Q_{f\_nitride}$	Fixed charges in the silicon nitride	$2.5 \cdot 10^{11} \text{ [cm}^{-2}\text{]}$
$N_{it}$	Total interface trap density	$3.2 \cdot 10^{11} \text{ [cm}^{-2}\text{]}$
$E_D$	Donor energy level	0.4 [eV]
$N_D$	Donor trap density	$3.2 \cdot 10^{11} \text{ [cm}^{-2}\text{]}$
$E_{A1}$	First acceptor energy level	0.72 [eV]
$N_{A1}$	First acceptor trap density	$1.28 \cdot 10^{11} \text{ [cm}^{-2}\text{]}$
$E_{A2}$	Second acceptor energy level	0.52 [eV]
$N_{A2}$	Second acceptor trap density	$1.92 \cdot 10^{11} \text{ [cm}^{-2}\text{]}$
$\sigma_E$	Electron capture cross-section	$1 \cdot 10^{-16} \text{ [cm}^2\text{]}$
$\sigma_H$	Hole capture cross-section	$1 \cdot 10^{-16} \text{ [cm}^2\text{]}$

## 7.6. Impact of the SPI on the STI/Si interface

Another important photodiode region to consider and discuss is the interface between the STI and the silicon. As mentioned before, the STI impacts the initial dark current, before irradiation, and SR before and after irradiation. Cross-sections of that region, with and without the SPI are depicted in Figure 7.15. a) and b) respectively. The vertical red dashed line indicates the cut-line at which the doping profile was extracted. Figure 7.15. c) shows the doping profile distribution versus depth, indicating a difference of more than two orders of magnitude between the SPI and the epitaxial layer. Small boron segregation is visible in both cases, more pronounced if the SPI is omitted.



a)



b)

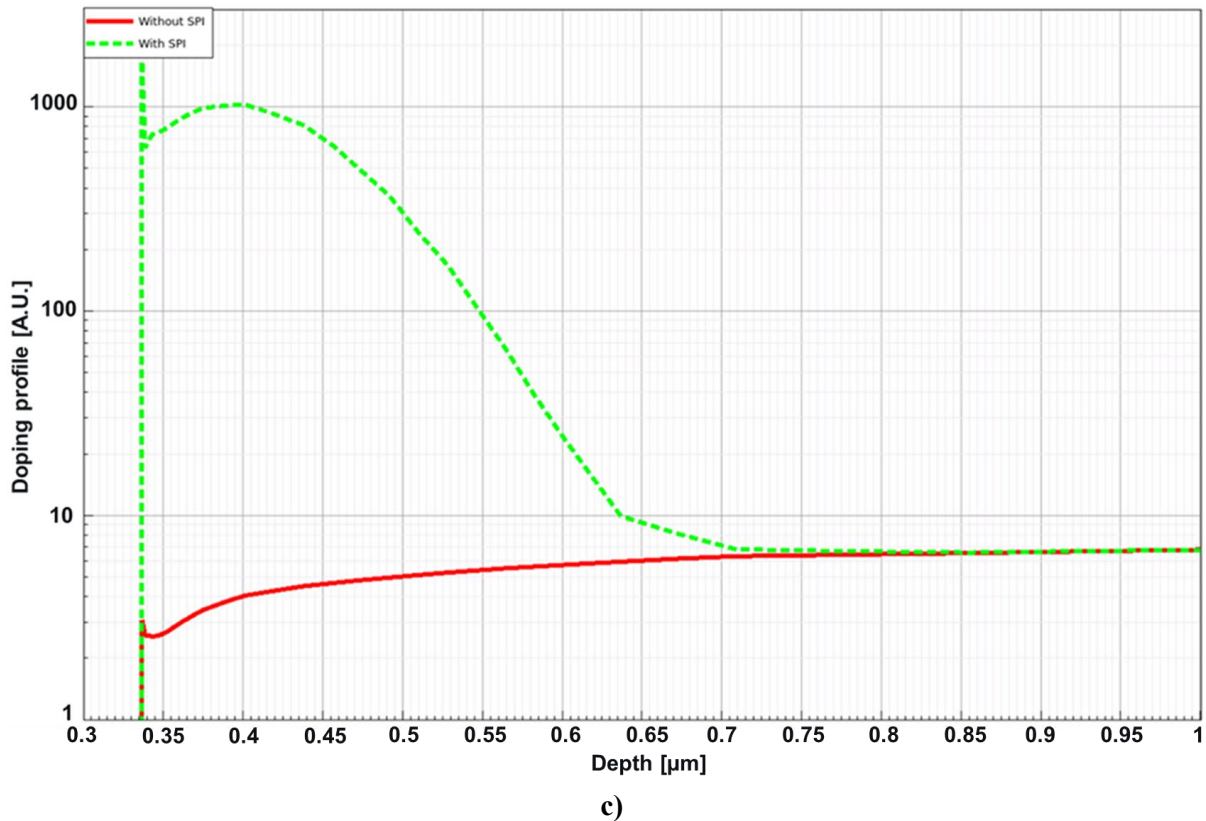


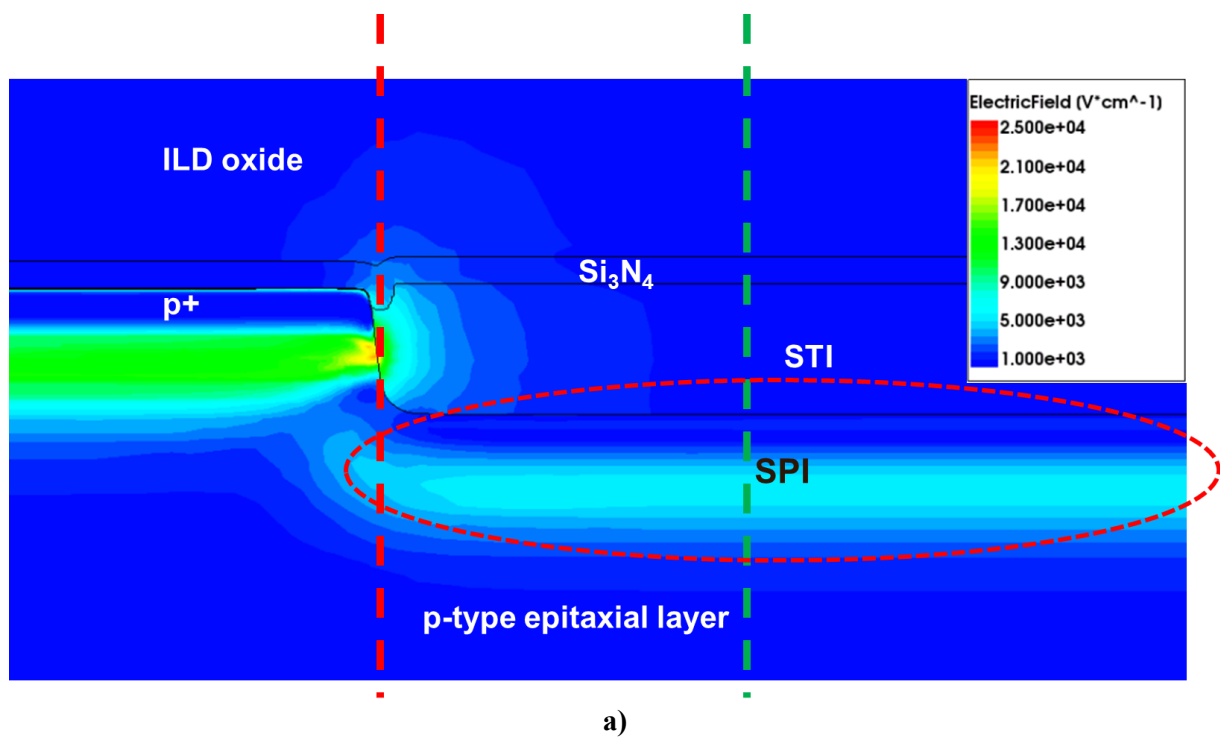
**Figure 7.15.** Cross-section of the interface between the shallow trench isolation (STI) and the silicon: **a)** with shallow p-type implant (SPI) passivation, **b)** without SPI. Doping profile distribution between the two cases are shown in case **c)**. Comparing the two doping profiles, a difference of more than two orders of magnitude between the SPI and the epitaxial layer is observed. Small boron segregation is visible in both cases, more pronounced if the SPI is omitted. The doping profile is expressed in arbitrary units (A.U.) for relative comparison.

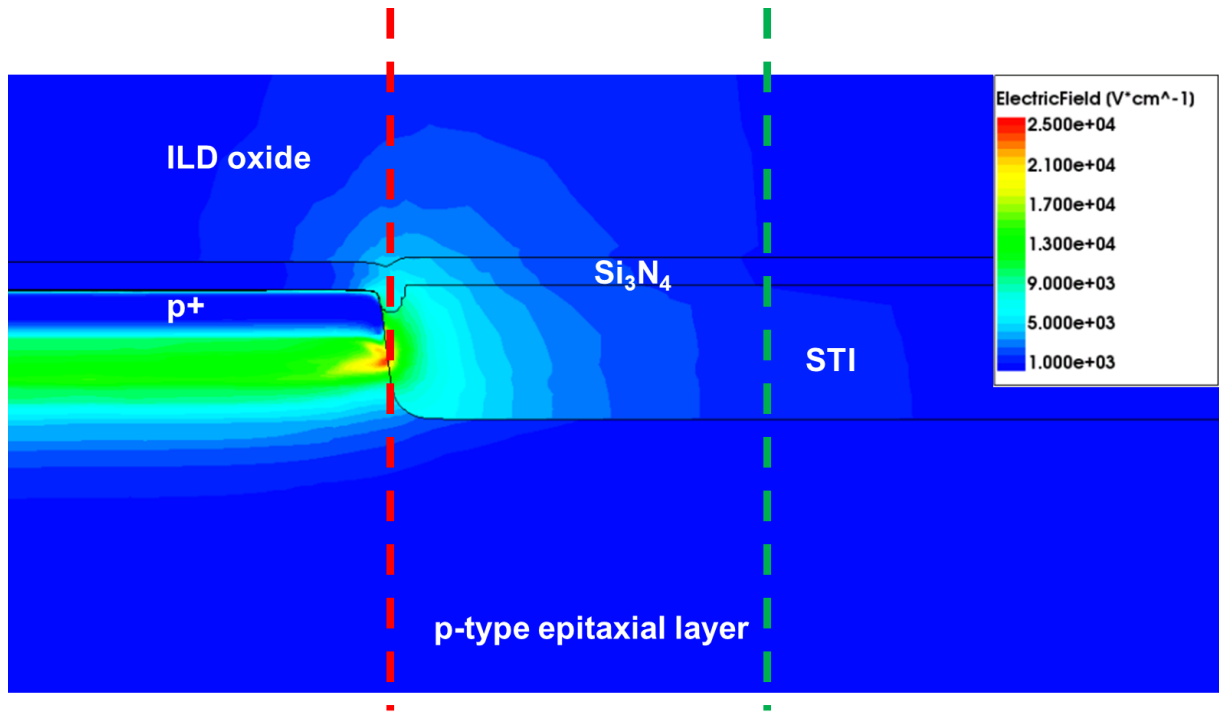
In order to analyze the impact of the SPI on the radiation hardness of the photodiodes, electric field distribution is plotted for both cases, with and without the SPI, and is shown in Figures 7.16. a) and b) respectively. The bias of the NW islands was set to 0 V bias in order to mimic the unbiased wafer environment during X-ray irradiation. The simulation temperature was set to irradiation temperature,  $T = 21$  °C. The electric field scale was fixed between 1 kV/cm and 25 kV/cm. The peak electric field is located in the region where the highly doped surface p-type implant reaches the STI on its lateral side, indicated by the red dashed line. The green dashed line indicates the region where there is no impact of the lateral implant on the vertical electric field. The electric field distributions are given in Figures 7.16. c) and d) respectively.

The peak electric field value is in the range of  $< 25$  kV/cm for both cases and it is around 7 times lower than the electric field in the island region, where the depletion region reaches the SiO<sub>2</sub>/Si interface. Due to such low electric field value, it is expected that a small amount of radiation-induced defects is generated in the STI and at the STI/Si interface. Because of that, a small degradation of optical performance is observed, as discussed before, in chapter 5.2.3.

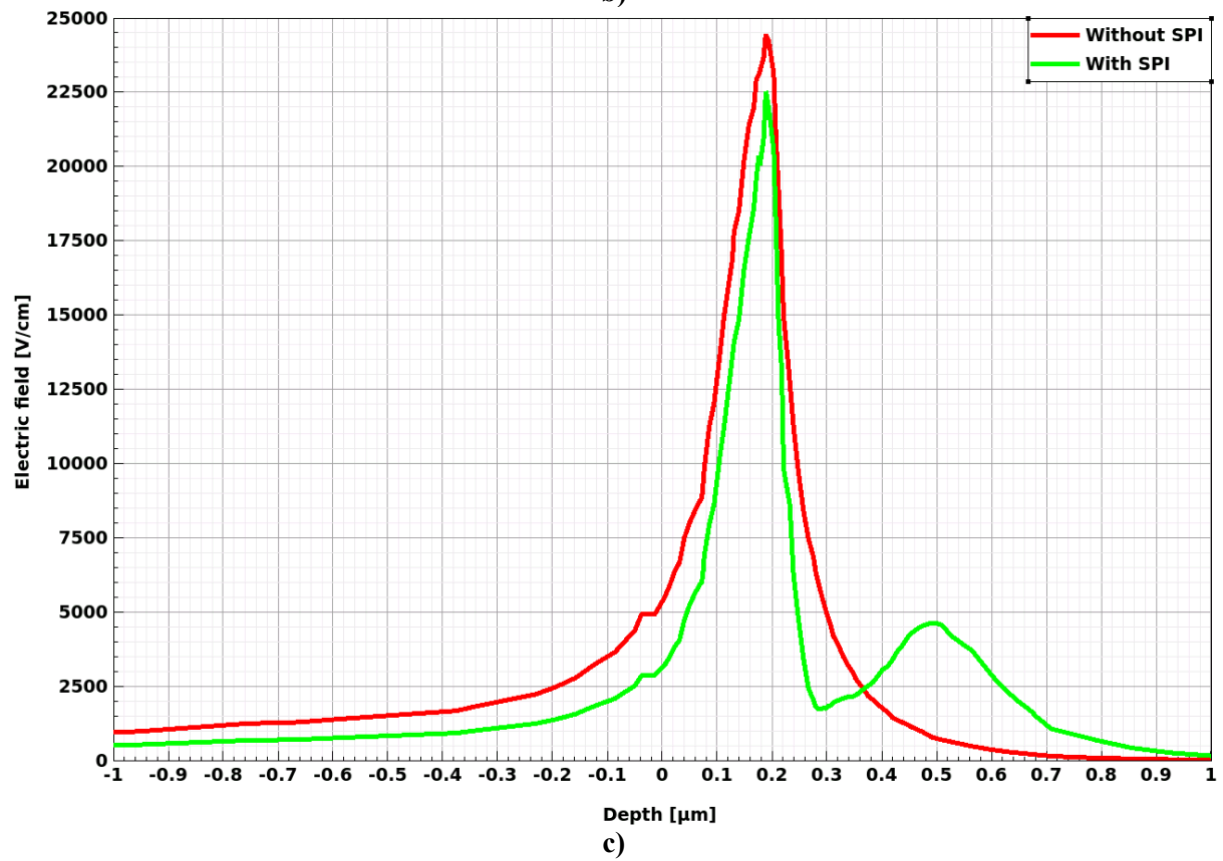
Considering the vertical electric field, it can be concluded that there is negligible depletion at the STI/Si interface if the SPI is omitted. The electric field is in the range of  $< 1$  kV/cm, which is too low to impact defect generation due to X-ray irradiation. On the other hand, if the SPI is present, the electric field strength increases up to 5.5 kV/cm. The electric field is present due to the SPI out-diffusion towards the epitaxial layer. This means that the SPI is acting as a repelling layer, forcing optically generated minority electrons away from the STI/Si interface.

Even though there is no significant electric field present in the STI, if the SPI is omitted, the STI/Si interface still includes some interface traps, present due to the silicon oxide deposition procedure during STI processing. Because of that, the optical performance, before and after irradiation, will be slightly degraded, resulting in lower SR values. Finally, in order to improve the robustness and radiation-hardness of the photodiode structures at the STI/Si interface, the SPI should be used, as it will passivate the STI/Si interface, preventing the trapping of optically generated minority electrons.





b)



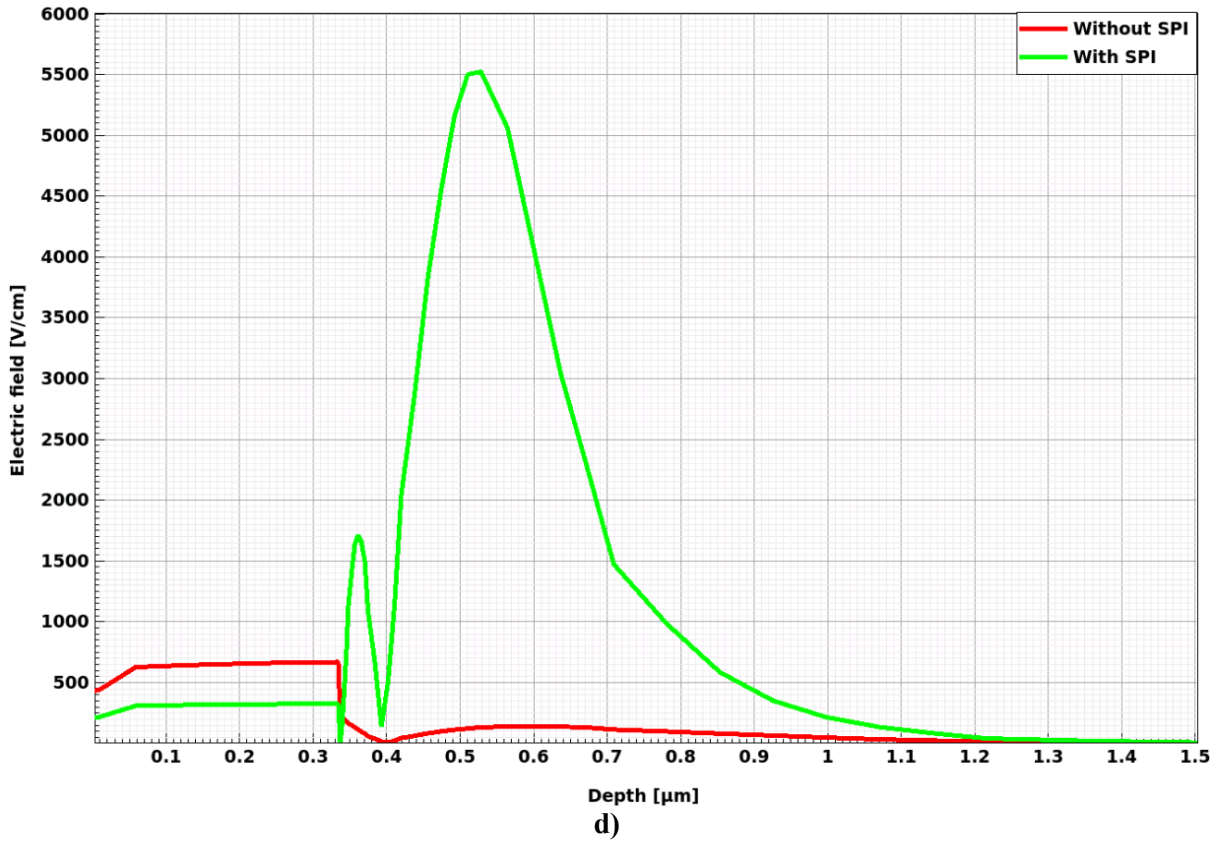


**Figure 7.16.** Electric field distribution at the shallow trench isolation/silicon (STI/Si) interface: **a)** with shallow p-type implant (SPI) passivation, **b)** without SPI passivation. The electric field present in the SPI region is there due to the out-diffusion of the SPI towards the epitaxial layer, causing a gradient in the doping profile. Red dashed line indicates the vertical cut-line at which the peak electric field distribution is extracted, as seen in case **c)**. Case **d)** shows the electric field distribution without the influence of the lateral highly-doped p-type implant on the electric field distribution in the STI.

## 7.7. Modeling and calibration of trap parameters in TCAD simulations

Similar to calibration methodology used in chapter 7.3., a central-composite statistical DoE was implemented [116]. In the DoE, the trap parameters were varied within their physical range with face-centered value distribution, as shown in Table 7.5. [102].

**Table 7.5.** Total-Ionizing Dose (TID) induced defects parameter variation. The trap parameters were varied within their physical range with face-centered value distribution [102].

Symbol	Variation percentage	Minimum value	Maximum value
$Q_{f\_oxide}$	+/- 100%	$4 \cdot 10^9$ [cm <sup>-2</sup> ]	$16 \cdot 10^9$ [cm <sup>-2</sup> ]
$Q_{f\_nitride}$	+/- 100%	$1.25 \cdot 10^{11}$ [cm <sup>-2</sup> ]	$5 \cdot 10^{11}$ [cm <sup>-2</sup> ]
$N_{it}$	+/- 100%	$1.6 \cdot 10^{11}$ [cm <sup>-2</sup> ]	$6.4 \cdot 10^{11}$ [cm <sup>-2</sup> ]
$E_D$	+/- 17.5%	0.33 [eV]	0.47 [eV]
$N_D$	+/- 100%	$1.6 \cdot 10^{11}$ [cm <sup>-2</sup> ]	$6.4 \cdot 10^{11}$ [cm <sup>-2</sup> ]
$E_{A1}$	+/- 17.5%	0.65 [eV]	0.79 [eV]



$N_{A1}$	+/- 100%	$0.64 \cdot 10^{11} \text{ [cm}^{-2}\text{]}$	$2.56 \cdot 10^{11} \text{ [cm}^{-2}\text{]}$
$E_{A2}$	+/- 17.5%	0.45 [eV]	0.59 [eV]
$N_{A2}$	+/- 100%	$0.96 \cdot 10^{11} \text{ [cm}^{-2}\text{]}$	$3.84 \cdot 10^{11} \text{ [cm}^{-2}\text{]}$
$\sigma_E$	+/- 1000%	$1 \cdot 10^{-17} \text{ [cm}^2\text{]}$	$1 \cdot 10^{-15} \text{ [cm}^2\text{]}$
$\sigma_H$	+/- 1000%	$1 \cdot 10^{-17} \text{ [cm}^2\text{]}$	$1 \cdot 10^{-15} \text{ [cm}^2\text{]}$

An example of donor and acceptor energy level variation is depicted in Figure 7.17. [102]. The donor trap energy level was varied between 0.33 eV and 0.47 eV, relative to the valence band. The acceptor traps energy levels were varied between 0.65 eV and 0.79 eV in the case of the first acceptor trap and between 0.45 eV and 0.59 eV in the case of the second acceptor trap, relative to the conduction band. Densities of fixed charges in the oxide and in the nitride, as well as the interface trap density had minimum variation values, whereas the electron and hole capture cross-sections had maximum screening values. Dominant effect on the increase of the dark current comes from the second acceptor level. If the trap energy level of the second acceptor trap is closer to the midgap, the current increases more, as compared to the variation of the energy level of the first acceptor level or the donor level [102].

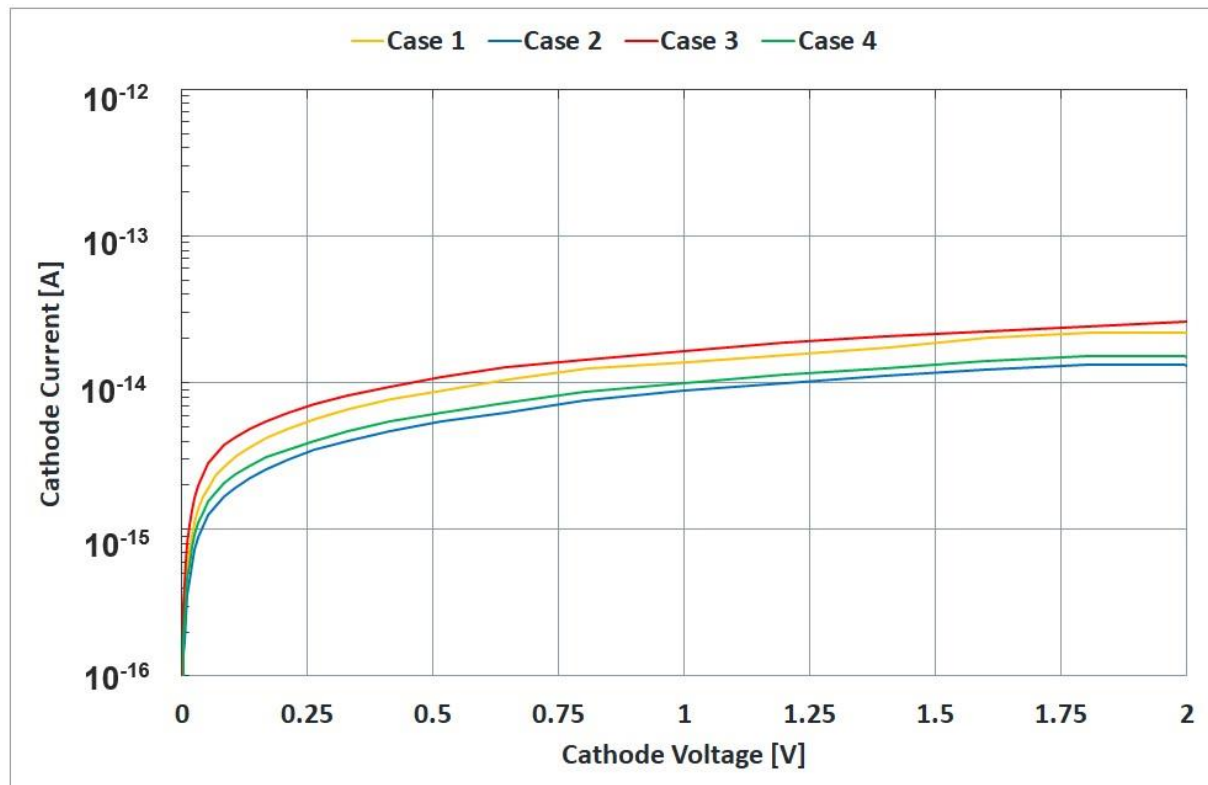


**Figure 7.17.** Reverse current-voltage (I-V) characteristics as a function of the variation of energy level of donor and acceptor traps. The donor trap energy level was varied between 0.33 eV and 0.47 eV, relative to the valence band. The acceptor traps energy levels were varied between 0.65 eV and 0.79 eV in the case of the first acceptor trap and between 0.45 eV and 0.59 eV in the case of the second acceptor

trap, relative to the conduction band. The dominant effect has the variation of the energy level of the second acceptor level. It is positioned closest to the midgap, therefore affecting the dark current significantly more than the other two traps. Fixed charges in the oxide and in the nitride, as well as the interface trap densities had minimum variation values, whereas the capture cross-sections for both electrons and holes had maximum variation values [102].

Table 7.6. presents the calibrated parameter values [102]. Considering that during irradiation, due to the irradiation-generated photo carriers, the photodiode was slightly forward biased, the lower electric field would result in a reduced fixed charge density in the oxide,  $Q_{f\_Oxide,OC} = 5.7 \cdot 10^9 \text{ cm}^{-2}$ , compared to the calibrated value,  $Q_{f\_Oxide} = 8 \cdot 10^9 \text{ cm}^{-2}$ . The resulting dark current where the  $Q_{f\_Oxide,OC}$  value was used instead of the calibrated  $Q_{f\_Oxide}$  value, changed less than 1%, thus the following results and conclusions are based on the calibrated values [102].

**Table 7.6.** Initial and calibrated Total-Ionizing Dose (TID) induced parameter values [102].

Symbol	Initial value	Calibrated value
$Q_{f\_oxide}$	$8 \cdot 10^9 \text{ [cm}^{-2}\text{]}$	$8 \cdot 10^9 \text{ [cm}^{-2}\text{]}$
$Q_{f\_nitride}$	$2.5 \cdot 10^{11} \text{ [cm}^{-2}\text{]}$	$1.25 \cdot 10^{11} \text{ [cm}^{-2}\text{]}$
$N_{it}$	$3.2 \cdot 10^{11} \text{ [cm}^{-2}\text{]}$	$6.4 \cdot 10^{11} \text{ [cm}^{-2}\text{]}$
$E_D$	0.4 [eV]	0.33 [eV]
$N_D$	$3.2 \cdot 10^{11} \text{ [cm}^{-2}\text{]}$	$6.4 \cdot 10^{11} \text{ [cm}^{-2}\text{]}$
$E_{A1}$	0.72 [eV]	0.65 [eV]
$N_{A1}$	$1.28 \cdot 10^{11} \text{ [cm}^{-2}\text{]}$	$2.56 \cdot 10^{11} \text{ [cm}^{-2}\text{]}$
$E_{A2}$	0.52 [eV]	0.59 [eV]
$N_{A2}$	$1.92 \cdot 10^{11} \text{ [cm}^{-2}\text{]}$	$3.84 \cdot 10^{11} \text{ [cm}^{-2}\text{]}$
$\sigma_E$	$1 \cdot 10^{-16} \text{ [cm}^2\text{]}$	$1 \cdot 10^{-15} \text{ [cm}^2\text{]}$
$\sigma_H$	$1 \cdot 10^{-16} \text{ [cm}^2\text{]}$	$1 \cdot 10^{-17} \text{ [cm}^2\text{]}$

## 7.8. TID model in 180 nm technology

The consequence of X-ray irradiation is the accumulation of fixed positive charge in the native oxide and silicon nitride layers and the creation of interface traps, whose mutual interaction defines the surface SCR width. The additional positive charges in the nitride attract the electrons at the NW of the pn-junction and repels the holes at the surface p-type implant. Because of that, the SCR becomes narrower in the n-type region and a bit wider in the p-type

region. The native oxide layer acts as an energy barrier for the electrons attracted by the positive charge in the nitride.

Furthermore, the interface traps are created at the interface of the native oxide with the silicon. These traps could be filled or unfilled, depending on the position of quasi-Fermi levels relative to trap energy levels. The traps were neutral before filling. For acceptor traps, if the quasi-Fermi level for electrons is above the trap energy level, the trap would be filled by an electron. The opposite situation is valid for donor traps. If the interface trap is filled by a charge carrier, then it would act as an added net charge. A filled donor trap would further enhance the effect of the fixed positive charges in the nitride and the filled acceptor trap would have the opposite effect.

Relative energy levels of the electron and hole quasi-Fermi levels with regards to the acceptor and donor traps were extracted from the TCAD simulations. Since the acceptor traps were below the quasi-Fermi level for electrons in the NW region, they were filled by electrons and contributed towards the extension of the SCR at the surface in the NW. Furthermore, donor traps were above the quasi-Fermi level for holes in the p-type region, but because the P<sup>+</sup> doping is ~ three orders of magnitude higher than the doping of NW, the extension of the SCR in the p-type region was negligible. On the other hand, both the acceptor and donor traps acted as generation centers, consequently increasing the surface generation rate. Energy band diagram showing valence and conduction bands, quasi-Fermi levels for both electrons and holes and acceptor and donor trap energy levels along the Si/SiO<sub>2</sub> interface is shown in Figure 7.18. [102].

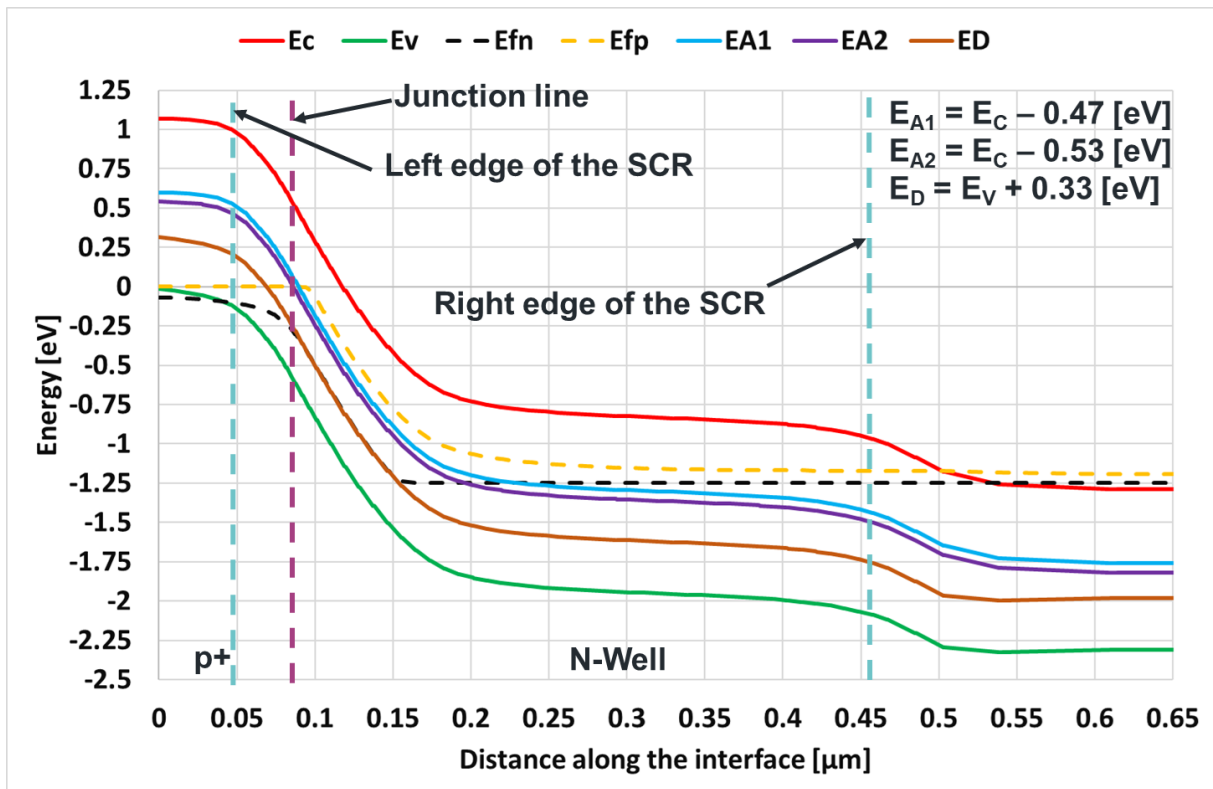
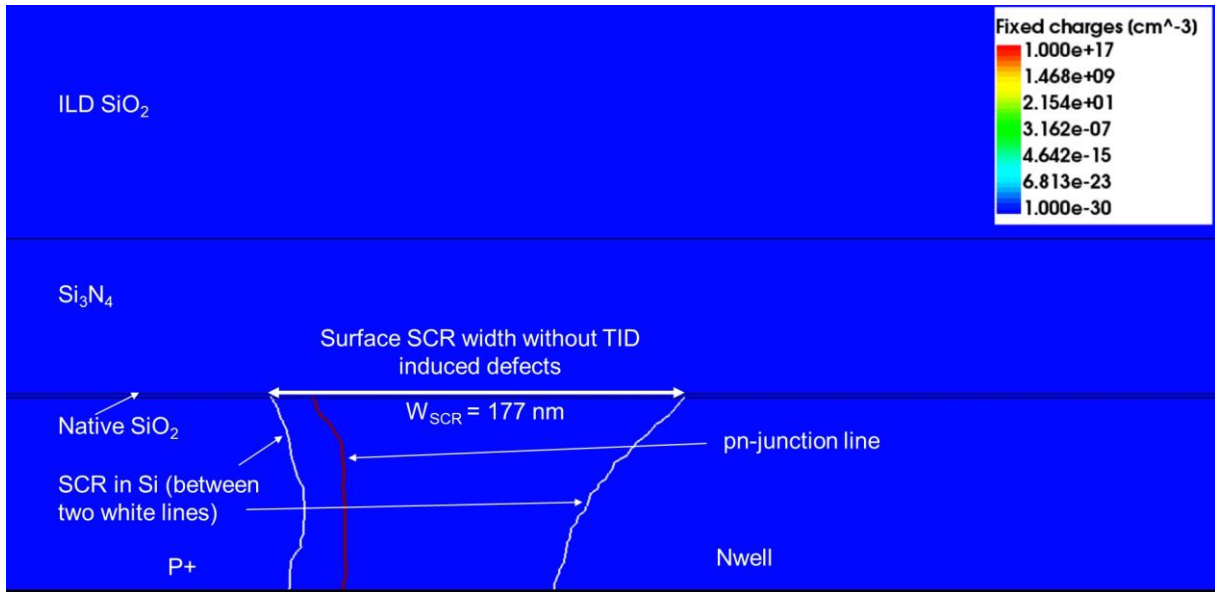
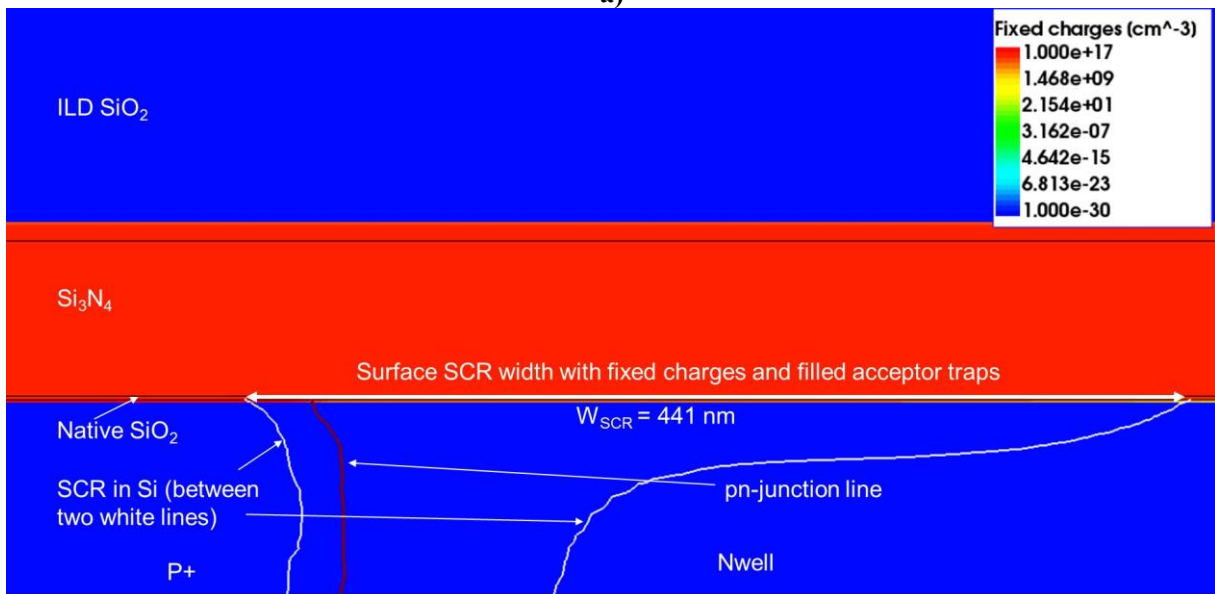


**Figure 7.18.** Energy band diagram along the silicon oxide/silicon ( $\text{SiO}_2/\text{Si}$ ) interface at the  $\text{p}^+/\text{N-Well}$  pn-junction, where  $E_C$  and  $E_V$  are the conduction and valence band energies,  $E_{fn}$  and  $E_{fp}$  are the quasi-Fermi levels for electrons and holes and  $E_{A1}$ ,  $E_{A2}$  and  $E_D$  are the two acceptor and one donor trap energy levels, respectively. Left of the junction line, indicated by the dashed purple line, is the  $\text{p}^+$  region, and right of it is the N-Well. In the majority of the space charge region (SCR) in the n-type region, the acceptor traps are below the  $E_{fn}$ , thus they will be filled by electrons. Similar to them, the donor traps in the SCR in the p-type region are above the  $E_{fp}$ , thus they will be filled by holes [102].

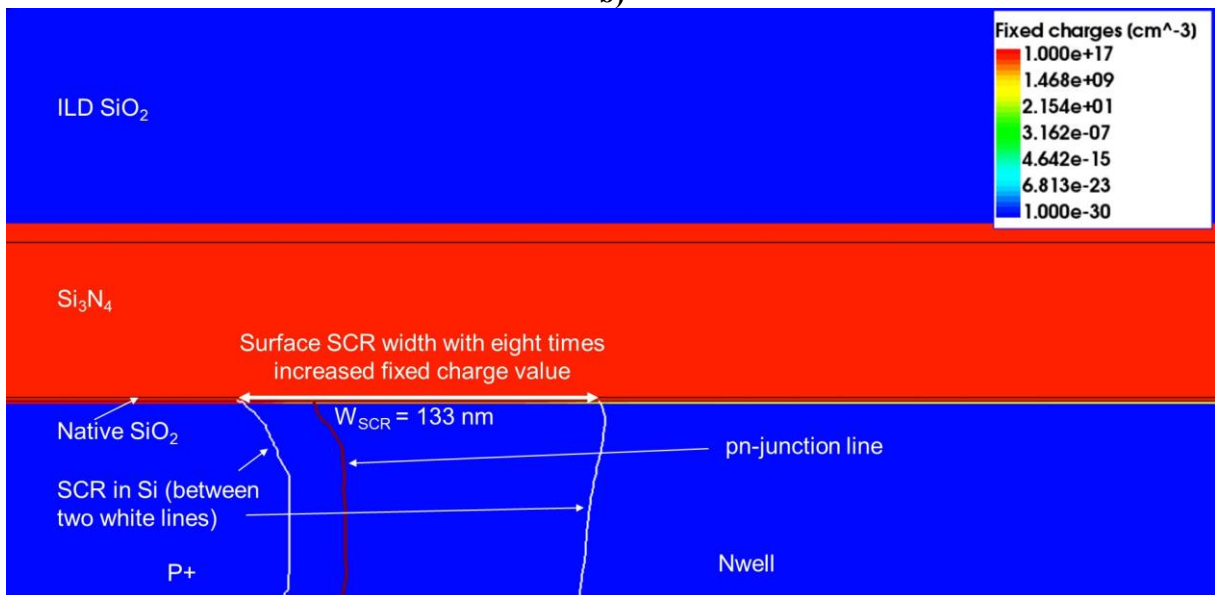
Comparison of SCR width, at 1.25V reverse bias, between the pre-irradiation and post-irradiation simulation at 400 Gy(Si), as well as with the simulation with eight times increased positive charge in the nitride layer, compared to the post-irradiation simulation, is illustrated in Figure 7.19. [102]. SCR width of the 100 Gy(Si) and 200 Gy(Si) simulations was the same as the SCR width of the pre-irradiation simulation, implying that the filled acceptor traps are compensated by the fixed charge in the insulating layers [102].



a)



b)

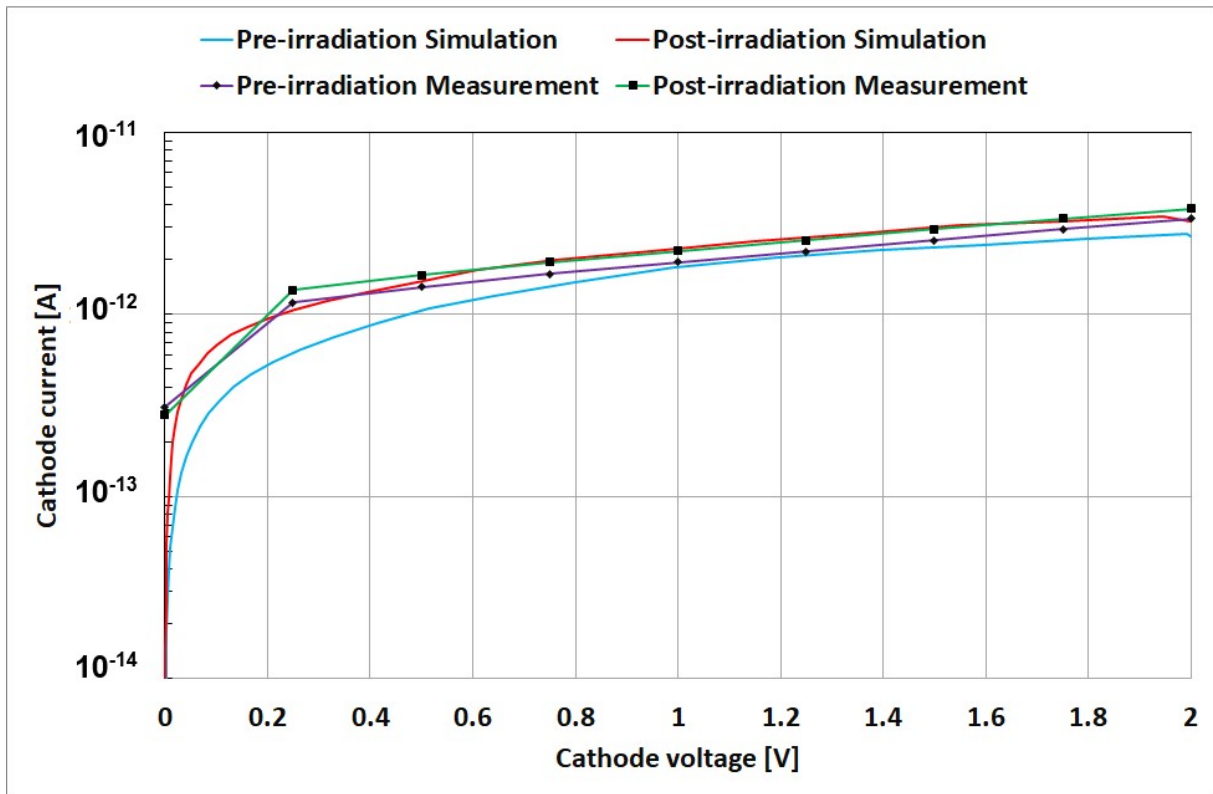


c)

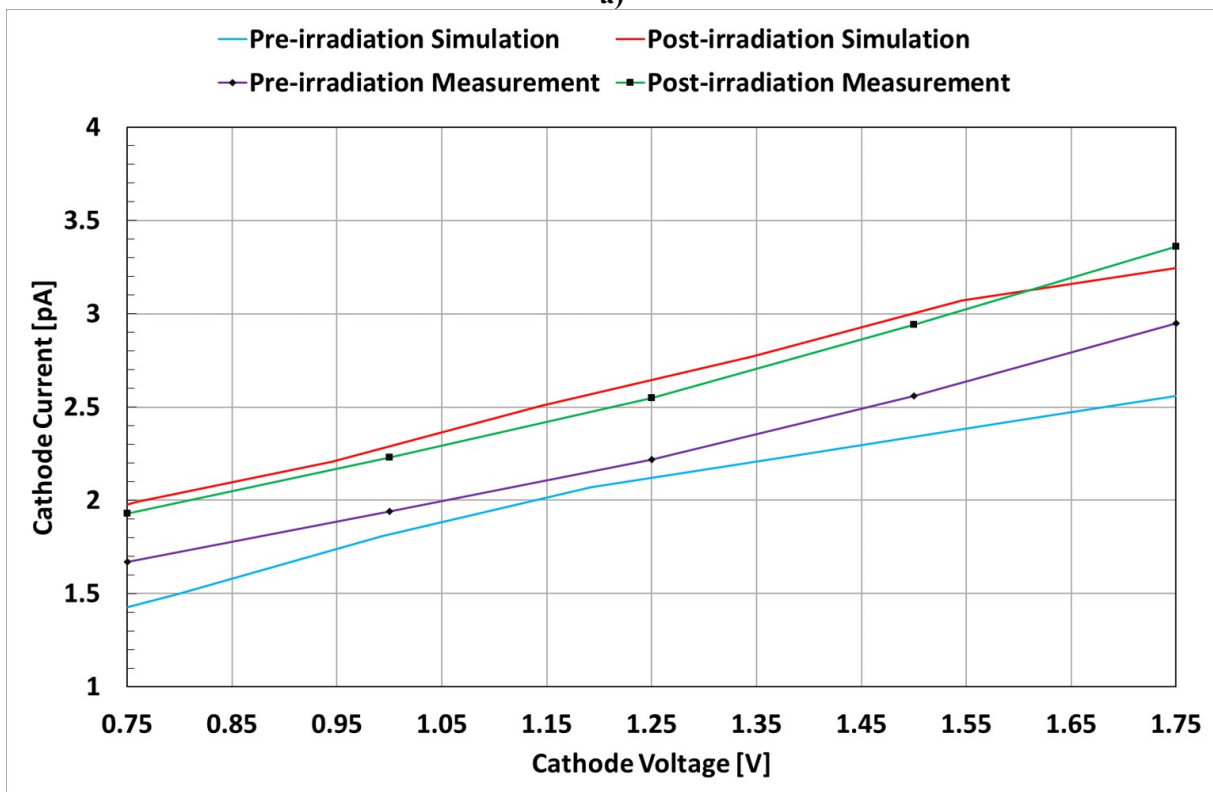
**Figure 7.19.** Comparison of the surface space charge region (SCR) of the photodiode structures corresponding to: **a)** Pre-irradiation simulation, **b)** Post-irradiation simulation at 400 Gy(Si) and **c)** Post-irradiation simulation with eight times increased positive charge in the nitride layer compared to case (b), showing narrower SCR. Simulations were performed at 1.25V reverse bias. SCR width of the post-irradiation simulations at 100 Gy(Si) and at 200 Gy(Si) was the same as the SCR width of the pre-irradiation simulation [102].

### **7.8.1. Dark current comparison between the TCAD simulations and the measurements**

Comparison between pre- and post-irradiation dark current simulations and measurements in 180 nm technology is shown in Figure 7.20. a) [102]. All current values were normalized to the 242 islands. It is shown that the post-irradiation simulation was almost fully fitted to the measurement, whereas the pre-irradiation simulation shows minor deviation from the measurements. The reason for the mismatch was that the defects created during processing, such as the fixed charges in the silicon nitride, were implemented only in the post-irradiation simulation in order to simulate the impact on the TID induced defects. Calibration below 0.25 V was not considered, as the measurement values were in the range of the measurement inaccuracy. Satisfactory fitting, within 3-4 % between 0.75 V and 1.75 V is achieved for the post-irradiation simulation, whereas the pre-irradiation simulations show minor deviation of 5 % at 1.25 V from the measurement, as shown in Figure 7.20 b). The deviation comes from the fact that only the TID effects and impact of these effects were simulated, thus no fabrication defects were implemented in the pre-irradiation simulation [102]. It should be noted that the deviation observed between measurements and simulations is in the range of a few fA, when normalized to the one-island structure [102].



a)



b)

**Figure 7.20.** Comparison between **a)** pre- and post-irradiated simulation and measurement of dark current characteristics. **b)** Fitted segment of the calibrated dark current characteristics between 0.75 V and 1.75 V. Simulations are normalized to 242 islands [102]. The minimum current in the simulations is defined by the numerical error value. The current at 0 V, before normalization to 242 islands, was in the range of 1 fA.

## 7.8.2. Capacitance comparison between the TCAD simulations and the measurements

Comparison between pre- and post-irradiation C-V simulations and measurements is shown in Figure 7.21. As discussed in chapter 7.4., the mismatch between the simulations and the measurements comes from the parasitic contributions to the capacitance, coming from metallization and ILD, were not included in the simulations. The constant shift between the simulated and the measured capacitance corresponds to the parasitic capacitance, which was extracted from the layout, and was in the range of 2.8 pF. Considering the radiation hardness, both the simulations and the measurements show negligible changes after irradiation, indicating that the photodiode capacitance does not change after X-ray exposure. Chapter 7.8., showed a comparison in the SCR width after the addition of the TID induced defects with the SCR width before irradiation. Although the SCR at the surface becomes wider, the total volume of the SCR does not significantly change, meaning that the photodiode capacitance would remain the same. Furthermore, the amount of added fixed charges is too small to significantly affect the capacitance. The simulated capacitance values were shown to be independent of the frequency in the range between 10 kHz and 100 MHz. For the purposes of comparing the two technologies, the measurement frequency was set to 100 kHz, as the photodiodes processed in 350 nm technology were originally measured with an applied small signal of that frequency.

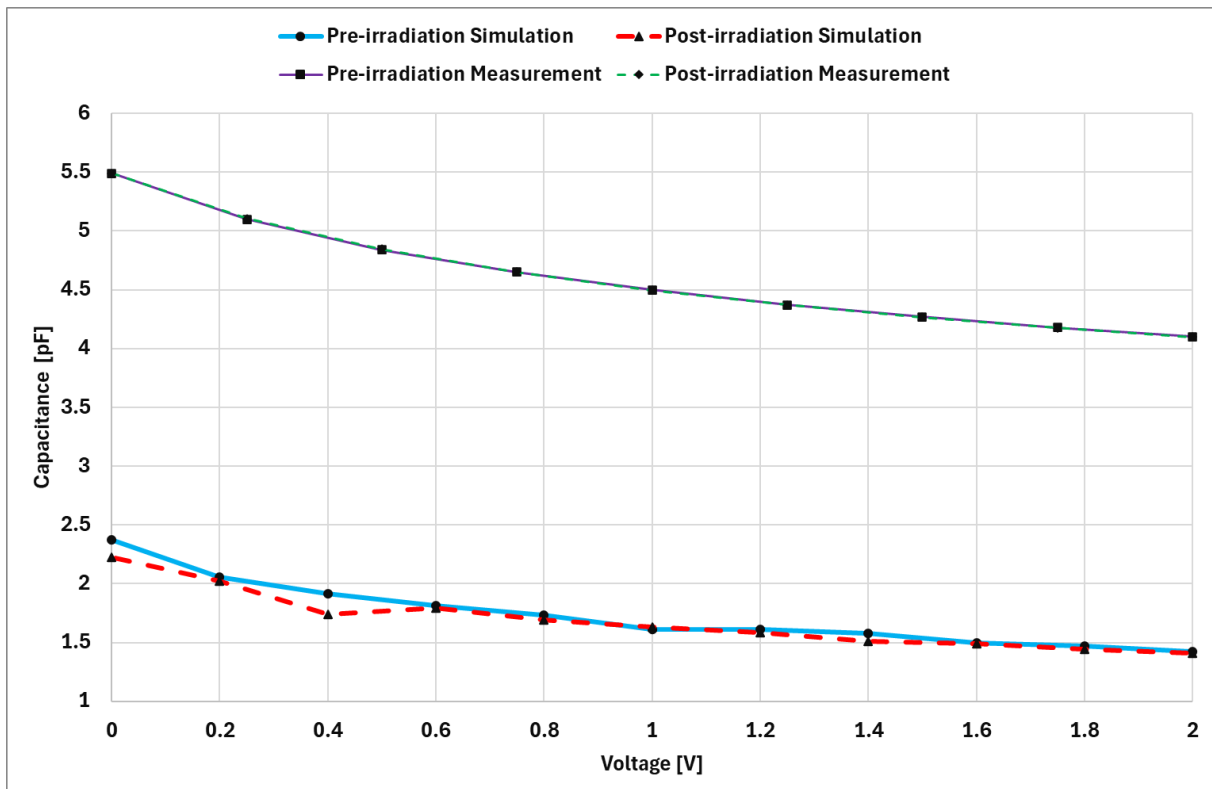




**Figure 7.21.** Comparison between pre- and post-irradiation capacitance-voltage (C-V) simulations and measurements, performed at the frequency of 100 kHz. As discussed in chapter 7.4., the mismatch between the simulations and the measurements is present because the parasitic contributions to the capacitance, coming from metallization and inter level dielectric (ILD), were not included in the simulations.

## 7.9. Summary

2D TCAD process and device simulations of the photodiode structures processed in 180 nm and 350 nm *ams OSRAM* CMOS technologies were simulated and their cross-sections were presented. In addition to the NW islands, the cross-sections additionally included the dielectric stack, that was present above the silicon surface. Main electrical and optical characteristics, such as I-V, C-V and SR characteristics in the case of 350 nm technology, and I-V and C-V in the case of 180 nm technology, were calibrated with the measurements.

In order to model the I-V characteristics in 2D TCAD simulations, the reverse characteristics was normalized to one NW island and afterwards was multiplied by the total number of islands (242) in order to numerically scale it to the measured values. On the other hand, the forward characteristics included seven islands, in order to simulate the impact of the island periphery on the total forward current. Capacitance simulations, similar to the dark current simulations, were normalized to one island and then multiplied by the total number of islands to fit the simulations with the measurements. The discrepancy between the capacitance simulations and measurements comes from the parasitic component that was not simulated. Furthermore, the optical simulations were performed in the case of the photodiode structure processed in 350 nm technology and the simulation domain included one NW island and its periphery which was centered around the middle point of the NW island.

Advanced pre-irradiation simulation calibration with the measurements included a statistical DOE, where input parameters that describe different physical settings, e.g. energy bandgap, doping dependent mobility, SRH recombination and Auger recombination, were varied within their physical boundaries. The parameters with the highest impact on the optical and electrical simulations were included in the RSM, which gave information on how the observed responses behaved according to a quadratic function of the most relevant parameters. The sensitivity analysis of each parameter is obtained by RSM techniques that deliver the variability of each response according to the variation of the input parameters within their range.

Even though the optical simulations were not performed for the structures processed in 180 nm technology, the critical region where the STI reaches the silicon was analyzed. The conclusion is that there was not significant boron segregation if the SPI is omitted. Furthermore,

the electric field in the STI was relatively weak, compared to the electric field in the NW island where the SCR reaches the surface, implying that the defect generation due to X-ray irradiation is minimal. Regardless, it is recommended that the SPI should be included in order to passivate the STI/Si interface, because the optical response heavily depends on the peripheral region, i.e. the area between the NW islands.

TCAD simulations were used to extract the trap level parameters created by ionizing radiation. Similar to the pre-irradiation simulations, a statistical DoE was used, where trap parameters, such as fixed charges in the insulating layers (oxide and nitride), energy level of interface traps, their densities and electron and hole capture cross-sections, were varied within their physical boundaries. Desired fitting is achieved for dark current and capacitance simulations. A TCAD model is proposed, that takes into consideration effects from TID-induced positive fixed charges in the insulating layers as well as interface traps and their behavior depending on the quasi-Fermi level for both electrons and holes as an explanation for higher radiation hardness of photodiode structures processed in 180 nm technology.

## 8. Conclusion

A radiation-hard photodiode structure, implemented in a CT scanner and processed in *ams OSRAM* 180 nm CMOS technology is presented. In the design of a radiation-hard photodiode test-chip, a special starting material was used that consisted of an 18  $\mu\text{m}$  low doped p-type epitaxial layer which was grown on top of the low resistive p-type substrate. Additionally, the epitaxial layer had a high-lifetime minority carrier property, which enabled long diffusion lengths in order to efficiently collect optically generated carriers via diffusion mechanisms. The wafer was divided in four quadrants, each represented by a reference die that received a certain TID. The top right die was a reference die that received no X-ray irradiation and the bottom right quadrant did not have the SPI processed below the STI. A photodiode test-chip was presented consisting of four different photodiode structures, processed and fabricated in *ams OSRAM* mixed signal 180 nm technology. In the photodiode design, STI cut-lines were used in order to allow for correct processing due to size restrictions. Furthermore, the layout consisted of 242 NW islands that were surrounded by the highly-doped p-type surface implant that was used for surface passivation. At the edge of the photodiode, a p/n/p guard-ring was implemented. Finally, below the STI, another SPI was introduced to partially passivate STI/Silicon interface.

Wafer-level X-ray irradiation was performed at Seibersdorf laboratories, where three different dies on the wafer were irradiated with three different TIDs, 100 Gy(Si), 200 Gy(Si) and 400 Gy(Si), respectively, with the dose rate of 100 Gy/h. After the irradiation, the wafer was securely placed in the single-wafer box that was encased in the vacuum bag. The bag was evacuated and afterwards it was placed in the cooling system in order to avoid defect annealing. Finally, the wafer box was transported back to the optical laboratory.

After X-ray exposure, TID induced defects are generated in the insulating layers and at the insulator/silicon interface in the silicon photodiode structures. There are two types of defects that degrade the performance of the optical sensors: the fixed charges in the insulating layers and the interface traps at the insulator/silicon interface. The fixed positive charges are accumulated holes in the insulating layers, close to the interface with silicon. These fixed charges contribute to the generation of interface traps, which are deep-level defects present on the silicon side at the insulator/silicon interface. Due to these defects, the surface recombination rate is increased, resulting in an increased dark current after X-ray exposure. Additionally, in the un-passivated silicon surfaces, optically generated minority electrons can get trapped which results in reduction of optical performance of the silicon photodiodes.

Both the pre- and post-irradiation measurements were performed at a semi-automated probestation. The contacts on the wafer were directly probed and electrical and optical measurements were carried out. Pre-irradiation measurements showed that the dark current depends mainly on the total number of islands and that an inconsistent spacing between the closest island and the STI lines leads to a small increase in the dark current. Furthermore, capacitance measurements showed a similar trend, where the total capacitance dependent on the total number of islands. Spectral responsivity measurements introduced the relevance of optical fiber positioning above the photodiode surface. The wavelength spectrum was between 400 nm and 900 nm, with the target wavelengths being 510 nm, 670 nm, and 780 nm respectively.

In terms of the dark current, the photodiode structures were radiation-hard up to TID = 200 Gy(Si) and only after the TID = 400 Gy(Si), the dark current increased by  $\Delta I = 320$  fA, which was around 10 – 16 % higher than the dark current before X-ray irradiation. Considering the measurement offset of  $\sim 50$  fA, the dark current increase was constant for all four devices, implying that initial dark current is not dependent on the STI area, but rather on the spacing between the nearest island and the STI. In addition to that, the constant current increase indicates that the size of the unit cell does not impact the current degradation. The most critical region where TID induced defects impact the photodiode performance is the region where the SCR reaches the un-passivated surface, which is around the NW islands. The TID induced defects increase the surface recombination, resulting in higher dark current.

In regard to the capacitance characteristics, the photodiode structures were radiation-hard up to TID = 400 Gy(Si), implying that the change in the SCR width at the silicon oxide/silicon interface did not have a meaningful impact on the total SCR volume.

Finally, in optical characterization, it was important to calculate the systematic error, which was present in the measurements due to the fiber misalignment between the measurements. After the measurement normalization, it can be concluded that all four photodiode structures are radiation-hard up to TID = 200 Gy(Si). After the TID = 400 Gy(Si), the spectral characteristics degradation was constant over the wavelength range, with the maximum degradation being in the range of  $\sim 2.3$  % for the device with the largest STI area. In addition to that, the relation between the STI area and the spectral responsivity degradation shows that for larger STI area, the optical performance will degrade more. Since the optical performance mainly depends on the diffusing optically generated minority carriers in the quasi-neutral region, between the islands, some of them may get trapped at the STI/silicon interface, resulting in spectral responsivity degradation.

Even though the dark current before X-ray irradiation was smaller for the photodiode structures fabricated in 350 nm CMOS technology, after the TID = 200 Gy(Si), the dark current increased by 50 %. On the other hand, the photodiode structures fabricated in the 180 nm CMOS were radiation-hard up to TID = 200 Gy(Si) and only had dark current degradation up to 16 % after TID = 400 Gy(Si). A possible explanation for higher radiation hardness in 180nm technology could be the additional trapping of positive charges in the nitride layer, that compensates the effect of the interface traps. Additionally, small differences in other parameters, such as differences in thermal budget and in the doping profiles further contribute to the radiation hardness of the photodiodes processed in 180nm technology.

In terms of capacitance characteristics, devices fabricated in 180 nm technology had higher capacitance before and after irradiation, compared to the similar photodiodes fabricated in 350 nm technology. On the other hand, the photodiodes fabricated in 350 nm technology had a degradation of ~ 3 – 4 % after TID = 200 Gy(Si), whereas the photodiodes fabricated in 180 nm technology were radiation-hard up to TID = 400 Gy(Si). In terms of absolute values, this is a 38% reduction in dark current after a TID of 200 Gy(Si) in the 180nm technology, compared to 350nm technology. Technological differences, such as different thermal budget, implant conditions and steepness of doping profiles contribute to the better performance of the structures fabricated in 350 nm technology before X-ray irradiation. Considering the radiation hardness, the nitride layer, present in the structures fabricated in 180 nm technology, could be a possible explanation of improved radiation-hardness.

Finally, the spectral responsivity of the photodiodes fabricated in 180 nm technology was 20 – 45 % higher, than the spectral responsivity of the devices fabricated in 350 nm technology. In terms of radiation hardness, after the TID = 400 Gy (Si) there was a small degradation of the spectral responsivity, ranging between 0.93 and 2.29 %, in case of the devices fabricated in 180 nm technology. The reason for that degradation are the STI lines, which were implemented in 180 nm technology in order to allow correct processing. Furthermore, in order to improve the radiation hardness of the structures fabricated in 180 nm technology, further optimization of the STI lines can be made, in order to mitigate both the spectral responsivity and the dark current before and after X-ray irradiation. Comparing the radiation hardness of the similar photodiodes between the two CMOS technology, at the same TID = 200 Gy(Si), it can be concluded that both structures are radiation-hard, as the degradation is < 0.8 %. In addition to that, a comparison in normalized photo-to-dark current ratio (nPDR) degradation after TID = 400 Gy(Si) in the case of photodiode processed in 180 nm technology (Device 1), and TID = 200 Gy(Si) in the case of the photodiode processed in 350 nm technology, is analyzed.

In both technologies the dark current degradation was more affected by the TID, compared to the SR. It is therefore concluded that the nPDR is dominantly impacted by the dark current increase after the TID. The degradation of the nPDR was in the range of 15 % for the photodiodes processed in 180 nm technology, compared to 45 % – 50 % degradation for the photodiodes processed in 350 nm technology.

2D TCAD simulations of the photodiode structures processed in 180 nm and 350 nm *ams OSRAM* CMOS technologies were simulated and their cross-sections were presented. In addition to the NW islands, the cross-sections additionally included the dielectric stack, that was present above the silicon. Main electrical and optical characteristics, such as IV, CV and SR characteristics, were calibrated with the measurements.

In order to model the IV characteristics in 2D TCAD simulations, the reverse characteristics was normalized to one NW island and afterwards was multiplied by the total number of islands (242) in order to numerically scale it to the measured values. On the other hand, the forward characteristics included seven islands, in order to simulate the impact of the island periphery on the total forward current. Capacitance simulations, similar to the dark current simulations, were normalized to one island and then multiplied by the total number of islands to fit the simulations with the measurements. The discrepancy between the capacitance simulations and measurements comes from the parasitic component that was not simulated. Furthermore, the optical simulations were performed in the case of the photodiode structure processed in 350 nm technology and the simulation domain included one NW island and its periphery which was centered around the middle point of the NW island.

Advanced pre-irradiation simulation calibration with the measurements included a statistical DOE, where input parameters that describe different physical settings, e.g. energy bandgap, doping dependent mobility, SRH recombination and Auger recombination, were varied within their physical boundaries. The parameters with the highest impact on the optical and electrical simulations were included in the RSM, which gave information on how the observed responses behaved according to a quadratic function of the most relevant parameters. The sensitivity analysis of each parameter is obtained by RSM techniques that deliver the variability of each response according to the variation of the input parameters within their range.

Even though the optical simulations were not performed for the structures processed in 180 nm technology, the critical region where the STI reaches the silicon was analyzed. The conclusion is that there was not significant boron segregation if the SPI is omitted. Furthermore, the electric field in the STI was relatively weak, compared to the electric field in the NW island where the SCR reaches the surface, implying that the defect generation due to X-ray irradiation

should be minimal. Regardless, it is recommended that the SPI should be included in order to passivate the STI/Si interface, because the optical response heavily depends on the peripheral region, i.e. the area between the NW islands.

TCAD simulations were used to extract the trap level parameters created by ionizing radiation. Similar to the pre-irradiation simulations, a statistical DOE was used, where trap parameters, such as fixed charges in the insulating layers (oxide and nitride), energy level of interface traps, their densities and electron and hole capture cross-sections, were varied within their physical boundaries. Satisfactory fitting is achieved for dark current and capacitance simulations. A TCAD model is proposed, that takes into consideration effects from TID-induced positive fixed charges in the insulating layers as well as interface traps and their behavior depending on the quasi-Fermi level for both electrons and holes as an explanation for higher radiation hardness of photodiode structures processed in 180nm technology.

## 9. Bibliography

- [1] G. Weckler, "Operation of p-n junction photodetectors in a photon flux integrating mode," *IEEE J. Solid-State Circuits*, vol. 2, pp. 65-73, Sept. 1967, DOI: 10.1109/JSSC.1967.1049795
- [2] Y. Xu, "Fundamental Characteristics of a Pinned Photodiode CMOS Pixel," Ph.D. dissertation, Delft University of Technology, Delft, NL, 2015
- [3] F. M. Li, A. Nathan, "Overview of CCD", in *CCD Image Sensors in Deep-Ultraviolet, Degradation Behavior and Damage Mechanisms*, NL, 2005, ch. 2, pp. 7-9
- [4] P. Denyer, *et al.*, "On-chip CMOS sensors for VLSI imaging systems," in *Proc. VLSI-91*, Edinburgh, Scotland, 1991, pp. 157–166
- [5] P. Noble, "Self-scanned image detector arrays," *IEEE Trans. Electron Devices*, vol. 15, no. 4, pp. 202-209, Apr. 1968, DOI: 10.1109/T-ED.1968.16167
- [6] E. R. Fossum, "Active pixel sensors: Are CCD's dinosaurs?," in *Proc. SPIE*, San Jose, CA, USA, 1993, pp. 30-39
- [7] B. Fowler, A. El Gamal, D.X.D. Yang, "A CMOS area image sensor with pixel-level A/D conversion," in *Proc. ISSCC '94*, San Francisco, CA, USA, Feb. 1994, pp. 226-227
- [8] U. Jain, "Characterization of CMOS image sensors," MSc thesis, Delft University of Technology, Delft, NL, 2016
- [9] A. El Gamal, H. Eltoukhy, "CMOS image sensors," in *IEEE Circuits Devices Mag.*, vol. 21, no. 3, pp. 6-20, Jun. 2006, DOI: 10.1109/MCD.2005.1438751
- [10] R. Tejas, P. Macherla, N. Shylashree, "Image Sensor – CCD and CMOS," in *Microelectronics, Communication Systems, Machine Learning and Internet of Things*, vol 887, pp. 455-484, Jan. 2023, DOI: 10.1007/978-981-19-1906-0\_40
- [11] C. H. Chen, *et al.*, "Study for cross-contamination between CMOS image sensor and IC product," in *2001 IEEE/SEMI Advanced Semiconductor Manufacturing Conference*, Munich, Germany, Apr. 2001, pp. 121-123, DOI: 10.1109/ASMC.2001.925629
- [12] H. S. P. Wong, "CMOS image sensors – recent advances and device scaling considerations," in *IEDM*, pp. 201-204, Dec. 1997, DOI: 10.1109/IEDM.1997.650332
- [13] A. Theuwissen, "CCD or CMOS image sensors for consumer digital still photography?," in *International Symposium on VLSI Technology, Systems, and Applications*, pp. 168-171, Apr. 2001, DOI: 10.1109/VTSA.2001.934511
- [14] M. Hillebrand, *et al.*, "High speed camera system using a CMOS image sensor," in *Proc. IEEE Symposium on Intelligent Vehicle Symposium*, Dearborn, MI, USA, Oct. 2000, pp. 656-661



- [15] M. Bigas, *et al.*, “Review of CMOS image sensors,” *Microelectronics J.*, vol. 37, no. 5, pp. 433-451, Sep. 2005, DOI: doi.org/10.1016/j.mejo.2005.07.002
- [16] J. W. van Hoorne, “Study and development of a novel silicon pixel detector for the upgrade of the ALICE Inner Tracking System,” PhD dissertation, Technische Universität Wien, Vienna, AT, 2015
- [17] W. Snoeys, “CMOS monolithic active pixel sensors for high energy physics,” *Nucl. Instrum. Methods Phys. Res. A*, Vol. 765, pp. 167-171, Jul. 2014, DOI: doi.org/10.1016/j.nima.2014.07.017
- [18] N. Wermes, “Depleted CMOS pixels for LHC proton-proton experiments,” *Nucl. Instrum. Methods Phys. Res. A*, Vol. 824, pp. 483-486, Jul. 2016, DOI: doi.org/10.1016/j.nima.2015.09.038
- [19] T. Kishishita, *et al.*, “Characterization of Depleted monolithic Active Pixel detectors implemented with a high-resistive CMOS technology,” *Nucl. Instrum. Methods Phys. Res. A*, Vol. 824, pp. 417-418, Jul. 2016, DOI: doi.org/10.1016/j.nima.2015.09.048
- [20] E. Shefer, *et al.*, “State of the Art of CT Detectors and Sources: A Literature Review,” *Curr. Radiol. Rep.*, vol. 1, pp. 76-91, Feb. 2013, DOI: 10.1007/s40134-012-0006-4
- [21] A. Noel, F. Thibault, “Digital detectors for mammography: the technical challenges,” *European Radiology*, vol. 14, pp. 1990-1998, Oct. 2004, DOI: 10.1007/s00330-004-2446-6
- [22] W. Rossner, M. Ostertag, F. Jermann, “Properties and applications of gadolinium oxysulfide based ceramic scintillators,” in *proc. of the seventh international symposium on physics and chemistry of luminescent materials*, vol. 98-24, 1999, pp. 187-194
- [23] R. Nakamura, “Improvements in the X-ray Characteristics of Gd<sub>2</sub>O<sub>2</sub>S:Pr Ceramic Scintillators,” *J. of the American Ceramic Society*, vol. 82, no. 9, pp. 2407-2410, Feb. 1999, DOI: 10.1111/j.1151-2916.1999.tb02097.x
- [24] V. Goiffon, *et al.*, “Total Dose Evaluation of Deep Submicron CMOS Imaging Technology Through Elementary Device and Pixel Array Behavior Analysis”, *IEEE Trans. Nucl. Sci.*, vol. 55, no. 6, pp. 3494-3501, Dec. 2008, DOI: 10.1109/TNS.2008.2005294
- [25] V. Goiffon, *et al.*, “Radiation Effects in Pinned Photodiode CMOS Image Sensors: Pixel Performance Degradation Due to Total Ionizing Dose”, *IEEE Trans. Nucl. Sci.*, vol. 59, no. 6, pp. 2878-2887, Dec. 2012, DOI: 10.1109/TNS.2012.2222927

- [26] V. Goiffon, *et al.*, “Analysis of Total Dose-Induced Dark Current in CMOS Image Sensors From Interface State and Trapped Charge Density Measurements,” *IEEE Trans. Nucl. Sci.*, vol. 57, no. 6, pp. 3087-3094, Dec. 2010, DOI: 10.1109/TNS.2010.2077653
- [27] M. Jakubek, *et al.*, “3D imaging of radiation damage in silicon sensor, and spatial mapping of charge collection efficiency,” *J. Inst.*, vol. 8, no. 3, pp. 1-10, Mar. 2013, DOI: 10.1088/1748-0221/8/03/C03023.
- [28] W. Shockley and W. T. Read, „Statistics of the Recombination of Holes and Electrons,“ *Phys. Rev.*, vol. 87, no. 5, pp. 835-842, Sept. 1952, DOI: 10.1103/PhysRev.87.835
- [29] B. R. Hancock, *et al.*, “Multi-megarad (Si) radiation-tolerant integrated CMOS imager”, *Proc. SPIE*, San Jose, CA, USA, 2001, pp. 147-155
- [30] V. Goiffon, M. Estriebeau, P. Magnan, “Overview of Ionizing Radiation effects in Image Sensors Fabricated in a Deep-Submicrometer CMOS Imaging Technology”, *IEEE Trans. Electron Devices*, vol. 56, no. 11, pp. 2594-2601, Nov. 2009, DOI: 10.1109/TED.2009.2030623 2009.
- [31] V. Goiffon, *et al.*, “Generic Radiation Hardened Photodiode Layouts for Deep Submicron CMOS Image Sensor Processes,“ *IEEE Trans. Nucl. Sci.*, vol. 58, no. 6, pp. 3076-3084, Dec. 2011, DOI: 10.1109/TNS.2011.2171502
- [32] S. Rizzolo, *et al.*, “Radiation Hardness Comparison of CMOS Image Sensor Technologies at High Total Ionizing Dose Levels,“ *IEEE Trans. Nucl. Sci.*, vol. 66, no. 1, pp. 111-119, Jan. 2019, DOI: 10.1109/TNS.2018.2884037
- [33] E. R. Fossum, „CMOS Image Sensors: Electronic Camera-On-A-Chip,“ *IEEE Trans. Electron Devices*, vol. 44, no. 10, pp. 1689-1698, Oct. 1997, DOI: 10.1109/16.628824.
- [34] W. Snoeys, „Monolithic pixel detectors for high energy physics,“ *Nucl. Instrum. Methods Phys. Res. A*, vol. 731, pp. 125-130, Dec. 2013, DOI: 10.1016/j.nima.2013.05.073
- [35] F. Šegmanović, *et al.*, "Optical and electrical simulations of radiation-hard photodiode in 0.35 $\mu$ m high-voltage CMOS technology," *2018 28th Int. Symp. on Power and Timing Modeling, Optimization and Simulation (PATMOS)*, Costa Brava, Spain, 2018, pp. 92-96, DOI: 10.1109/PATMOS.2018.8464156
- [36] F. Faccio, “Radiation effects in the electronics for CMS”, *Radiation Tutorial*, CERN, 2017, [https://lhcb-elec.web.cern.ch/papers/radiation\\_tutorial.pdf](https://lhcb-elec.web.cern.ch/papers/radiation_tutorial.pdf)
- [37] H. Spieler, “Solid State Detectors – VII. Radiation Effects”, 2012, [https://www-physics.lbl.gov/~spieler/USPAS-MSU\\_2012/pdf/VII\\_Radiation\\_Effects.pdf](https://www-physics.lbl.gov/~spieler/USPAS-MSU_2012/pdf/VII_Radiation_Effects.pdf)

- [38] J. R. Schwank, et al., “Radiation Effects in MOS Oxides,” *IEEE Trans. Nucl. Sci.*, vol. 55, no. 4, pp. 1833-1853, Aug. 2008, DOI: 10.1109/TNS.2008.2001040
- [39] R. C. Hughes, “Hole mobility and transport in thin SiO<sub>2</sub> films,” *Appl. Phys. Lett.*, vol. 26, no. 8, pp. 436–438, Apr. 1975, DOI: 10.1063/1.88200
- [40] R. C. Hughes, “Charge carrier transport phenomena in amorphous SiO<sub>2</sub>: Direct measurement of the drift mobility and lifetime,” *Phys. Rev. Lett.*, vol. 30, no. 26, pp. 1333–1336, Jun. 1973, DOI: <https://doi.org/10.1103/PhysRevLett.30.1333>
- [41] F. B. McLean, H. E. Boesch Jr., and J. M. McGarrity, “Dispersive Hole Transport in SiO<sub>2</sub>,” Adelphi, MD, Harry Diamond Laboratory, 1987, Tech. Rep. HDL-TR-2117.
- [42] T. R. Oldham, and F. B. McLean, “Total Ionizing Dose Effects in MOS Oxides and Devices”, *IEEE Trans. Nucl. Sci.*, vol. 50, no. 3, pp. 483-499, Jul. 2003, DOI: 10.1109/TNS.2003.812927
- [43] F. B. McLean, T. R. Oldham, “Basic Mechanisms of Radiation Effects in Electronic Materials and Devices,” Adelphi, MD, Harry Diamond Laboratory, 1987, Tech. Rep. HDL-TR-2129.
- [44] G. A. Asuman, Jr., F. B. McLean, “Electron-hole pair creation energy in SiO<sub>2</sub>,” *Appl. Phys. Lett.*, vol. 26, no. 4, pp. 173-175, Feb. 1975, DOI: 10.1063/1.88104
- [45] G. A. Ausman, “Field dependence of geminate recombination in a dielectric medium,” Adelphi, MD, Harry Diamond Laboratory, 1987, Tech. Rep. HDL-TR-2097.
- [46] M. R. Shaneyfelt, *et al.*, “Charge yield for cobalt-60 and 10 keV x-ray irradiations,” *IEEE Trans. Nucl. Sci.*, vol. 38, no. 6, pp. 1187–1194, Dec. 1991, DOI: 10.1109/23.124092
- [47] J. M. Benedetto, H. E. Boesch, Jr., “The relationship between 60Co and 10 keV X-ray damage in MOS devices,” *IEEE Trans. Nucl. Sci.*, vol. 33, no. 6, pp. 1317-1323, Dec. 1986, DOI: 10.1109/TNS.1986.4334599
- [48] C. Kittel, “Energy bands,” in *Introduction to Solid State Physics*, 8th ed., John Wiley & Sons, Inc, Hoboken, NJ, USA, 2005, ch. 7, pp. 161-184
- [49] F. B. McLean, G. A. Ausman Jr., “Simple approximate solutions to continuous-time random-walk transport,” *Phys. Rev. B*, vol. 15, no. 2, pp. 1052–1061, Jan. 1977.
- [50] F. B. McLean, *et al.*, “Application of stochastic hopping transport to hole conduction in amorphous SiO<sub>2</sub>,” *J. Appl. Phys.*, vol. 47, no. 4, pp. 1529–1532, Apr. 1976.
- [51] W. L. Warren, *et al.*, “Microscopic nature of border traps in MOS devices,” *IEEE Trans. Nucl. Sci.*, vol. 41, no. 6, pp. 1817–1827, Dec. 1994, DOI: 10.1109/23.340513

- [52] M. R. Shaneyfelt, *et al.*, “Field dependence of interface trap buildup in polysilicon and metal gate MOS devices,” *IEEE Trans. Nucl. Sci.*, vol. 37, no. 6, pp. 1632–1640, Dec. 1990, DOI: 10.1109/23.101171
- [53] C. M. Dozier, D. B. Brown, “Photon energy dependence of radiation effects in MOS structures,” *IEEE Trans. Nucl. Sci.*, vol. 27, no. 6, pp. 1694–1699, Dec. 1980, DOI: 10.1109/TNS.1980.4331090
- [54] C. M. Dozier, D. B. Brown, “Effects of photon energy on the response of MOS devices,” *IEEE Trans. Nucl. Sci.*, vol. 28, no. 6, pp. 4137–4141, Dec. 1981, DOI: 10.1109/TNS.1981.4335689
- [55] D. B. Brown, C. M. Dozier, “Electron-hole recombination in irradiated SiO<sub>2</sub> from a microdosimetry viewpoint,” *IEEE Trans. Nucl. Sci.*, vol. 28, no. 6, pp. 4142–4144, Dec. 1981, DOI: 10.1109/TNS.1981.4335690
- [56] C. M. Dozier, *et al.*, “An evaluation of low-energy X-Ray and Cobalt-60 irradiations of MOS transistors,” *IEEE Trans. Nucl. Sci.*, vol. 34, no. 6, pp. 1535–1539, Dec. 1987, DOI: 10.1109/TNS.1987.4337511
- [57] J. R. Srour, O. L. Curtis Jr., K. Y. Chiu, “Charge transport studies in SiO<sub>2</sub>: Processing effects and implications for radiation hardening,” *IEEE Trans. Nucl. Sci.*, vol. 21, no. 6, pp. 73–80, Dec. 1974, DOI: 10.1109/TNS.1974.6498909
- [58] D. M. Fleetwood, P. S. Winokur, J. R. Schwank, “Using laboratory X-ray and Co-60 irradiations to predict CMOS device response in strategic and space environments,” *IEEE Trans. Nucl. Sci.*, vol. 35, no. 6, pp. 1497–1505, Dec. 1988, DOI: 10.1109/23.25487
- [59] F. B. McLean, “A direct tunneling model of charge transfer at the insulator semiconductor interface in MIS devices,” Adelphi, MD, Harry Diamond Laboratory, 1976, HDL-TR-1765.
- [60] G. F. Derbenwick, H. H. Sander, “CMOS hardness prediction for low-dose-rate environments,” *IEEE Trans. Nucl. Sci.*, vol. 24, no. 6, pp. 2244–2247, Dec. 1977, DOI: 10.1109/TNS.1977.4329200
- [61] P. S. Winokur, “Limitations in the use of linear systems theory for the prediction of hardened-MOS device response in space satellite environments,” *IEEE Trans. Nucl. Sci.*, vol. 29, no. 6, pp. 2101–2106, Dec. 1982, DOI: 10.1109/TNS.1982.4336504
- [62] P. S. Winokur, K. G. Kerris, L. Harper, “Predicting CMOS inverter response in nuclear and space environments,” *IEEE Trans. Nucl. Sci.*, vol. 30, no. 6, pp. 4326–4332, Dec. 1983, DOI: 10.1109/TNS.1983.4333132

- [63] S. Manzini, A. Modelli, "Discharge of trapped holes in silicon dioxide," in *Insulating Films on Semiconductors*, edited by J. F. Verweij and D. R. Wolters, Eds. New York: Elsevier, 1983, pp. 112–115
- [64] T. R. Oldham, A. J. Lelis, F. B. McLean, "Spatial dependence of trapped holes determined from tunneling analysis and measured annealing," *IEEE Trans. Nucl. Sci.*, vol. 33, no. 6, pp. 1203-1209, Dec. 1986, DOI: 10.1109/TNS.1986.4334579
- [65] V. Lakshmana, A. S. Vengurlekar, "Logarithmic detrapping response for holes injected into SiO and the influence of thermal activation and electric fields," *J. Appl. Phys.*, vol. 63, p. 4548-4554, May 1988, DOI: 10.1063/1.340153
- [66] P. J. McWhorter, S. L. Miller, W. M. Miller, "Modeling the anneal of radiation-induced trapped holes in a varying thermal environment," *IEEE Trans. Nucl. Sci.*, vol. 37, no. 6, pp. 1682–1689, Dec. 1990, DOI: 10.1109/23.101177
- [67] M. Schmidt, K. Koster Jr., "Hole trap analysis in SiO<sub>2</sub>/Si structures by electron tunneling," *Phys. Stat. Sol. B*, vol. 174, no. 1, pp. 53–66, Nov. 1992, DOI: 10.1002/pssb.2221740106
- [68] A. J. Lelis, *et al.*, "The nature of the trapped hole annealing process," *IEEE Trans. Nucl. Sci.*, vol. 36, no. 6, pp. 1808–1815, Dec. 1989, DOI: 10.1109/23.45373
- [69] M. Simons, H. L. Hughes, "Determining the energy distribution of pulsed-radiation-induced charge in MOS structures from rapid annealing measurements," *IEEE Trans. Nucl. Sci.*, vol. 19, no. 6, pp. 282-290, Dec. 1972, DOI: 10.1109/TNS.1972.4326846
- [70] M. Simons, H. L. Hughes, "Short-Term Charge Annealing in Electron-Irradiated Silicon Dioxide," *IEEE Trans. Nucl. Sci.*, vol. 18, no. 6, pp. 106-112, Dec. 1971, DOI: 10.1109/TNS.1971.4326420
- [71] J. G. Simmons, G. W. Taylor, "High-field isothermal currents and thermally stimulated currents in insulators having discrete trapping levels," *Phys. Rev. B*, vol. 5, no. 4, pp. 1619-1629, Feb. 1972, DOI: 10.1103/PhysRevB.5.1619
- [72] Z. Shanfield, "Thermally stimulated current measurements on irradiated MOS capacitors," *IEEE Trans. Nucl. Sci.*, vol. 30, no. 6, pp. 4064-4070, Dec. 1983, DOI: 10.1109/TNS.1983.4333082
- [73] Z. Shanfield, M. Moriwaki, "Radiation-induced hole trapping and interface state characteristics of al-gate and poly-si gate MOS capacitors," *IEEE Trans. Nucl. Sci.*, vol. 32, no. 6, pp. 3929-3934, Dec. 1985, DOI: 10.1109/TNS.1985.4334045

- [74] Z. Shanfield, M. Moriwaki, "Characteristics of hole traps in dry and pyrogenic gate oxides," *IEEE Trans. Nucl. Sci.*, vol. 31, no. 6, pp. 1242-1248, Dec. 1984, DOI: 10.1109/TNS.1984.4333490
- [75] D. M. Fleetwood, R. A. Reber, P. S. Winokur, "Effect of bias on thermally stimulated current (TSC) in irradiated MOS devices," *IEEE Trans. Nucl. Sci.*, vol. 38, no. 6, pp. 1066-1077, Dec. 1991, DOI: 10.1109/23.124076
- [76] D. M. Fleetwood, *et al.*, "New insights into radiation-induced oxide-trapped charge through thermally stimulated current measurement and analysis," *IEEE Trans. Nucl. Sci.*, vol. 39, no. 6, pp. 2192-2203, Dec. 1992, DOI: 10.1109/23.211421
- [77] D. M. Fleetwood, *et al.*, "The role of border traps in MOS high-temperature postirradiation annealing response," *IEEE Trans. Nucl. Sci.*, vol. 40, no. 6, pp. 1323-1334, Dec. 1993, DOI: 10.1109/23.273535
- [78] D. M. Fleetwood, *et al.*, "Effects of oxide traps, interface traps, and border traps on MOS devices," *J. Appl. Phys.*, vol. 73, no. 10, pp. 5058-5074, May 1993, DOI: 10.1063/1.353777
- [79] D. M. Fleetwood, "Revised model of thermally stimulated current in MOS capacitors," *IEEE Trans. Nucl. Sci.*, vol. 44, no. 6, pp. 1826-1833, Dec. 1997, DOI: 10.1109/23.658949
- [80] P. J. McWhorter, S. L. Miller, T. A. Dellin, "Modeling the memory retention characteristics of SNOS nonvolatile transistors in a varying thermal environment," *J. Appl. Phys.*, vol. 68, no. 4, pp. 1902-1909, Aug. 1990, DOI: 10.1063/1.346580
- [81] J. R. Schwank, *et al.*, "Physical mechanisms contributing to device Rebound," *IEEE Trans. Nucl. Sci.*, vol. 31, no. 6, pp. 1434-1438, Dec. 1984, DOI: 10.1109/TNS.1984.4333525
- [82] P. S. Winokur, *et al.*, "Correlating the radiation response of MOS capacitors and transistors," *IEEE Trans. Nucl. Sci.*, vol. 31, no. 6, pp. 1453-1460, Dec. 1984, DOI: 10.1109/TNS.1984.4333529
- [83] D. M. Fleetwood, "Long-term annealing study of midgap interface-trap charge neutrality," *Appl. Phys. Lett.*, vol. 60, no. 23, pp. 2883-2885, Jun. 1992, DOI: 10.1063/1.106807
- [84] P. J. McWhorter, P. S. Winokur, R. A. Pastorek, "Donor/acceptor nature of radiation-induced interface traps," *IEEE Trans. Nucl. Sci.*, vol. 35, no. 6, pp. 1154-1159, Dec. 1988, DOI: 10.1109/23.25433

- [85] Y. Y. Kim, P. M. Lenahan, "Electron-spin resonance study of radiation-induced paramagnetic defects in oxides grown on (100) silicon substrates," *J. Appl. Phys.*, vol. 64, no. 7, pp. 3551–3557, Oct. 1988, DOI: 10.1063/1.341494
- [86] N. S. Saks, C. M. Dozier, D. B. Brown, "Time dependence of interface trap formation in MOSFETs following pulsed irradiation," *IEEE Trans. Nucl. Sci.*, vol. 35, no. 6, pp. 1168-1177, Dec. 1988, DOI: 10.1109/23.25435
- [87] D. L. Griscom, D. B. Brown, N. S. Saks, "Nature of Radiation-Induced Point Defects in Amorphous SiO<sub>2</sub> and Their Role in SiO<sub>2</sub> -ON-Si Structures," in *The Physics and Chemistry of SiO<sub>2</sub> and the Si/SiO<sub>2</sub> Interface*, New York, USA, 1988, ch. 4, sec. 2, pp. 287-297
- [88] J. M. McGarrity, *et al.*, "Interface states resulting from a hole flux incident on the SiO<sub>2</sub> /Si interface," *The Physics of SiO<sub>2</sub> and its Interfaces*, pp. 428–432, Mar. 1978, DOI: 10.1016/B978-0-08-023049-8.50079-8
- [89] M. R. Shaneyfelt, *et al.*, "Interface-trap buildup rates in wet and dry oxides," *IEEE Trans. Nucl. Sci.*, vol. 39, no. 6, pp. 2244–2251, Dec. 1992, DOI: 10.1109/23.211427
- [90] T. R. Oldham, *et al.*, "An overview of radiation-induced interface traps in MOS structures," *Semiconduct. Sci. Technol.*, vol. 4, no. 12, pp. 986, Dec. 1989, DOI: 10.1088/0268-1242/4/12/004
- [91] P. S. Winokur, F. B. McLean, H. E. Boesch, Jr., "Physical processes associated with radiation-induced interface states," Adelphi, MD, Army Harry Diamond Laboratory, 1986, HDL-TR-2081.
- [92] S. R. Hofstein, "Proton and sodium transport in SiO films," *IEEE Trans. Electron Devices*, vol. 14, no. 11, pp. 749-759, Nov. 1967, DOI: 10.1109/T-ED.1967.16102
- [93] J. R. Schwank, *et al.*, "Radiation induced interface state generation in MOS devices," *IEEE Trans. Nucl. Sci.*, vol. 33, no. 6, pp. 1178–1184, Dec. 1986, DOI: 10.1109/TNS.1986.4334575
- [94] P. S. Winokur, *et al.*, "Total-dose failure mechanisms of integrated circuits in laboratory and space environments," *IEEE Trans. Nucl. Sci.*, vol. 34, no. 6, pp. 1448–1454, Dec. 1987, DOI: 10.1109/TNS.1987.4337496
- [95] N. S. Saks, D. B. Brown, R. W. Rendell, "Effects of switched bias on radiation-induced interface trap formation," *IEEE Trans. Nucl. Sci.*, vol. 38, no. 6, pp. 1130–1139, Dec. 1991, DOI: 10.1109/23.124085

- [96] P. S. Winokur, *et al.*, “Two-stage process for buildup of radiation-induced interface states,” *J. Appl. Phys.*, vol. 50, no. 5, pp. 3492–3495, May 1979, DOI: 10.1063/1.326344
- [97] D. M. Fleetwood, P. V. Dressendorfer, D. C. Turpin, “A reevaluation of the worst-case postirradiation response for hardened MOS transistors,” *IEEE Trans. Nucl. Sci.*, vol. NS-34, no. 6, pp. 1178–1183, Dec. 1987, DOI: 10.1109/TNS.1987.4337449
- [98] S. N. Rashkeev, *et al.*, “Effects of hydrogen motion on interface trap formation and annealing,” *IEEE Trans. Nucl. Sci.*, vol. 51, no. 6, pp. 3158–3165, Dec. 2004, DOI: 10.1109/TNS.2004.839202
- [99] X. J. Chen, *et al.*, “Nature of interface defect buildup in gated bipolar devices under low dose rate irradiation,” *IEEE Trans. Nucl. Sci.*, vol. 53, no. 6, pp. 3649–3654, Dec. 2006, DOI: 10.1109/TNS.2006.885375
- [100] Z. Li, “Radiation damage effects in Si materials and detectors and rad-hard Si detectors for SLHC,” *J. Inst.*, vol. 4, no. 3, pp. 1-32, Mar. 2009, DOI: 10.1088/1748-0221/4/03/P03011
- [101] V. Goiffon, *et al.*, "Radiation Damages in CMOS Image Sensors: Testing and Hardening Challenges Brought by Deep Sub-Micrometer CIS Processes", *Proc. SPIE 7826*, Toulouse, FR, 2010
- [102] F. Šegmanović, *et al.*, “Evaluation of the Radiation Hardness of Photodiodes in 180-nm CMOS Technology for Medical Applications”, *IEEE Trans. Nucl. Sci.*, vol. 68, no. 9, pp. 2367–2374, Sep. 2021, DOI: 0.1109/TNS.2021.3101920
- [103] *Standard Practice for Calculating Absorbed Dose From Gamma or X Radiation*, ASTM E0666-21 Standard, Mar. 2021
- [104] *Radiological Health Handbook*, U.S. Department of Health, Education, and Welfare, Rockville, Maryland 20852, Jan. 1970.
- [105] B. E. Burke, *et al.*, “Soft X-Ray CCD Imagers for AXAF,” *IEEE Trans. Elec. Dev.*, vol. 44, no. 10, pp. 1633–1642, Oct. 1997, DOI: 10.1109/16.628815
- [106] Synopsys, “Sentaurus™ Device User Guide,” Mar. 2022.
- [107] F. Šegmanović, *et al.*, "Impact of TCAD Model Parameters on Optical and Electrical Characteristics of Radiation-Hard Photodiode in 0.35μm CMOS Technology," *2018 41st Int. Conv. on Information and Communication Technology, Electronics and Microelectronics (MIPRO)*, Opatija, Croatia, 2018, pp. 18-22, DOI: 10.23919/MIPRO.2018.8400003



- [108] W. Bludau, A. Onton, W. Heinke, "Temperature dependence of the band gap in silicon," *J. Appl. Phys.*, vol. 45, no. 4, pp. 1846-1848, Apr. 1974, DOI: 10.1063/1.1663501
- [109] F. Roger, "Methodologie De Calibrage De Simulateurs Utilises en Microelectronique – Application A L'Implantation Ionique Et A La Mobilité des Porteurs," Ph.D. dissertation, Institut national polytechnique de Grenoble, Grenoble, FR, 2002
- [110] G. Masetti, M. Severi, S. Solmi, "Modeling of Carrier Mobility Against Carrier Concentration in Arsenic-, Phosphorus-, and Boron-Doped Silicon," *IEEE Trans. Electron Devices*, vol. 30, no. 7, pp. 764-769, Jul. 1983, DOI: 10.1109/T-ED.1983.21207
- [111] D. J. Roulston, N. D. Arora, S. G. Chamberlain, "Modeling and Measurement of Minority-Carrier Lifetime versus Doping in Diffused Layers of n<sup>+</sup>-p Silicon Diodes," *IEEE Trans. Electron Devices*, vol. 29, no. 2, pp. 284-291, Feb. 1982, DOI: 10.1109/T-ED.1982.20697
- [112] S. M. Sze, Kwok K. Ng, "Physics and Properties of Semiconductors – A Resume", in *Physics of semiconductor devices*, third edition, John Wiley & Sons, Inc, Hoboken, NJ, USA, 2006, ch. 1, sec. 1.5, pp. 27-38
- [113] L. Huldt, N. G. Nilsson, K. G. Svantesson, "The temperature dependence of band-to-band Auger recombination in silicon," *Appl. Phys. Lett.*, vol. 35, no. 10, pp. 776-777, Nov. 1979, DOI: 10.1063/1.90974
- [114] W. Lochmann, A. Haug, "Phonon-Assisted Auger Recombination in Si with Direct Calculation of the Overlap Integrals," *Solid State Communications*, vol. 35, no. 7, pp. 553-556, Aug. 1980, DOI: 10.1016/0038-1098(80)90896-0
- [115] R. Häcker, A. Hangleiter, "Intrinsic upper limits of the carrier lifetime in silicon," *J. Appl. Phys.*, vol. 75, no. 11, pp. 7570-7572, Jun. 1994, DOI: 10.1063/1.356634
- [116] R.L.Plackett, J.P.Burman, "The design of optimum multifactorial experiments," *Biometrika*, vol. 33, pp. 305-325, Jun. 1946, DOI: 10.2307/2332195
- [117] F. Roger, *et al.*, "Global statistical methodology for the analysis of equipment parameter effects on TSV formation," *2015. International Workshop on CMOS Variability*, Salvador de Bahia, September 2015., pp. 39-44, DOI: 10.1109/VARI.2015.7456561
- [118] P. Fernandez-Martinez, *et al.*, "Simulation of Total Ionizing Dose in MOS Capacitors," in *Proc. of the 8th Spanish Conf. on Electron Devices*, 2011, pp. 1-4, DOI: 10.1109/SCED.2011.5744251

- [119] P. Paillet, *et al.*, “Simulation of Multi-Level Radiation-Induced Charge Trapping and Thermally Activated Phenomena in SiO<sub>2</sub>,” *IEEE Trans. Nucl. Sci.*, vol. 45, no. 3, pp. 1379-1384, Jun. 1998, DOI: 10.1109/RADECS.1997.698841
- [120] A. G. Aberle, “Fundamentals of silicon surface passivation with silicon dioxide and plasma silicon nitride,” in *Crystalline silicon solar cells – Advanced Surface Passivation and Analysis*, 1st edition, Centre for Photovoltaic Engineering, Australia: University of New South Wales, 2004, ch. 4, sec. 4.3, pp. 90-113.
- [121] V. Sharma, “Study of Charges Present in Silicon Nitride Thin Films and Their Effect on Silicon Solar Cells Efficiencies“, Ph.D. dissertation, Arizona State University, Tempe, AZ, USA, 2013.
- [122] F. Faccio, *et al.*, “Influence of LDD Spacers and H<sup>+</sup> Transport on the Total-Ionizing-Dose Response of 65-nm MOSFETs Irradiated to Ultrahigh Doses,” *IEEE Trans. Nucl. Sci.*, vol. 65, no. 1, pp. 164-174, Jan. 2018, DOI: 10.1109/TNS.2017.2760629
- [123] P. J. McWhorter, S. L. Miller, T. A. Dellin, “Radiation Response of SNOS Nonvolatile Transistors,” *IEEE Trans. Nucl. Sci.*, vol. 33, no. 6, pp. 1413-1419, Dec. 1986, DOI: 10.1109/TNS.1986.4334615
- [124] H. Puchner, *et al.*, “Impact of Total Ionizing Dose on the Data Retention of a 65nm SONOS-Based NOR Flash,” *IEEE Trans. Nucl. Sci.*, vol. 61, no. 6, pp. 3005-3009, Dec. 2014, DOI: 10.1109/TNS.2014.2367451
- [125] F. Moscatelli, *et al.*, “Measurements and TCAD Simulations of Bulk and Surface Radiation Damage Effects in Silicon Detectors,” *Proc. 2015 IEEE Nucl. Sci. Symp. Med. Imag. Conf. (NSS/MIC)*, 2015, pp. 858-863, DOI: 10.1109/NSSMIC.2015.7581944

## **Biography**

Filip Šegmanović was born in Zagreb, Croatia, on 14<sup>th</sup> May 1992. He finished elementary school and high school in Zagreb. He studied Electrical Engineering and Information Technology at the Faculty of Electrical Engineering and Computing at the University of Zagreb. During his studies, he attended lectures in the field of microelectronics, semiconductor technology, as well as analogue and digital integrated circuits. During his Master studies, he received the Rector's Award for the best scientific paper. He received his BSc in 2014 and his MSc in 2016 on the topic of quenching circuits which used single-photon avalanche diodes as the detecting elements. After his MSc, he was hired as a PhD researcher at the ams OSRAM company. Apart from technical training in the topics of microelectronics and detectors, during his PhD he also attended courses on innovation management and technological competence leveraging, and acquired a PRINCE2 certificate in project management. He is the author of numerous papers on radiation-hard photodetectors and has participated in several international conferences.

## List of publications

1. I. Berdalović, Ž. Osrečki, F. Šegmanović, D. Grubišić, T. Knežević, T. Suligoj, "Design of passive-quenching active-reset circuit with adjustable hold-off time for single-photon avalanche diodes", *Proceedings of the 39th International Convention on Information and Communication Technology, Electronics and Microelectronics (MIPRO 2016)*
2. F. Šegmanović, G. Meinhardt, F. Roger, I. Jonak-Auer, T Suligoj, "Impact of TCAD Model Parameters on Optical and Electrical Characteristics of Radiation-Hard Photodiode in 0.35 $\mu$ m CMOS Technology," *2018 41st Int. Conv. on Information and Communication Technology, Electronics and Microelectronics (MIPRO)*, Opatija, Croatia, 2018, pp. 18-22, DOI: 10.23919/MIPRO.2018.8400003
3. F. Šegmanović, G. Meinhardt, F. Roger, I. Jonak-Auer, T Suligoj, "Optical and electrical simulations of radiation-hard photodiode in 0.35 $\mu$ m high-voltage CMOS technology," *2018 28th Int. Symp. on Power and Timing Modeling, Optimization and Simulation (PATMOS)*, Costa Brava, Spain, 2018, pp. 92-96, DOI: 10.1109/PATMOS.2018.8464156
4. F. Šegmanović, G. Meinhardt, F. Roger, I. Jonak-Auer, T Suligoj, "Evaluation of the Radiation Hardness of Photodiodes in 180-nm CMOS Technology for Medical Applications", *IEEE Trans. Nucl. Sci.*, vol. 68, no. 9, pp. 2367–2374, Sep. 2021, DOI: 0.1109/TNS.2021.3101920

## Životopis

Filip Šegmanović je rođen 14.05.1992. u Zagrebu, u Hrvatskoj. Završio je osnovnu i srednju školu u Zagrebu. Studirao je elektrotehniku i informacijske tehnologije na Fakultetu Elektrotehnike i Računarstva, na Sveučilištu u Zagrebu. Tijekom studija, pohađao je kolegije u području mikroelektronike, poluvodičke tehnologije te analognih i digitalnih integriranih sklopova. Tijekom diplomskog studija primio je Rektorovu nagradu za najbolji znanstveni rad. Diplomirao je 2014. i magistrirao 2016. na temu sklopova za potiskivanje proboja fotodioda za detekciju jednog fotona. Nakon magistriranja, zaposlio se kao doktorand u firmi ams OSRAM. Osim stručnog usavršavanja na području mikroelektronike i detektora, tijekom doktorata sudjeluje i na tečajevima o menadžmentu inovacijama i primjeni tehnologija u poslovnom svijetu, te stječe i certifikat PRINCE2 za upravljanje projektima. Autor je brojnih konferencijskih radova te jednog rada u znanstvenom časopisu na temu fotodetektora otpornosti na ionizacijsko zračenje.